AD-A282 369

Ultrawideband Shipboard Electrooptic Electromagnetic Environment Monitoring

S. A. Pappert
M. H. Berry
S. M. Hart
R. J. Orazi
L. B. Koyama
S. T. Li

DTIC
ELECTE
JUL 2 5 1994
S G D

94-22723

UNITED STATES NAVY

NRaD

DTIC QUALITY INSPECTED 1

Technical Report 1646
May 1994

Ultrawideband Shipboard Electrooptic Electromagnetic Environment Monitoring

S. A. Pappert
M. H. Berry
S. M. Hart
R. J. Orazi
L. B. Koyama
S. T. Li

Accesion For		
NTIS CRA&I		☒
DTIC TAB		☒
Unannounced		☐
Justification		
By		
Dist ibution /		
Availability Codes		
Dist	Avail and / or Special	
A-1		

ADMINISTRATIVE INFORMATION

This report is submitted in partial fulfillment of Milestones 3, 4, 5, and 6, Task Number 3 (Electrooptic Electromagnetic Monitoring) of the Electromagnetic Compatibility Project (RH21C13) of the Surface Ship Technology Area Program (SC1A/PE0602121N). The work described herein was sponsored by the Office of Naval Research (ONR 334) under contract N0016791WX10040. The work was performed by the Naval Command, Control and Ocean Surveillance Center (NRaD Codes 555, 822, 843, and 753).

Released by
Matthew N. McLandrich, Head
Optical Electronics Branch

Under authority of
Dr. Howard E. Rast, Head
Solid State Electronics
Division

SM

EXECUTIVE SUMMARY

OBJECTIVE

1. Design, construct, package, test, and evaluate the best available wideband photonic electromagnetic field probe for shipboard electromagnetic environment (EME) monitoring.

2. Develop engineering solutions to problems encountered in Phase I testing of a first-generation breadboarded sensor. Investigate and develop alternative sensor configurations that can lead to improved system performance.

3. Develop requirements and a test plan for the shipboard testing of a 2-MHz to 18-GHz prototype system.

RESULTS

1. Broadband electromagnetic (EM) field detection using antenna-coupled fiber optic links has been successfully demonstrated in the 2-MHz to 18-GHz frequency range. This remote sensing system is potentially operable from 2 MHz to 50 GHz and can be packaged into small, lightweight units. Both amplitude and frequency information of multiple radio frequency and microwave signals have been simultaneously monitored with this wideband optical system. A root mean square electric field sensitivity of approximately 1 μV/m and a spurious free dynamic range of 109 dB/Hz$^{2/3}$ have been demonstrated with the 18-GHz externally modulated system.

2. Semiconductor optical waveguide modulators have been developed as an alternative to lithium niobate Mach–Zehnder modulators for this application. Systems employing the less mature semiconductor optical modulators have shown greater modulation efficiency for a given bandwidth at the expense of added optical insertion loss than lithium niobate-based systems.

3. Remote modulator bias control techniques have been investigated and a system based on the active control of the modulator direct current bias to compensate for bias position drift has been developed. This system utilizes a remote power-by-light approach in which a low-frequency optical control signal is sent to the modulator via an optical fiber and is remotely monitored to properly bias the optical modulator. This system has been successfully demonstrated in the 10°C to 90°C temperature range.

4. A remote optical polarization controller has been successfully demonstrated, which eliminated the need for expensive polarization-maintaining fiber. The controller has an optical insertion loss of 4.5-dB, resulting in a 9-dB penalty in detection sensitivity. Recent improvements in liquid crystal technology have resulted in polarization controller units with <2-dB optical insertion loss.

5. Small spiral antennas with responses from 300 MHz to 50 GHz have been demonstrated and are ideal for this shipboard emission monitoring system. Below 500 MHz, a number of approaches are currently being investigated to optimize the size/gain tradeoff characteristics of various antenna structures. One approach is to fabricate slightly larger spiral antennas to enhance the low-frequency response. A second approach to increase the low-frequency response is to fabricate spiral antennas on a

high-dielectric-constant substrate. A third approach has been to use a sectoralized loaded monopole antenna. A fourth approach is to suffer the gain penalty and use an electrically short dipole antenna. Each technique has its advantages and disadvantages, although the use of an electrically short dipole antenna is the simplest approach, and results indicate that acceptable 2-MHz to 500-MHz electric field sensitivities can be obtained using this approach.

6. A preliminary test plan for the FY 94 shipboard demonstration aboard an LSD-41 class surface ship is outlined. Preliminary results indicate that as few as three topside monitoring locations are required to obtain the electromagnetic signature of the ship.

RECOMMENDATIONS

1. Prepare the 2-MHz to 18-GHz prototype electrooptic EME system for a shipboard demonstration test to occur in FY 94. Continue developing the semiconductor optical waveguide modulators to eventually replace the presently used lithium niobate modulators. Extend fiber optic link operation to 50 GHz using both semiconductor and lithium niobate modulators and compare their performance.

2. Develop and optimize radio frequency and microwave probe designs for continuous 2-MHz to 50-GHz frequency coverage with compact, lightweight antennas.

3. Demonstrate EM field detection from 2 MHz to 50 GHz with a single fiber optic link and as few antennas as possible.

CONTENTS

FIGURES

TABLES

ABBREVIATIONS

BW	bandwidth
EA	electroabsorption
EHF	extremely high frequency
EM	electromagnetic
EMC	electromagnetic compatibility
EMCON	electromagnetic control
EME	electromagnetic environment
EMI	electromagnetic interference
EO	electrooptic
FKE	Franz-Keldysh effect
HF	high frequency
IOM	integrated optical modulator
LNA	low-noise amplifier
LPE	liquid phase epitaxy
MF	multimode fiber
MOCVD	metalorganic chemical vapor deposition
MZ	Mach-Zehnder
NF	noise figure
PBL	power-by-light
PMF	polarization-maintaining fiber
QCSE	quantum-confined Stark effect
QMS	quality monitoring system
QW	quantum well
RF	radio frequency
RIN	relative intensity noise
RMS	root mean square
SATCOM	satellite communication
SFDR	spurious free dynamic range
SL	superlattice
SMF	single-mode fiber
S/N	signal-to-noise ratio
UHF	ultrahigh frequency
VHF	very high frequency
VSWR	voltage standing wave ratio

1.0 INTRODUCTION

The shipboard electromagnetic environment (EME) routinely consists of high-level on-ship emissions extending from the high-frequency (HF) band into the extremely high frequency (EHF) band. Rapid advances in the areas of radar, electronic warfare (EW), and communications technologies are making this EME more complex and at the same time more difficult to manage. The Navy has an increasing need to monitor these emissions and verify electromagnetic control (EMCON) status as well as alert personnel of hazardous emission levels. To address this need, the Navy is seeking affordable, broadband shipboard EME monitoring probes and systems that are as nonperturbing as possible.

In response to this shipboard EME monitoring requirement, photonic techniques are being developed in association with wideband radio frequency (RF) probes for use in EME monitoring systems. The emerging photonic technologies will enable the Navy to collect and transmit broadband shipboard EME information for processing at a remote site while minimizing the overall system intrusiveness. Recent advances of high-speed fiber optic and electrooptic (EO) components has made this EME monitoring system approach viable and will provide ship operators with a valuable new command, control, communication, computer, and intelligence (C⁴I) capability. This status report reviews past EO EME monitoring system work and presents results from current efforts geared toward making this technology feasible. Requirements as well as test and evaluation plans for the shipboard demonstration to be conducted under this program in FY 94 are also presented.

1.1 TECHNICAL OBJECTIVE AND APPROACH

The principal objective of the Office of Naval Research-sponsored Electromagnetic Compatibility (EMC) Project is to minimize exterior electromagnetic interference (EMI) problems during the entire life cycle of Navy ships. An additional objective is the reduction or control of the RF emission signature of Navy surface combatants. This involves the task of controlling shipboard RF emissions by remote monitoring of the entire shipboard RF spectrum to determine, verify, and enforce the EMCON status.

Task Number 3 of the EMC Project develops a broadband, large-dynamic-range EM field probe that can be packaged into a small, lightweight system. The Task couples EO devices to wideband RF probes to provide a low-cost system that can monitor EM emission from the ship. This system is potentially useful from 2 MHz to 50 GHz, where most shipboard emission occurs. In addition to EMCON monitoring, the potential benefits or usages of this system will include the detection of RF hazards levels at key locations on the ship weather decks, the quality monitoring of communication emitters (QMS), and real-time automated frequency management.

The technical approach of this task is to build upon current photonic technology and bridge the gap where technology deficiencies exist to demonstrate a 2-MHz to 50-GHz EO EM field sensor. Photonic and wideband antenna component performances are being extended where necessary to meet the shipboard application requirements. The task will culminate in a shipboard demonstration of a prototype EO field sensor at which time the effort will be transitioned for further engineering development.

This four-year R&D task (FY 91 to FY 94) is being performed in three phases. Phase I was started and completed in FY 91; Phase II was started in FY 92 and will be completed in FY 94;

and Phase III is to begin in FY 93 and conclude in FY 94. Phase I (Milestones 1 and 2) consisted of assessing the present state-of-the-art of EO field sensors and determining their suitability for shipboard use. Phase II (Milestones 3, 4, 5, and 6) of this effort deals with solving problems determined from Phase I breadboard testing of the candidate EO EME monitoring system, developing alternative sensor schemes to improve system performance and extend frequency coverage, optimizing the RF probe design for efficient wideband coverage, and determining design guidelines for a concept demonstration of the EO sensor. Phase III of this work will consist of designing, constructing, and packaging the best available EO field sensor into a prototype demonstration system. System performance will be measured and the environmental ruggedness of the prototype system will be assessed. Shipboard testing and a subsequent final report will finish the advanced development work assosciated with this effort.

This report describes the work performed in Phase II (Milestones 3, 4, 5, and 6) of this Task.

1.2 BACKGROUND

Electromagnetic field sensing using EO and fiber optic techniques has been of interest to the Navy for some time. Previous work in this area has considered antenna-coupled lithium niobate bulk crystal and waveguide modulators, where high sensitivities have been attained for system bandwidths below 1 GHz.[1-3] This class of field sensor, which uses an optical intensity modulator for the RF electrical-to-optical conversion, is referred to as an externally modulated field monitoring system. An alternative EO field sensing approach has focused on the direct current modulation of an antenna-coupled high-speed injection laser diode.[4,5] This is referred to as a directly modulated field monitoring system. Both approaches use fiber optic links to transmit the EME information to a remote processing site. Directly modulated short-haul fiber optic systems possess a simpler design and are easier to implement, whereas externally modulated systems have been shown to be more sensitive and possess larger 3-dB bandwidths.[6,7]

Phase I work of this project demonstrated that the externally modulated EO EME monitoring system will ultimately outperform the directly modulated system and better meet shipboard EMCON monitoring system requirements. This conclusion was based on the superior noise characteristics of high-power solid-state lasers* (which can be used for externally modulated systems) compared to those of injection laser diodes and on the superior high-frequency modulation characteristics of external waveguide modulators.

As stated above, Phase II of this program began in FY 92 and involved determining solutions to problems encountered in Phase I and extending the performance capabilities of the selected EM field monitoring system. Anechoic chamber testing of an externally modulated EO EME system has been performed in the 2- to 18-GHz frequency range. A root mean square (RMS) electric field sensitivity of 15 μV/m and a spurious free dynamic range (SFDR) of 102 dB in a 1-Hz resolution bandwidth have been measured with this 2- to 18-GHz field detection system. These chamber results indicate that the externally modulated EO EME system can be useful for the proposed shipboard applications. Greater sensitivity is expected by increasing the optical power of the laser and by improving the optical modulator's RF efficiency. Both these modifications have been implemented. Laboratory testing of these refined EO sensor systems has been performed, and an increased sensitivity and dynamic range have been attained over the prior

---

*Available from Amoco Laser Co.

2

anechoic chamber results. A broadband fiber optic link noise figure of < 30 dB has been measured, which translates into a 1-Hz RMS electric field senstivity of approximately 1 μV/m.

A number of other system modifications have been investigated in an attempt to work out all the problem areas associated with this sensor. These Phase II modifications include the development of modified optical fiber cable assemblies to minimize polarization drift, the incorporation of polarization-insensitive semiconductor modulator designs and polarization-control devices to eliminate the need for polarization-maintaining fiber, and the operation of temperature-insensitive fiber optic links.

Developing more efficient optical modulators and extending their frequency range to 50 GHz is an ongoing thrust of the Phase II work, with both in-house and industrial efforts. The conventional design for externally modulated EO EME monitoring systems includes lithium niobate optical waveguide modulators. Although lithium niobate waveguide modulators are relatively mature and available with bandwidths to 18 GHz,* these broadband devices have complicated traveling-wave electrode designs and possess half-wave voltages in the 10-V range. An alternative to lithium niobate waveguide modulators for the externally moduated EO EME system are III-V semiconductor waveguide modulators. Both interferometric and absorption modulators are possible,[8,9] a'though emphasis in this report has been on semiconductor electroabsorption (EA) waveguide modulators. Both quantum-confined Stark effect[10] (QCSE) and Franz-Keldysh effect[11] (FKE) EA devices operating at 1.52 μm and 1.32 μm, respectively, are included. Both of these devices rely for operation on material absorption coefficient changes with an applied electric field. Fiber optic link sensitivity, spurious free dynamic range (SFDR), and bandwidth predictions using these EA devices based on theoretical and experimental results are presented and compared to those of lithium niobate-based fiber optic links.

A final photonic probe design for the FY 94 shipboard demonstration has been completed. Fiber optic link implementations include a power-by-light (PBL) system to optically power the modulator as well as a modulator bias-control circuit to automatically adjust for environmental changes. These two system insertions improved the usefulness of the EO field sensor, and the results of testing these system modifications will be presented.

Phase II antenna development efforts include the development of a compact HF/very high frequency (VHF) antenna as well as a wideband spiral antenna useable to 50 GHz. Advanced antenna developmental efforts include the development of compact HF/VHF antennas. One approach being pursued is the development of a small-aperture, high-dielectric spiral antenna, which should provide useable gain down into the HF band. Other low-frequency antenna candidates include an enlarged spiral antenna, a sectoralized monopole antenna, and an electrically short dipole antenna. Results using these HF/VHF/ultrahigh frequency (UHF) antenna structures are presented. A miniature spiral antenna design with gain to 50 GHz is also being developed and will be discussed. These antenna R&D efforts will continue into FY 94.

An initial test plan for the shipboard demonstration of the photonic EM field probe has been developed. The prototype sensor will be placed at selected topside sites of an LSD-41 class surface ship and controlled emissions will be recorded. Detailed testing procedures will be described.

---

*Available from United Technologies Photonics.

2.0 SHIPBOARD EO EME MONITORING

In this section, an externally modulated EO EME monitoring system is described and laboratory results on a number of breadboarded systems are presented and compared with simulations. The photonic link as well as the wideband RF probe will also be discussed.

2.1 DESCRIPTION OF EXTERNALLY MODULATED EO EME MONITORING SYSTEM

A schematic diagram of an antenna-coupled externally modulated EO EME monitoring system is shown in figure 2-1. Its primary components include a high-power, low-noise, polarized optical source, polarization-maintaining single-mode optical fiber (PMF) for the uplink, an antenna-coupled optical waveguide modulator, standard single-mode fiber (SMF) for the downlink, a high-speed p-i-n photodiode, and a signal processor. The signal processor will normally consist of a wideband spectrum analyzer and a central processing unit. Low-noise preamplifiers are not included in the EO EME monitoring system configuration and are not considered necessary for this relatively high signal level application. The antenna and optical modulator are positioned at a selected point about the ship for EM field detection, while amplitude and frequency information is remotely received and processed. The intent of this geometry or configuration is to minimize the perturbation of the EM field by eliminating any electrical transmission lines between the probe and receiving station. If passive modulator biasing is not feasible, electrical powering or biasing of the optical modulator can be achieved optically via a high-power laser diode, a multimode optical fiber, and photovoltaic cells for optical-to-electrical power conversion. This optical powering scheme is generically shown in figure 2-2 and its implementation is discussed in Section 3.1.

Initial laboratory prototypes of the EO EME monitoring system operate from 2 to 18 GHz and use a wideband spiral antenna which possesses a 50 Ω output impedance and a minimum gain of 0 dBi across this band. A system is presently being constructed for shipboard testing, which is operable from 2 MHz to 18 GHz. This prototype system has been designed to operate with a number of different optical modulator types that are being developed as part of this R&D effort and that are described below. A four-fiber, all dielectric optical cable has been designed and fabricated for this prototype system; it allows for analog EME information as well as modulator biasing signals to be transferred to a remote site. The optics of the sensor head is packaged in a plastic box that mates to the wideband antenna via an SMA-connector. Antenna or probe output powers ranging from less than –60 dBm to greater than 20 dBm can be expected at some topside positions.[12] This implies that the monitoring system must realize an SFDR exceeding 80 dB and a sensitivity below –60 dBm. This system performance must eventually be attained from 2 MHz to 50 GHz by some combination of field detection units. This will be accomplished by combining the broadband RF information from the banded antennas onto a single fiber optic link, as is shown in figure 2-3. Hence, optical modulators with the potential for extremely wide passband operation are required for this shipboard application. The optical waveguide modulator alternatives being pursued in this work will now be discussed.
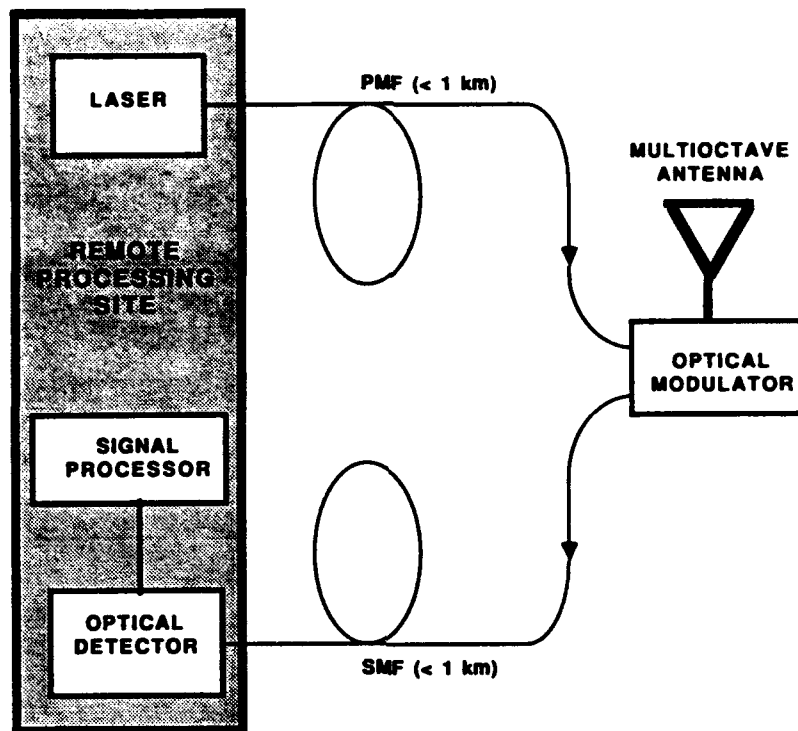
Figure 2-1. Schematic diagram of an antenna-coupled externally modulated EO EME monitoring system.
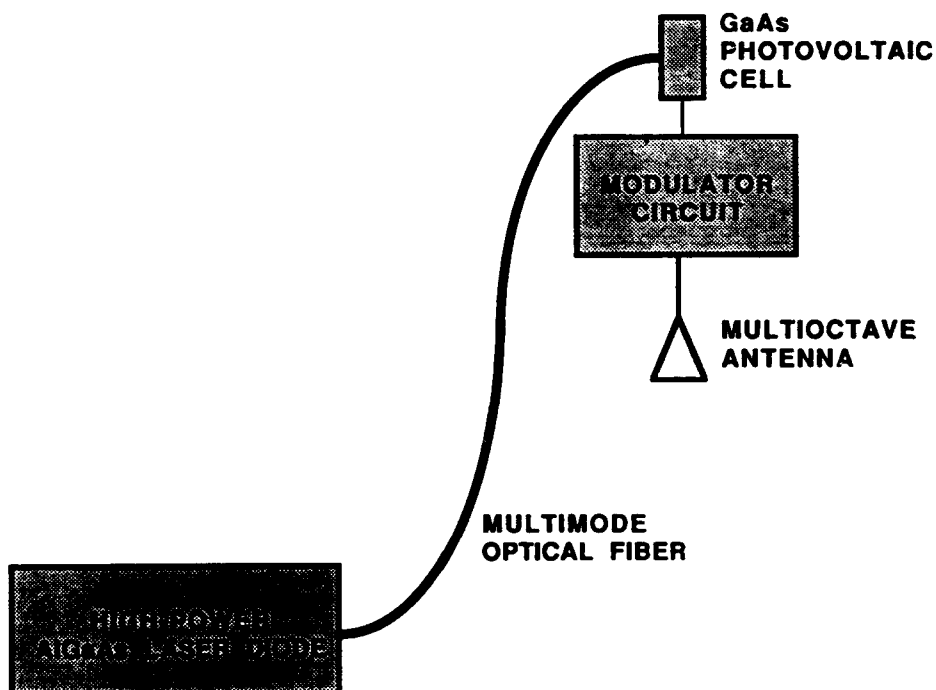
Figure 2-2. Optical powering scheme using GaAs photovoltaic cells for the EO EME monitoring system.

5
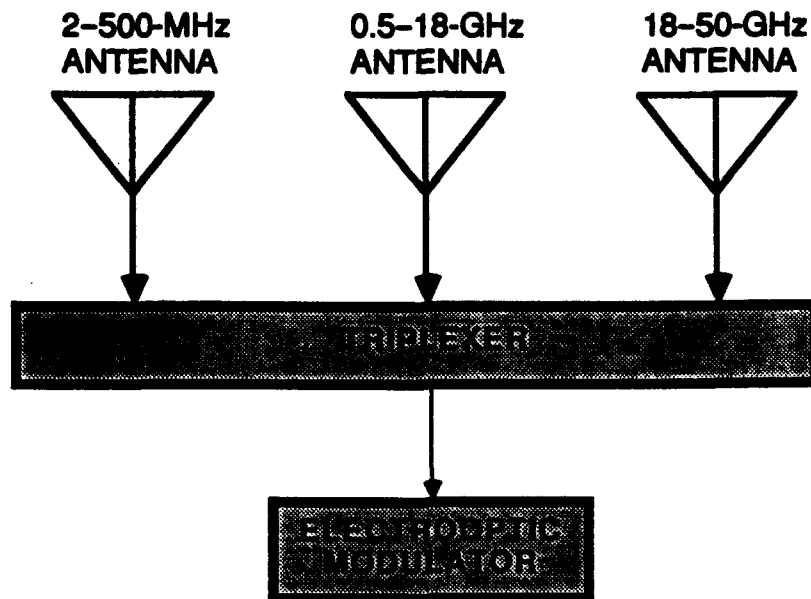
Figure 2-3. Triplexing scheme to combine RF information from 2 MHz through 50 GHz.

2.1.1 Lithium Niobate Optical Waveguide Modulators

The most used crystal for producing broadband optical waveguide modulators is lithium niobate. This material has a large linear EO coefficient and low-loss single-mode waveguides can be easily formed by using titanium indiffusion or proton-exchange techniques. MZ waveguide modulators fabricated with traveling-wave electrodes on x-cut lithium niobate are the most promising of the commercially available high-bandwidth modulator devices. A schematic of this interferometric waveguide modulator is shown in figure 2-4. In these devices, light is coupled from a single-mode optical fiber into a lithium niobate waveguide. The light is equally split at the input Y-branch and then recombined at a similiar output Y-branch. The light in one arm of the interferometer is phase-modulated by an RF signal and results in intensity modulation for the combined output optical waveguide mode. The intensity-modulated output optical power is then coupled back into a single-mode optical fiber for transmission. The expression for the output optical power as a function of the input optical power for an ideal MZ modulator is given by

$$S_{out}(V) = S_{in} \ t_m \cos^2 \ (\pi V/2V_\pi) \qquad (2.1)$$

where

S_{in}	=	input optical power
t_m	=	modulator transmission loss factor
V_π	=	modulator half-wave voltage

6
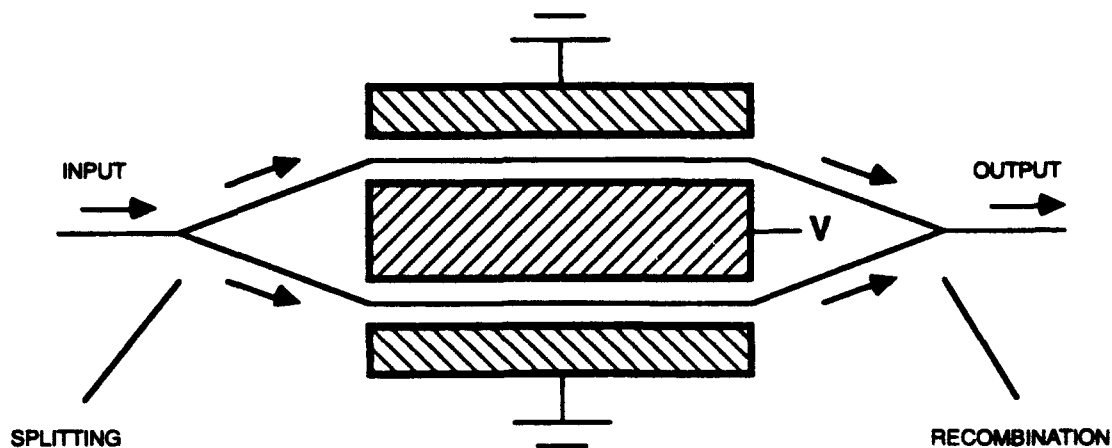
Figure 2-4. Schematic of lithium niobate MZ interferometric optical modulator.

For analog applications, in addition to the RF signal, a DC bias of $V_\pi/2$ is applied to achieve maximum RF sensitivity. The highest speed commercially available lithium niobate MZ modulators possess an 18-GHz modulation bandwidth, a V_π of approximately 10 volts, and a t_m of approximately 0.5.* An x-cut lithium niobate MZ modulator with performance specifications close to this has been procured and tested in this effort. The x-cut crystal was chosen over the z-cut crystal because of its demonstrated superior thermal stability. This device was used in the 2- to 18-GHz laboratory system that was tested and whose experimental results will be discussed in Sections 2.3 and 2.4. Alternative optical waveguide modulators that have attracted consider-able recent attention are III-V semiconductor-based interferometric and EA modulators. These are now discussed.

2.1.2 III-V Semiconductor Optical Waveguide Modulators

GaAs-based MZ modulators operating at 1.3 μm are beginning to become available. The operation of these modulators is identical to that of the lithium niobate modulators discussed above. Better phase matching between the optical and electrical signals is expected with the GaAs traveling-wave modulator than with the lithium niobate modulator. This should allow for higher bandwidth devices without sacrificing modulation efficiency. Obtaining low optical insertion loss is a remaining challenge for the GaAs MZ modulators. A DC to 50-GHz proto-type GaAs modulator possessing an RF $V_\pi = 10$ V and a 10-dB optical insertion loss is to be delivered to the Navy for use in this effort. For the bandwidth, the modulation efficiency of this device exceeds any available lithium niobate modulator, although the optical insertion loss is significantly higher (10 dB compared to 3 dB). When this semiconductor modulator is received, it will be tested and evaluated for use in this shipboard application. Another promising III-V semiconductor optical modulator is the EA waveguide modulator. This type of modulator will now be discussed.

Semiconductor EA waveguide modulators fabricated in either a p-i-n or p-n junction structure are also being considered for this analog fiber optic application. Here, a reverse bias

---

*Available from GEC Advanced Optical Products.

7

across the junction modulates the electric field in the waveguide and changes the absorption coefficient of the material. The semiconductor EA waveguide modulator possesses an exponential optical power transmission relation given by

$$S_{out}(V) = S_{in}t_m \exp[-\Gamma\Delta a(V)\ L] \tag{2.2}$$

where

S_{in}	=	input optical power
t_m	=	modulator transmission loss factor
L	=	waveguide length
Γ	=	optical mode and active absorbing layer overlap integral
Δa	=	change in absorption coefficient

In quantum well structures, Δa is due to the QCSE. In thick (> 500 Å) or bulk semiconductor layers, Δa is due to the FKE. QCSE modulators typically have a large Δa at low applied voltage, but possess a relatively small Γ, while FKE modulators typically have a small Δa, but a large Γ. It can be seen from Eq. 2.2 that these two parameters equally affect the modulator's performance and therefore both devices can obtain comparable modulation performance. Prebiasing the EA modulator to the quasilinear region enables analog operation in the same manner as with MZ modulators. The modulator linearity can be assessed by measuring the harmonic and intermodulation distortion about a given bias position, which ultimately determines the SFDR.

Two modulators, a 1.52-μm QCSE modulator and a 1.32-μm FKE modulator, have been fabricated and tested for use in the EO EME monitoring system. The liquid phase epitaxy (LPE) grown 1.32-μm FKE modulator is schematically shown in figure 2-5 and uses an InGaAsP active absorbing waveguide layer. This ridge-waveguide modulator has a device length of 300 μm, a waveguide thickness of 0.4 μm, a device capacitance of 0.2 pF, and a $\Gamma \approx 0.7$. For digital applications, an extinction ratio of > 30 dB at less than 10 V has been obtained with this modulator.

The 1.52-μm QCSE modulator uses an InGaAs/InP quantum well ridge-waveguide structure and was grown using metalorganic chemical vapor deposition (MOCVD). A schematic of this modulator is shown in figure 2-6. This device has a length of 650 μm, an undoped superlattice waveguide thickness of 1 μm, and a $\Gamma \approx 0.1$. It is the ten 70-Å InGaAs quantum wells buried in the center of the superlattice waveguide of this modulator structure that are responsible for the 1.52-μm absorption modulation. This waveguide modulator has also displayed a > 30-dB extinction ratio at less than 10 V applied bias. For more details about these specific modulators, the interested reader is referred elsewhere.[13,14] Analog photonic links and electromagnetic field monitoring systems employing these optical modulator types will be analyzed next.

8
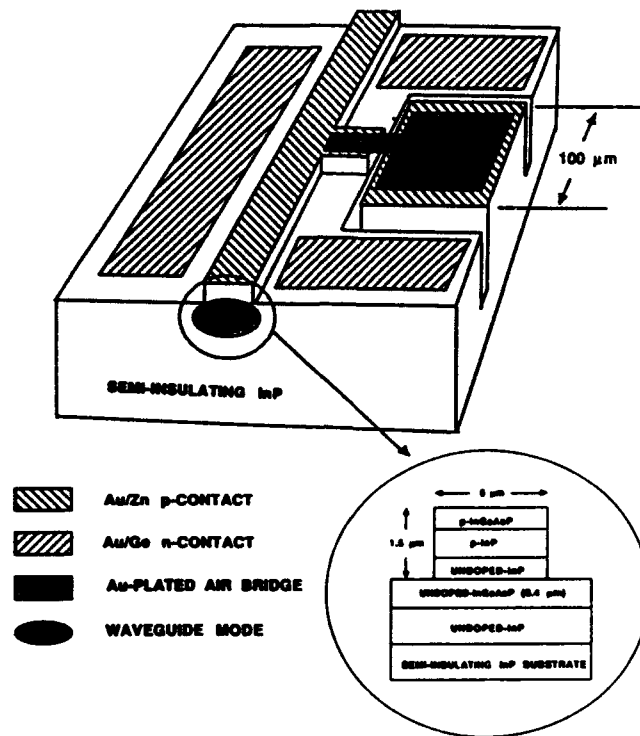
Figure 2-5. Structure of LPE-grown 1.32-μm InGaAsP
FKE optical modulator.
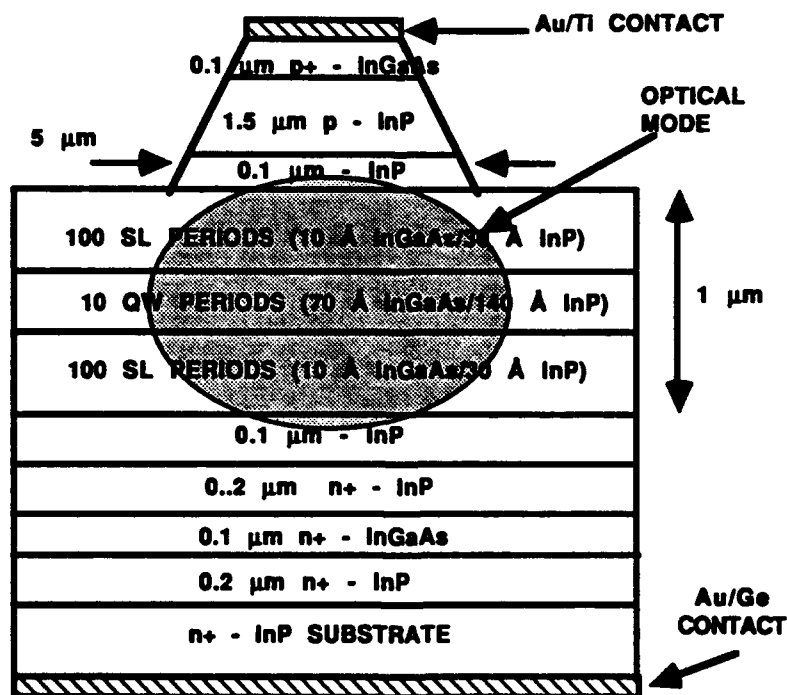
Figure 2-6. Structure of MOCVD-grown 1.52-μm InGaAsP/InP
multiple quantum well QCSE optical modulator.

2.2 ANALYSIS OF EO EME MONITORING SYSTEM

The externally modulated EO EME system described in Section 2.1 will now be theoretically analyzed. Performance will be predicted and important noise sources identified. Particular attention will be paid to the performance characteristics of the optical modulator. For digital applications, a modulator's usefulness is determined primarily by its bandwidth, switching voltage (bias required to obtain a 10-dB extinction ratio), and optical insertion loss. For analog link applications like the one at hand, the modulator's bandwidth, linearity, RF efficiency, and optical insertion loss are important. These parameters will now be discussed for both MZ modulator and EA modulator-based systems, and a performance comparison analysis will be made between the lithium niobate and semiconductor modulator options.

To assess the relative usefulness of the candidate optical waveguide modulators discussed in Section 2.1, an externally modulated fiber optic link was breadboarded. Modulator characteristics were measured for the FKE and QCSE modulators and compared to those of a high-speed 1.32-μm lithium niobate MZ waveguide modulator. The MZ modulator performance specifications used for this comparison are a $V_\pi = 10$ V, a fiber-to-fiber insertion loss of 3 dB, and a 3-dB electrical bandwidth of 18 GHz, specifications which at this time compare favorably with other commercially available MZ modulators. As described in the previous Section, the relevent QCSE modulator parameters for transverse magnetic (TM) mode operation are a device length of $L = 650$ μm, a confinement factor of $\Gamma = 0.07$, and a device capacitance of 1.2 pF. The relevent FKE modulator parameters are a device length of 300 μm, a confinement factor of 0.7, and a device capacitance of 0.2 pF.

The relative transmission versus applied bias or optical transfer functions for the FKE, QCSE, and MZ modulators are shown in figure 2-7. The important aspects of these curves for this analog application are (1) the bias required to obtain quasilinear operation, (2) the slope of the curve at the bias point, which is a measure of the RF efficiency, and (3) the linearity about the bias point. These aspects will now be investigated.

The externally modulated fiber optic link RF insertion loss can be expressed as

$$H^2 = K_f^2 \, r_d^2 R_{out} \, r_m^2 \tag{2.3}$$

where

K_f	=	optical loss from source to detector (not including modulator insertion loss)
r_d	=	detector responsivity (A/W_o)
R_{out}	=	detector output resistance (Ω)
r_m^2	=	modulator RF efficiency factor $(W_o/W_e \leftarrow)$.

For an MZ modulator

$$r_m^2 = (t_m \, P_o \, \pi/V_\pi)^2 \, (R_m/2) \, (1-\rho_m^2) \tag{2.4}$$

where P_o is the laser power, t_m is the modulator transmission factor, R_m is the modulator input resistance, and ρ_m is the modulator input RF reflection coefficient. For an EA modulator, r_m is given by

$$r_m^2 = (t_m \, P_o)^2 \, (R_m/2) \, (1-\rho_m^2) \, [\Gamma L \, (d\Delta\alpha/dV)_{V_b}]^2 \tag{2.5}$$

10
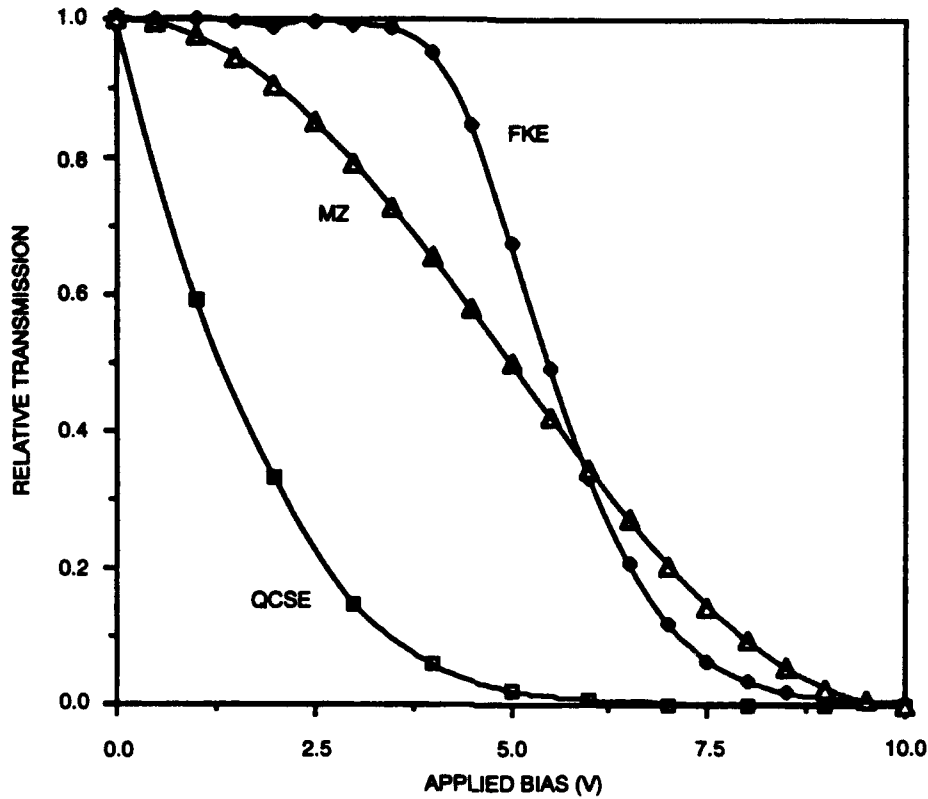
Figure 2-7. Relative transmission versus applied bias curves for the
1.32-μm FKE waveguide modulator, the 1.52-μm QCSE waveguide
modulator, and the 1.32-μm lithium niobate MZ waveguide modulator.

where the derivative is taken at the modulator bias voltage, V_b. Measured values for $\Delta\alpha$ as a
function of voltage for the QCSE and FKE modulators are shown in figure 2-8. It is found that
$(d\Delta\alpha/dV)$ evaluated at $V_b \approx 2$ V is equal to 150 $(cm-V)^{-1}$ for the QCSE modulator and 50
$(cm-V)^{-1}$ at $V_b \approx 6$ V for the FKE modulator. If we assume that $P_o = 50$ mW, $R_m = 50$ Ω, $\rho_m = 0$, and $t_m = 0.10$, we find that $r_{FKE}^2 = 6.9$ x 10^{-4} (W_o^2/W_e) and $r_{QCSE}^2 = 2.9$ x 10^{-4} (W_o^2/W_e). For
the MZ modulator, we will also assume $P_o = 50$ mW, $R_m = 50$ Ω, $\rho_m = 0$, but a lower optical
insertion loss yielding $t_m = 0.50$. Using these numbers gives $r_{MZ}^2 = 1.5$ x 10^{-3} (W_o^2/W_e) which
is slightly larger than that of the FKE modulator. This result is entirely due to the presently
encountered larger EA modulators' optical insertion loss (10 dB versus 3 dB). Hence, even
though the insertion loss of the EA modulators is substantially larger than that of the MZ
modulator, the RF power efficiencies are comparable due to the larger modulator optical power
transfer function slopes evident in figure 2-7. If the insertion loss of the EA modulators can be
improved to the same level as the MZ modulator, then efficiencies of $r_{FKE}^2 = 1.7$ x 10^{-2}
(W_o^2/W_e) and $r_{QCSE}^2 = 7.3$ x 10^{-3} (W_o^2/W_e) are obtained, which are significant improvements
over current state-of-the-art MZ modulators. If we further assume that $R_{out} = 50$ Ω, $r_d = 0.85$
A/W_o, and $K_f = 0.1$ (including 3 dB for biasing of the modulator), then the expected RF insertion
loss is −33 dB for the MZ system, −22 dB for the FKE modulator system, and −26 dB for the
QCSE modulator system. These results translate into a lower system noise figure (NF) for the
EA modulators if low optical insertion loss devices can be developed. It is important to note that
the QCSE modulator structure used in these experiments is not optimized. This optimization

11

process involves improving the material quality of the quantum wells as well as modifying the modulator geometry to increase Γ. When optimized, the performance of the QCSE modulator should be comparable to that demonstrated by the FKE modulator.
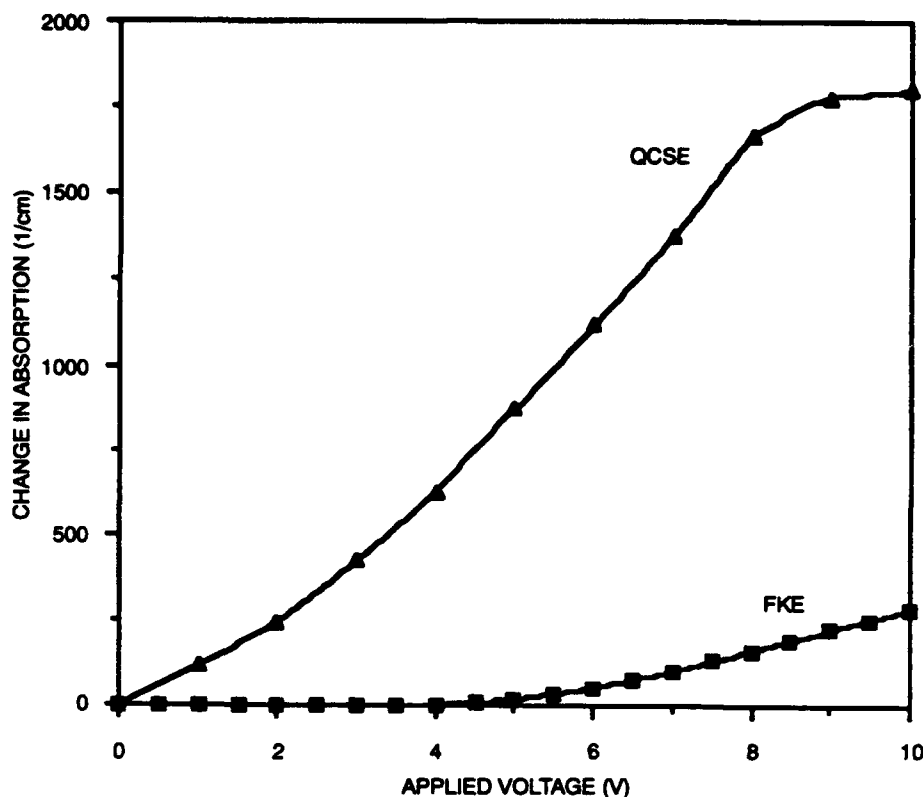
Figure 2-8. Experimental values for $\Delta\alpha$ versus applied bias for the 1.32-μm FKE and 1.52-μm QCSE waveguide modulators.

The SFDR of the MZ, FKE, and QCSE modulator systems will now be addressed. For the externally modulated link, with the above-used laser, detector, and laser-to-detector loss parameters, a detector optical power of 2.5 mW is expected for each link. Again, this assumes $t_m = 0.5$ for all three systems. With these detector optical power levels, as will be discussed in Section 2.2.2, the fiber optic links are shot-noise-limited. This assumes a laser relative intensity noise (RIN) of –165 dBc/Hz, which is well below the thermal and shot-noise contributions at these detector optical powers. This demonstrates the importance of minimizing the modulator insertion loss as well as using a high-power, low RIN laser in obtaining shot-noise-limited operation.

The receiver signal power and spurious signals due to intermodulation products and harmonics for the MZ, FKE, and QCSE modulator systems are graphed versus modulation index in figures 2-9 to 2-11, respectively. A normalized receiver bandwidth of 1 Hz, which determines the system noise floor, is used for these simulations. The result is that a 108-dB SFDR in a 1-Hz bandwidth can be expected for the MZ system. This result agrees well with actual two-tone distortion measurements performed on this link which yielded a 102-dB/Hz$^{2/3}$ SFDR with a 10-mW laser power and a 109-dB/Hz$^{2/3}$ SFDR with a 50-mW laser. Ideal biasing at the quadrature point is assumed for this calculation. The spurious signals are obtained by expanding

12
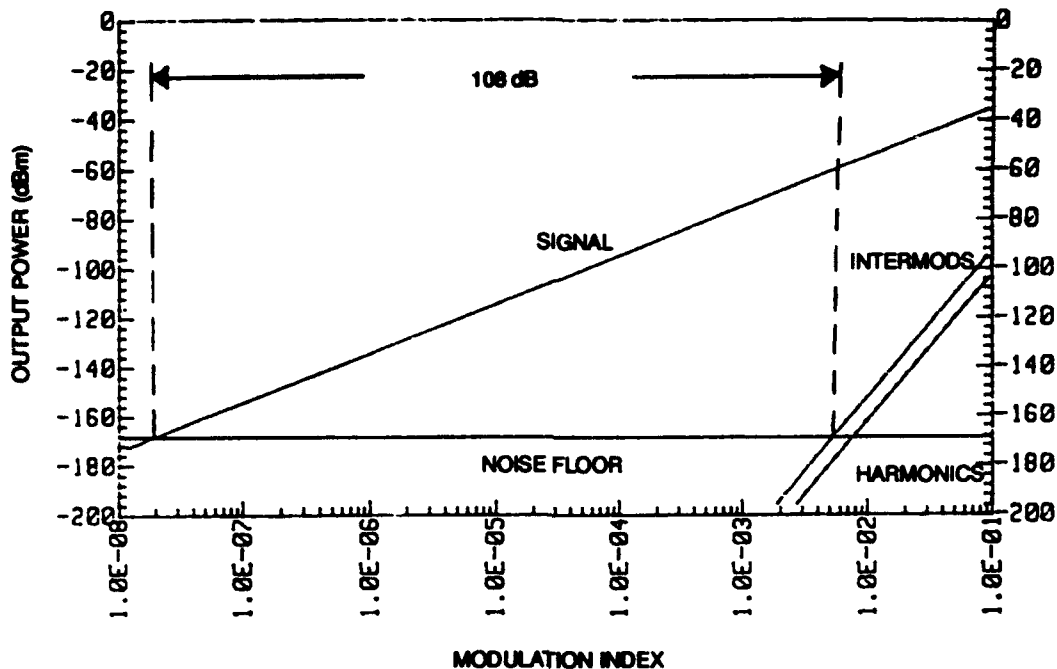
Figure 2-9. Optical receiver output power versus modulation index, including harmonics and intermodulation products for the 1.32-μm MZ modulator.
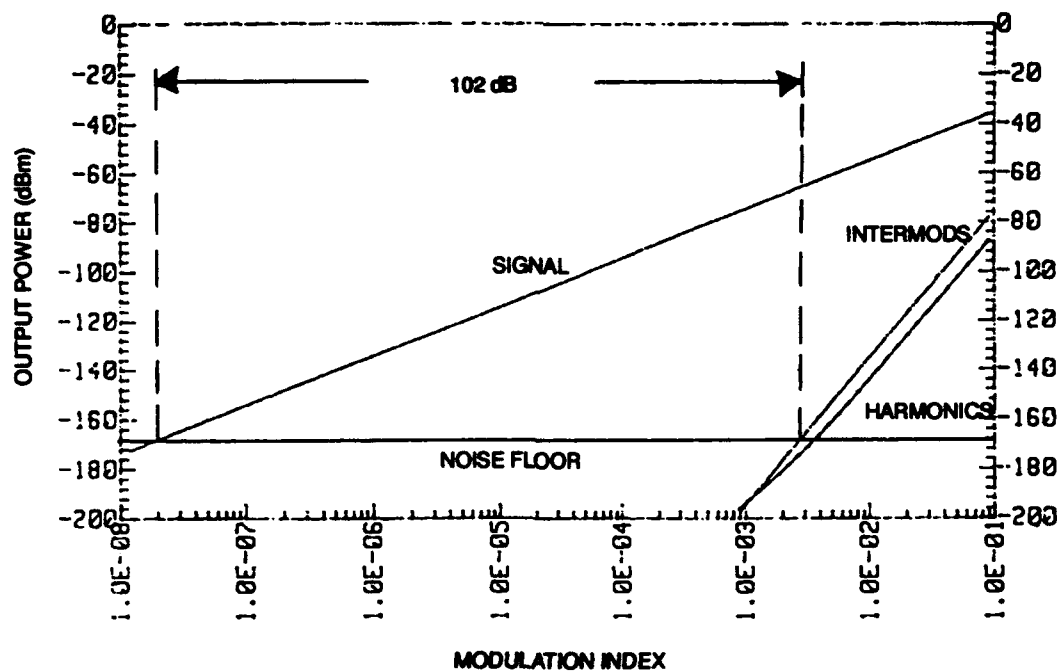
Figure 2-10. Optical receiver output power versus modulation index, including harmonics and intermodulation products for the 1.32-μm FKE modulator.

13
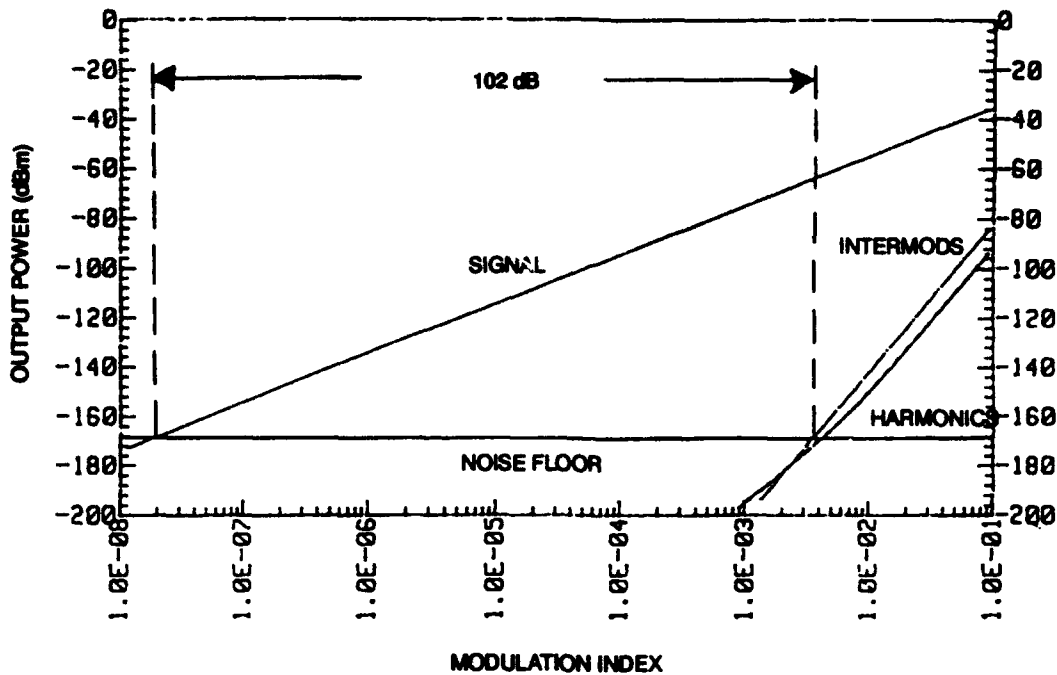
Figure 2-11. Optical receiver output power versus modulation index, including harmonics and intermodulation products for the 1.52-μm QCSE modulator.

the modulator optical power transfer function in a Taylor series and evaluating the nonlinear terms appropriately.[15] Using the experimental modulator transfer curves of figure 2-7, SFDRs of 102 dB and 105 dB in 1-Hz bandwidths are obtained for the FKE and QCSE modulator systems, respectively. Hence, not much difference in dynamic range performance is expected using either an EA or MZ optimally biased modulator. At the chosen bias positions, all three of these modulators were limited by the third-order intermodulation product and not the fundamental harmonics. For broadband systems such as in shipboard EME monitoring, the harmonics as well as the intermodulation products are important. It is important to note that the resultant dynamic ranges for the EA modulators were not as sensitive to bias position as the MZ modulator dynamic range within the 0.2 to 0.8 relative transmission ranges. This indicates that the SFDR performance of the exponential transfer function is less sensitive to bias position than the cosine-squared transfer function. This can be important in field-deployed situations where environmental fluctuations, which can affect the modulator bias position, are unavoidable. In the case of temperature fluctuations, significant modulator bias point drift can be expected. Hence, the EA modulators seem to be very competitive with the state-of-the-art lithium niobate MZ modulator in link performance.

The electrical power out of the antenna can be expressed in terms of the externally modulated fiber optic link parameters as

$$P_A = (t_m \ P_o \ m/2r_m)^2 \tag{2.6}$$

where m is the modulation index. For the MZ system, this gives

$$P_A = (m^2 \ V_\pi)/[2\pi^2 \ R_m \ (1 - \rho_m^2)] \tag{2.7}$$

14

and for the EA system

$$P_A = m^2/[2\ R_m\ (1 - \rho_m^2)\ \Gamma^2\ L^2\ (d\Delta\alpha\ /dV)^2)] \qquad (2.8)$$

Using the minimum detectable modulation indices given in figures 2-9 to 2-11, the minimum detectable antenna power in a 1-Hz receiver bandwidth is P_A(min) = –135 dBm for the MZ system, P_A(min) = –146 dBm for the FKE system, and P_A(min) = –142 dBm for the QCSE system. Again, these numbers assume equal modulator optical insertion losses of 3 dB, an assumption which remains to be demonstrated for the semiconductor devices. Nevertheless, excellent link sensitivity is expected, which translates into fairly low electric field sensitivities.

The system bandwidth of the EO EME monitoring system is ultimately limited by the modulation bandwidth of the optical modulators. For the MZ modulator, the bandwidth is 18 GHz with an assumed V_π = 10 V. A high-frequency V_π of closer to 30 V is actually measured with this lithium niobate MZ modulator. If the manufacturer-specified V_π value is used, a 0.56 V/GHz bandwidth-efficiency figure of merit results, which when extrapolated to beyond 40 GHz, implies devices with $V_\pi \approx$ 25 V. For the EA modulators, device capacitances in the 0.2-pF range are routinely attained with the FKE devices, which implies cutoff frequencies greater than 30 GHz with $V_b \approx$ 5 V. An experimental frequency response curve of the the 1.32-μm FKE modulator is shown in figure 2-12. At 20 GHz, the highest measurement frequency currently available, the response is less than 1 dBe down from its low-frequency response. This device possessed a 7-V on/off voltage, which translates into a bandwidth-efficiency figure of merit of better than 0.5-V/GHz, which already exceeds that of current lithium niobate MZ modulators. With optimized EA modulator structures, it is expected that the bias voltages required to obtain these extremely large bandwidths can be reduced to less than 5 V, which is a significant improvement over that attainable with comparable lithium niobate MZ modulators. A 1.5-μm quantum well waveguide modulator with a 3-dBe bandwidth exceeding 40 GHz at 5-V bias voltage has been reported,[16] which does demonstrate the usefulness of these modulators for ultrawideband applications.

The most useful and revealing parameters to evaluate the performance of the fiber optic sensing system are the link signal to-noise (S/N) ratio and the link NF. The S/N ratio will be considered first. The available output electrical signal power is given by

$$P_{sig} = (m^2/2)\ I_D^2\ R_{out} \qquad (2.9)$$

where I_D is the optical detector time averaged photocurrent, and the other parameters were previously defined. Three system noise sources are considered important: shot noise, thermal noise, and laser RIN noise. The available shot noise power is given by

$$P_{shot} = 2\ q\ I_D\ R_{out}\ B \qquad (2.10)$$

where q is the electronic charge and B is the receiver bandwidth. The available thermal noise power is given by

$$P_{th} = K\ T\ B \qquad (2.11)$$

>S21   log MAG
REF -70.0 dB W/A
2   3.0 dB/
V -0.9023 dB

MARKER 1-1
0.0 Hz
0.0 dB

MARKER 2-1
19.87 GHz
-0.9023 dB

Fermionics Modulator #LPE

SCALE
3.0 dB/div

START   0.130000000 GHz
STOP   20.000000000 GHz

6 Jan 1994 15:45
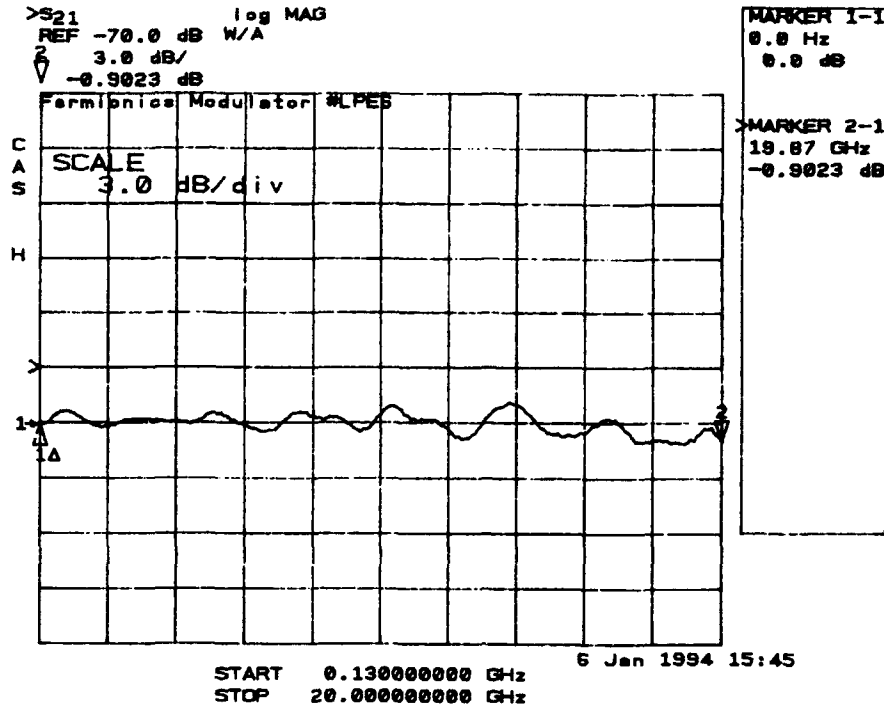
Figure 2-12. Frequency response curve for 1.32-μm LPE-grown
FKE modulator.

where K is Boltzman's constant and T is the receiver temperature. At room temperature, P_{th} = -174 dBm/Hz. The available laser noise power is given by

$$P_L = I_D^2 \, RIN \, R_{out} \, B \tag{2.12}$$

where the RIN value is usually specified for each laser or can be measured. The inverse of the link S/N ratio can then be expressed as

$$1/(S/N) = 2B/m^2 \, [(RIN) + (2q/I_D) + (KT/R_{out}I_D^2)] \tag{2.13}$$

where the first term in the bracket represents the laser noise contribution, the second term represents the shot noise contribution, and the third term represents the thermal noise contribution. Depending on the values of RIN, R_{out}, and I_D, the system is either shot-noise-limited, RIN-limited, or thermal-noise-limited. A plot of $m^2/(S/N)$ in a 1-Hz bandwidth versus I_D is shown in figure 2-13 for R_{out} = 50 Ω and different values of the laser RIN. This curve demonstrates the importance of obtaining a laser with a very low RIN value.

The fiber optic link NF is probably the most important parameter which can be measured, for it ultimately determines the detection sensitivity limit. The link NF is defined as

$$NF = 10 \, \log_{10} \, [(S/N)_{input}/(S/N)_{output}] \tag{2.14}$$

which can be expressed in terms of the link parameters as

$$NF = - \, 10 \log_{10}(H^2) + 10 \log_{10}[P_{th}(1 + H^2) + P_L + P_{shot}]/P_{th} \tag{2.15}$$

16
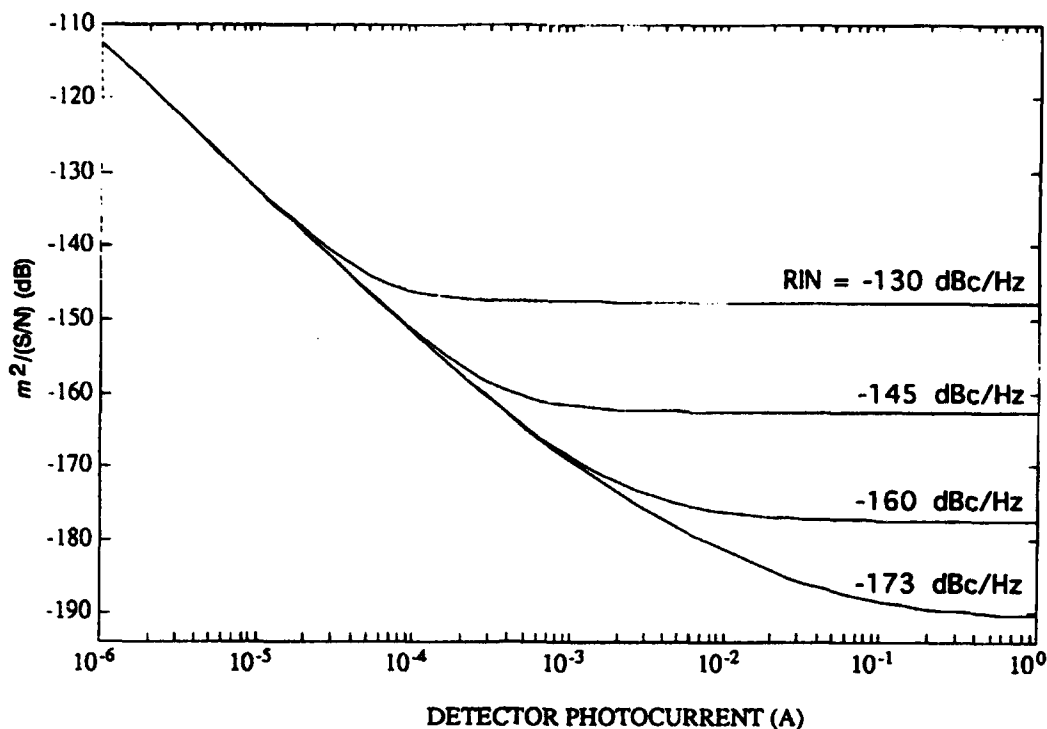
Figure 2-13. Plot of $m^2/(S/N)$, where m is the modulation index, in a 1-Hz bandwidth versus optical detector photocurrent for different laser RIN values.

where H^2 is the RF insertion loss given by Eq. 2.3. It is assumed in this NF expression that the input and output thermal noise powers are identical. For the MZ and EA modulator links, the expected NFs are 28 dB for the FKE system, 32 dB for the QCSE system, and 39 dB for the MZ system. Again, a clear advantage for the EA modulators if low optical insertion loss can b. achieved. Experimental results from a breadboarded MZ fiber optic link will now be discussed and compared with these simulated results.

2.3 PERFORMANCE OF FIBER OPTIC LINK

In this section, the best available 2-MHz to 18-GHz fiber optic link will be described. A diagram of the externally modulated fiber optic link is shown in figure 2-14. The 1.32-μm Nd:YAG laser (Amoco Model ALC1320-50S) has a fiber pigtail output power of 45 mW and a measured RIN value of approximately –170 dBc/Hz. The lithium niobate MZ modulator (GEC–Marconi Model Y-35-8808) has an optical insertion loss of 3.6 dB and a low frequency $V_\pi = 13.5$ V. The modulation frequency response of this modulator is shown in figure 2-15, which reveals a 3-dBe bandwidth of approximately 17 GHz. The InGaAs p-i-n photodiode (Fermionics Model HSD-30) has a fiber-coupled responsivity of $r_d = 0.7$ A/W at an optical wavelength of 1.3 μm. A 3-dBe modulation bandwidth exceeding 16 GHz was measured for this optical detector. The overall fiber link frequency response is plotted in figure 2-16, which shows a 10-dBe falloff in response from 50 MHz to 18 GHz (3-dBe bandwidth of 11 GHz). The fiber link loss budget is depicted in figure 2-17, which displays an optical loss from laser to detector of 10 dB, a value that includes the 3 dB for modulator biasing. The total noise power ($P_{th} + P_{shot} + P_L$) of this link as a function of optical detector photocurrent is plotted in

17
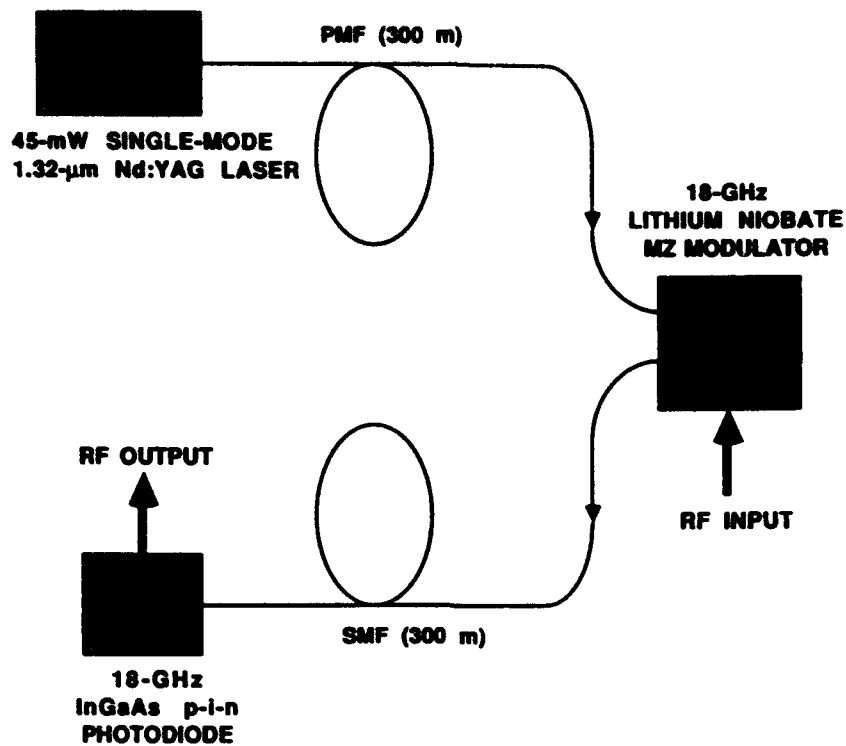
Figure 2-14. Schematic diagram of best available DC to 18-GHz externally modulated fiber optic link.
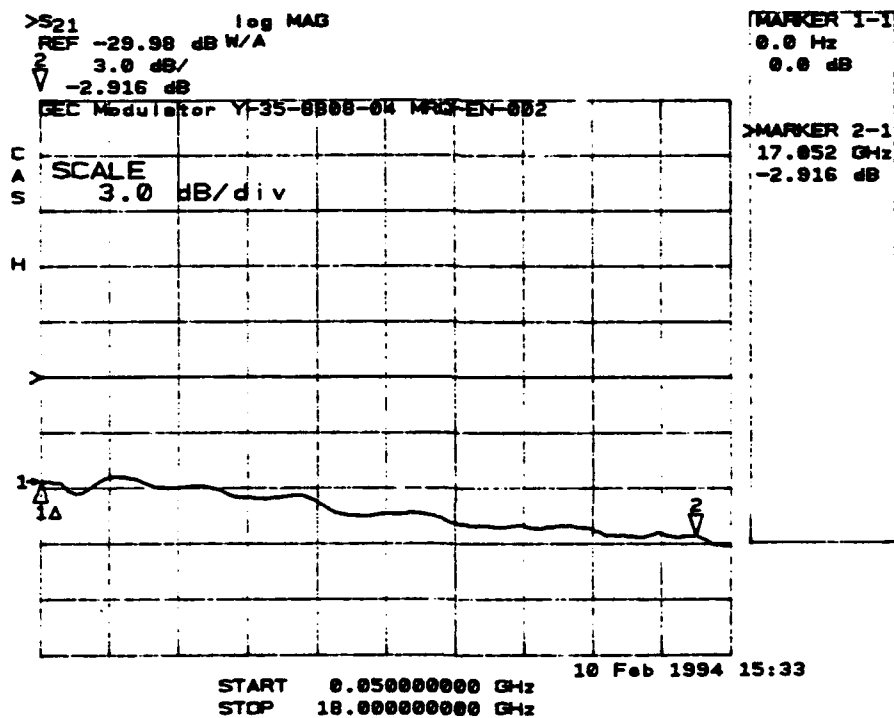
Figure 2-15. Modulation frequency response of wideband lithium niobate optical modulator.

18
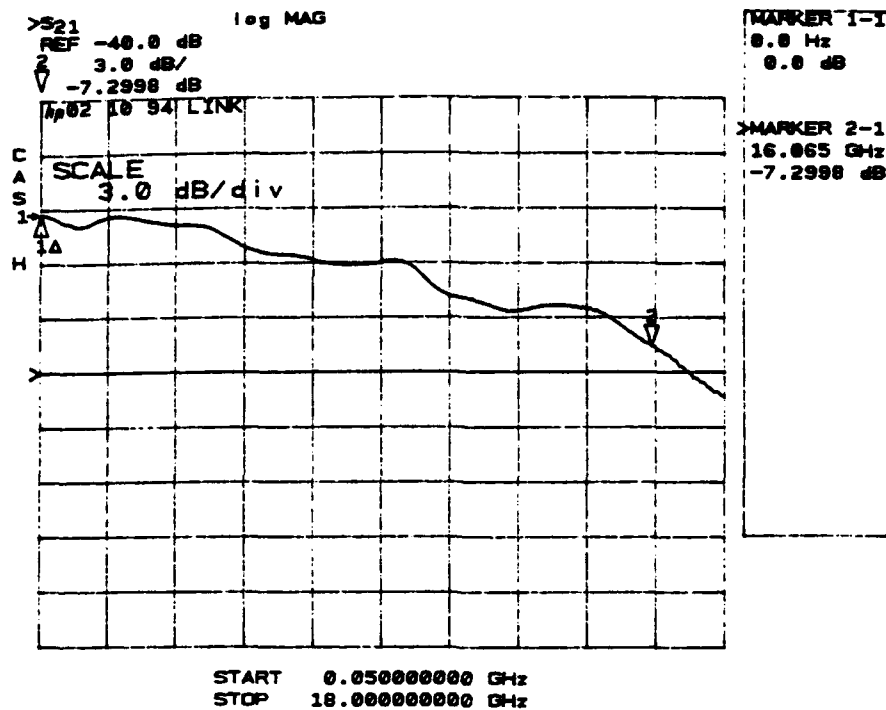
Figure 2-16. Externally modulated fiber optic link RF insertion loss versus frequency in the 50-MHz to 18-GHz range.
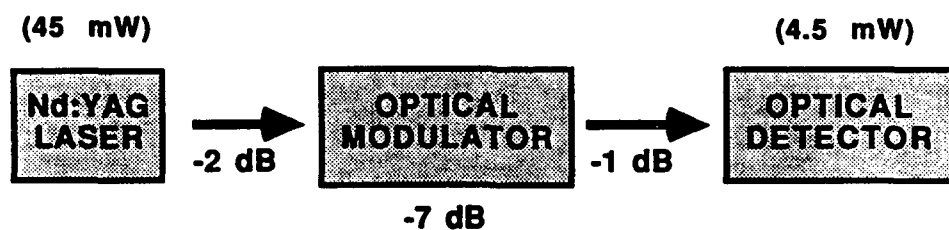
Figure 2-17. Diagram of the externally modulated fiber optic link loss budget.
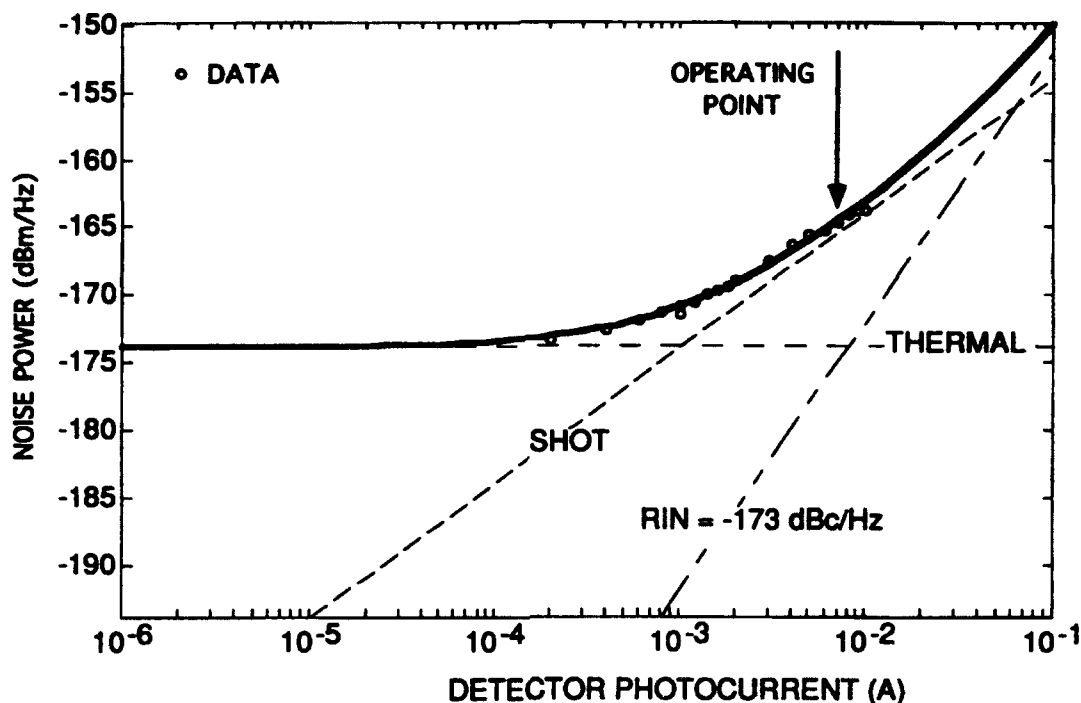
Figure 2-18. Total noise power (solid line) and experimental data (circles) versus
optical detector photocurrent for the externally modulated fiber optic link.

figure 2-18, which shows that the operating point for this system renders shot-noise-limited opera-
tion. The RF insertion loss of this link was measured to be 32 dB at 2 GHz. This is within 3 dB of
the theoretical prediction using Eq. 2.3. The link NF was measured to be 35 dB, 38 dB, and 45 dB
at frequencies of 2, 10, and 18 GHz, respectively. The insertion loss and NF values can be improved
upon by increasing the laser power and decreasing the optical modulator V_π voltage. For compari-
son, the RF insertion loss versus frequency of a 2-MHz to 500-MHz fiber optic link using a optical
modulator possessing a V_π of 4 V is shown in figure 2-19. Here, a link RF insertion loss of 11 dB
and an NF of less than 20 dB are obtained, which demonstrates the importance of maximizing the
modulation responsivity of the optical modulator. With continued laser and ultrawideband modula-
tor R&D, the potential for fiber links with low RF insertion loss can be expected. Two-tone measure-
ments with the 18-GHz fiber optic link show an SFDR of 108 dB/Hz$^{2/3}$. The SFDR is smaller than
the linear dynamic range for this wideband fiber optic system which implies a linear dynamic range
greater than 110 dB/Hz. This link will be field-tested and subsequent shipboard measurements will
be acquired.

2.4 ELECTROMAGNETIC FIELD MEASUREMENTS IN THE 2- to 18-GHZ FREQUENCY RANGE USING AN EO EME MONITORING SYSTEM

Remote electromagnetic field measurements in the 2- to 18-GHz frequency range using an
antenna-coupled externally modulated fiber optic link will be described in this Section. These
measurements have been made with a fiber optic link whose performance was not quite as good
as that described in the previous Section. Nevertheless, an electric field sensitivity of 15 μV/m
and an SFDR of 102 dB in a 1-Hz bandwidth have been measured. The results indicate that this
system is a feasible candidate for remotely measuring extremely broadband, large dynamic range
electromagnetic fields, especially when recent fiber optic link improvements are incorporated.

20
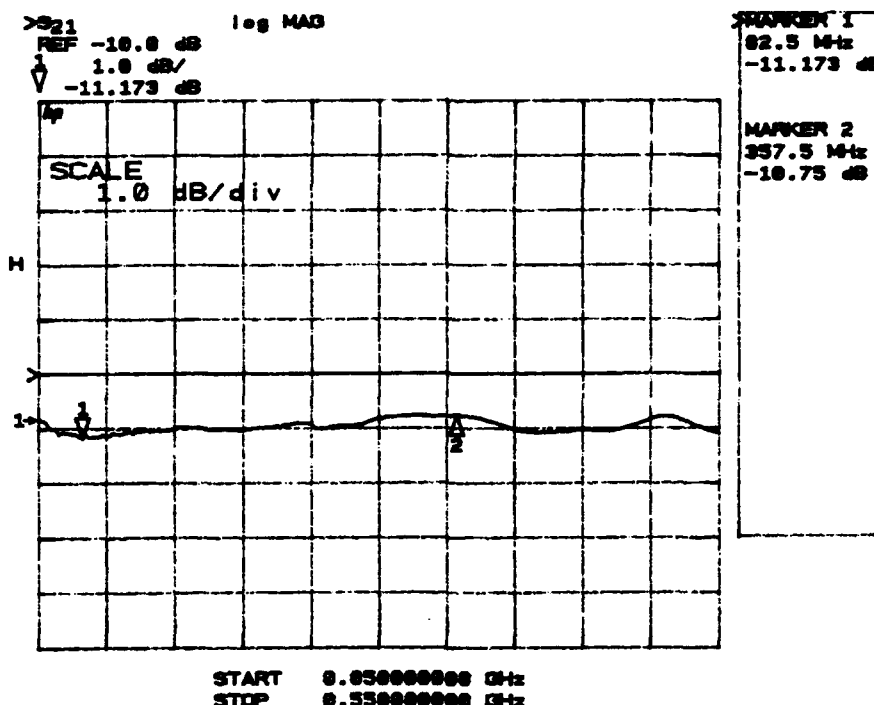
Figure 2-19. RF insertion loss versus frequency for a DC to
500-MHz fiber optic link using a $V_\pi = 4$ V optical modulator.

2.4.1 System Configuration

A schematic diagram of the antenna-coupled electromagnetic (EM) field detection system
used in this early work is shown in figure 2-20. It consists of a cavity-backed spiral antenna
(Transco Model 9C33500), a Ti:indiffused lithium niobate MZ waveguide modulator (GEC-
Marconi Model Y-35-8808) , a 1.32-μm Nd:YAG solid-state laser (Amoco Model
ALC1320-10S), a 100-meter length of PMF single-mode optical fiber (Alcoa-Fujikura Model
N000185), a 100-meter length of SMF (Corning Model SMF28), and a high-speed InGaAs p-i-n
photodiode (BT&D Model PDC4310-30-FP). The electrical output of the broadband antenna
with known characteristics is coupled to the optical modulator and is optically remoted via PMF
for the uplink and SMF for the downlink, with the laser and optical detector remotely located
with the associated processing electronics. In an effort to limit the electrical power requirements
and intrusiveness of the EM field probe, this configuration contains no low-noise amplifier at the
input to the optical modulator. The externally modulated fiber optic link is slightly different
than that described in Section 2.3. The Nd:YAG laser has an output power of 10 mW and a
measured RIN of –173 dBc/Hz. The lithium niobate MZ modulator has a 3-dBe modulation
bandwidth of 18 GHz, a 3.6-dB optical insertion loss, and a low-frequency half-wave voltage of
$V_\pi = 13.5$ V. The optical detector has a responsivity of $r_d = 0.85$ A/W and a 3-dBe modulation
bandwidth of 25 GHz. The fiber optic link and antenna performance were first measured and
calibrated separately and then mated for anechoic chamber testing of the entire EM field
detection system. The results of these experiments will now be discussed.

21
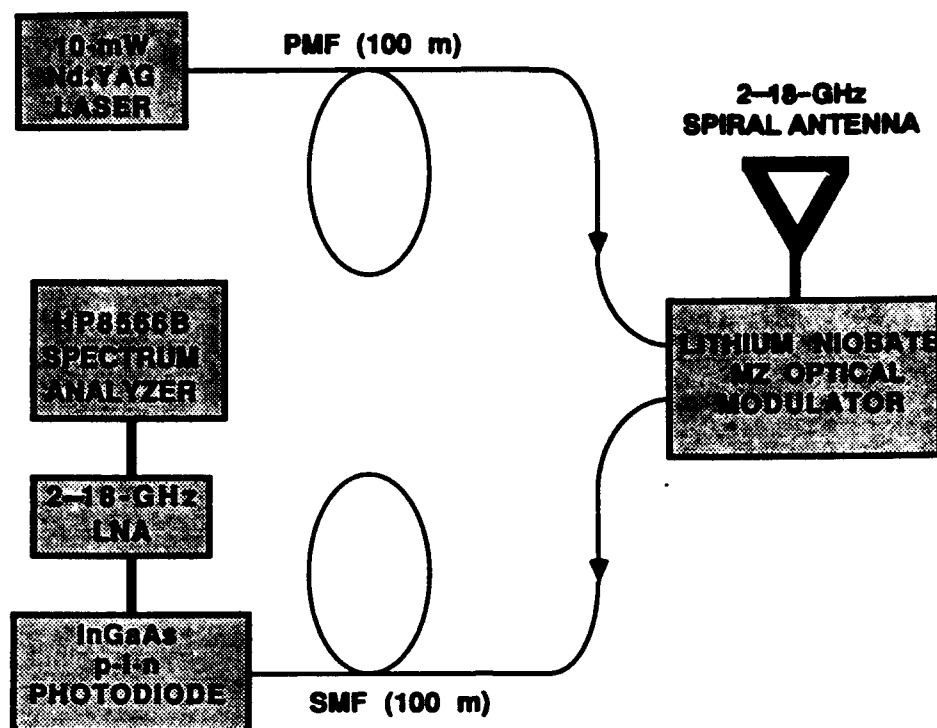
Figure 2-20. Schematic diagram of the antenna-coupled externally modulated fiber optic link for EM field detection.

2.4.2 Results

The fiber optic link and spiral antenna individual system responses in the 2- to 18-GHz frequency range are shown in figure 2-21. The close to 6-dBe roll off in response for the fiber optic link is due to the combined response of the integrated optical modulator (IOM) and the optical detector. The optical insertion loss of this link is 9.0 dB, which includes the 3 dB loss for IOM biasing. The RF insertion loss of this link was measured to be 45 dB at a frequency of 2 GHz. A lower RF insertion loss and hence better performance has since been obtained by employing a higher power laser. The effect of laser optical power on fiber optic link performance is better illustrated in figure 2-22, which graphs the inverse S/N ratio as a function of detector photocurrent. The individual thermal, shot, and RIN noise contributions are plotted to illustrate the thermal-noise-limited, shot-noise-limited, and RIN-limited regions of operation. The operating point for this fiber optic link is borderline between thermal-noise-limited and shot-noise-limited. More optical power would increase the S/N ratio and decrease the NF of the link. Link NF values of 49 dB, 52 dB, and 55 dB have been measured at modulation frequencies of 2 GHz, 10 GHz, and 18 GHz, respectively. Two-tone distortion measurements were performed near 9.5 GHz to determine the SFDR of the link. The theoretical and experimental results of these measurements are summarized in figure 2-23. A 102-dB/Hz$^{2/3}$ SFDR has been empirically measured by fitting the experimental data points for the fundamental and third-order intermodulation power levels to theoretical curves. Excellent agreement is obtained when an IOM V_π of 30 V is assumed instead of the 13.5-V low-frequency value. This discrepancy is not that alarming considering that the two-tone measurements were performed at 9.5 GHz and the V_π of 13.5 V was essentially measured at DC.

22

>S21   log MAG   MARKER 1-1
REF -50.0 dB   0.0 Hz
    3.0 dB/   0.0 dB
▽ -5.7617 dB

OSC modulator/ LED detector   MARKER 2-1
                                                                       18.0 GHz
                                                                       -5.7617 dB

C

S

1

                                                        22 Nov 1991 10:58
START   2.000000000 GHz
STOP   18.000000000 GHz

(a) Fiber optic link.

VSWR: 2.0:1 MAX

POLARIZATION: LHCP

BEAMWIDTH (3 dB): 80 DEG
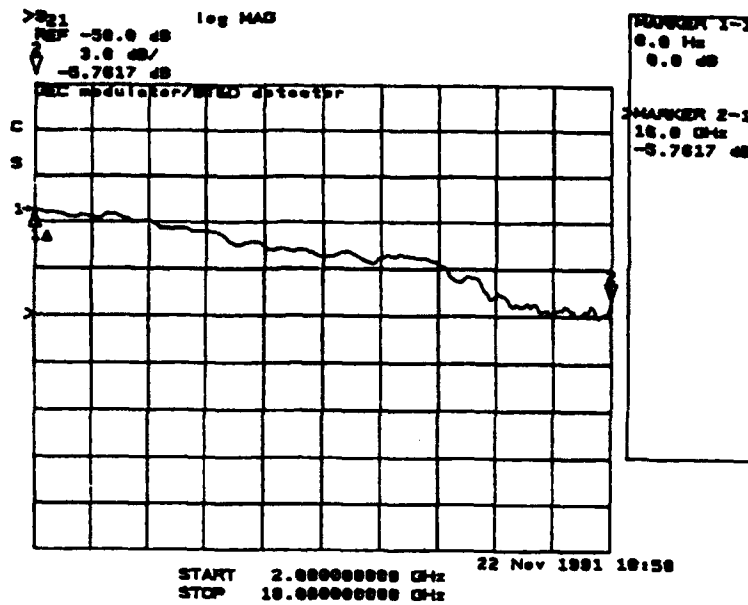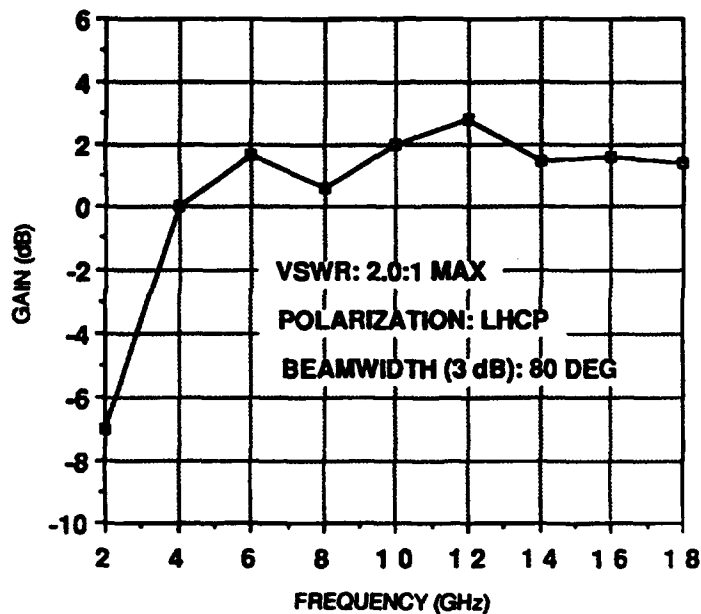
FREQUENCY (GHz)

(b) Spiral antenna.

Figure 2-21. Modulation frequency response from 2 to
18 GHz of the externally modulated fiber optic link
and the spiral antenna.

23
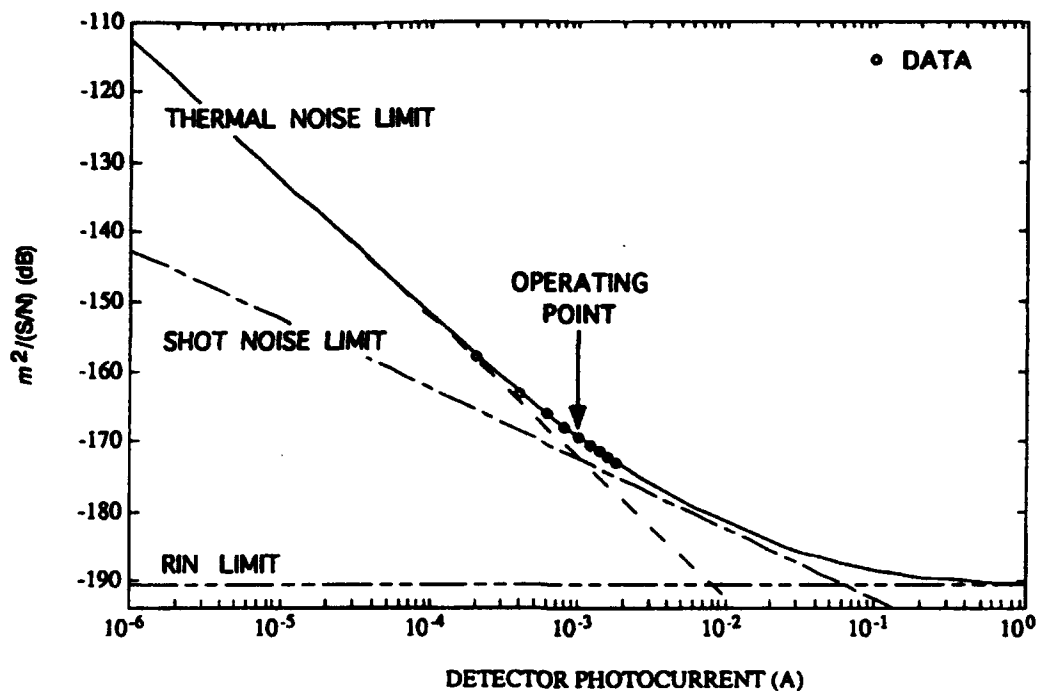
Figure 2-22. Plot of $m^2/(S/N)$, where m is the modulation index, for total noise (solid line), shot noise, thermal noise, and RIN contributions versus detector photocurrent for the fiber optic link used in this work.
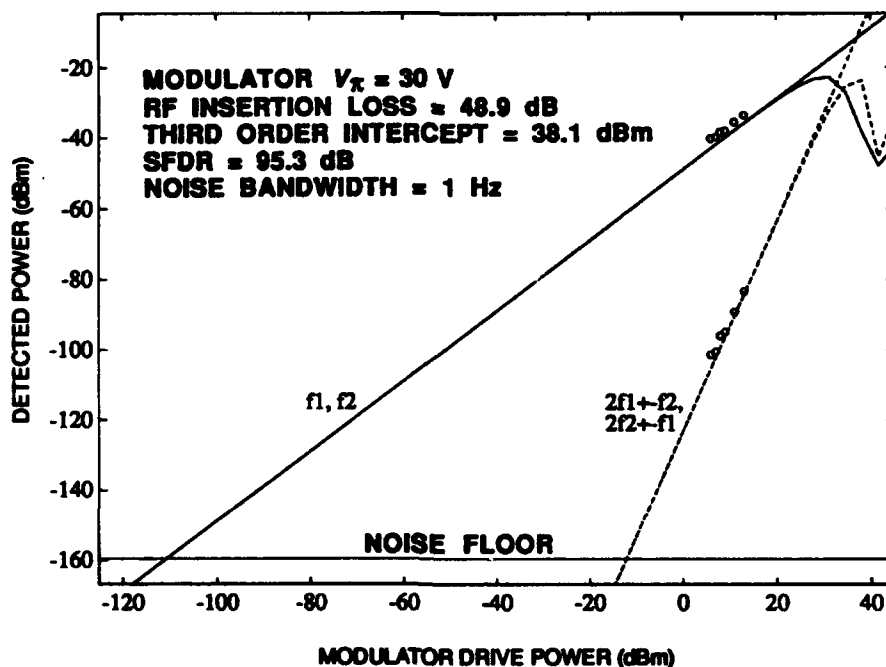
Figure 2-23. Plot of experimental (circles) and theoretical detected power for fundamental (solid line) and third-order intermodulation products (broken line) versus power applied to the IOM.

24

The wideband RF probe used for this work is a 2-inch-diameter cavity-backed spiral antenna whose gain characterisitics were given in Figure 2-21b. It is a left-hand circularly polarized antenna that has a 3-dB beamwidth of 80 degrees and a voltage standing wave ratio (VSWR) of less than 2:1 across the 2- to 18-GHz frequency range. The gain versus frequency characteristics were measured against standard gain horn antennas in the 2- to 18-GHz range for linearly polarized radiation, and > 0 dBi gain exists for frequencies above 4 GHz. The circularly polarized spiral antenna is a good choice for multioctave frequency coverage if a small, passive receive antenna is required.

EM field measurements were made with the antenna-coupled fiber optic link after separate testing of the antenna and link was completed. A 2- to 18-GHz far-field anechoic chamber was used in which to perform the experiments. Measurements were performed at 2.25, 9.52, and 16 GHz using three different standard gain horn source antennas. The spiral antenna output electrical power was calculated from the expression

$$P_A = A_{eff} \, W_{inc}$$

$$= (\lambda^2 G_A/4\pi) \, W_{inc} \tag{2.16}$$

$$= (P_{inp}) \, (G_{tr}) \, (G_A) \, (\lambda/4\pi R)^2$$

where

A_{eff}	=	effective aperture of spiral antenna (m^2)
W_{inc}	=	RF intensity incident on antenna (W/m^2)
P_{inp}	=	RF power applied to transmit antenna (W)
G_{tr}	=	gain of transmit antenna (dBi)
G_A	=	gain of spiral antenna (dBi)
λ	=	RF source wavelength (m)
R	=	propagation length (m)

The "actual" electric field strength at the probe site was calculated from the expression

$$E_A = (2 \, \eta \, W_{inc})^{1/2} \quad (V/m) \tag{2.16}$$

where $\eta = 377 \, \Omega$ is the free space impedance. The "measured" electric field strength was obtained using Eq. 2.17 along with the fiber optic link RF insertion loss data. Starting with the electrical power out of the optical detector, P_A was deduced by factoring in the fiber optic link loss. From P_A, the incident RF intensity W_{inc} was determined, and from that the electric field strength was found. It is important to have an accurate calibration of both the spiral antenna gain and the fiber optic link loss as a function of frequency if precise electric field measurements are to be made.

The EM field detection system response for boresight radiation at the three frequencies investigated is shown in figure 2-24. In this figure, the electrical output power of the optical

detector is plotted versus incident RMS electric field strength. A 10-Hz spectrum analyzer resolution bandwidth was used in this measurement. Extremely linear response is obtained from the highest field levels down to the minimum detectable levels for each frequency investigated. To assess the accuracy of these field measurements, electric field values were obtained from the detected optical power levels, since the RF insertion loss of the link as well as the gain of the antenna were known. The result of this measurement is shown in Figure 2-25 where measured field strengths are plotted versus calculated electric field strengths. There is some deviation from expected field levels, which is attributed to the anechoic chamber testing procedure. The pointing accuracy for the three relatively high gain horn antennas was not precisely controlled, resulting in actual electric field levels that differed from the calculated levels. Nonetheless, RMS electric field sensitivities of approximately 15 μV/m, 44 μV/m, and 107 μV/m have been achieved in a 1-Hz resolution bandwidth for the 2.25, 9.52, and 16-GHz frequencies, respectively. The RMS electric field detection ranges for the three frequencies investigated are summarized in table 2.1. These experimentally attained electric field detection ranges imply that this system can be useful for remotely performing broadband, large dynamic range electric field measurements.
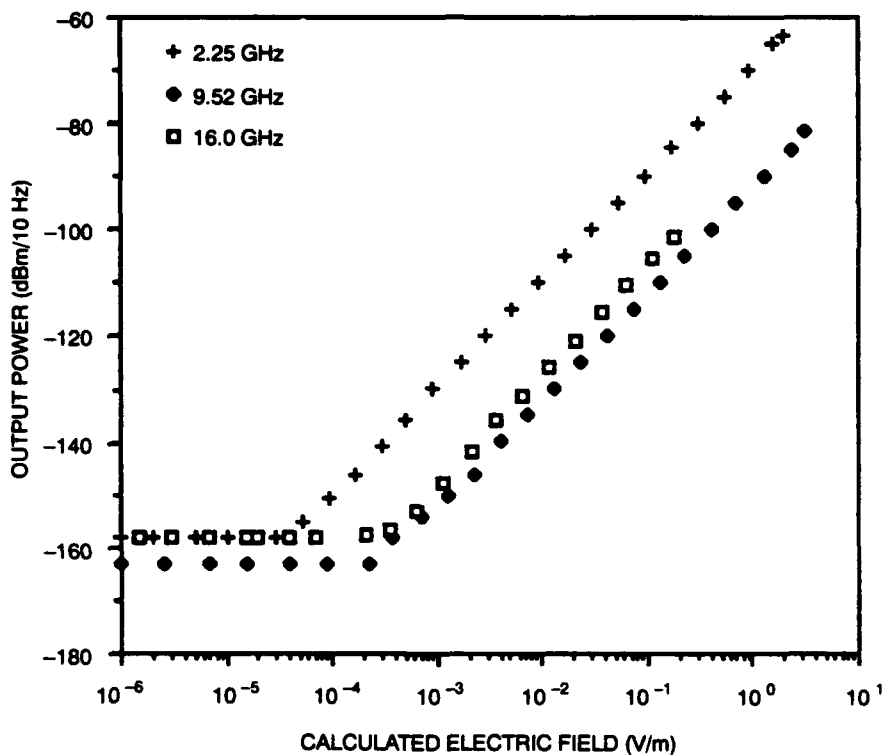
Figure 2-24. EM field detection system output versus incident RMS electric field level.
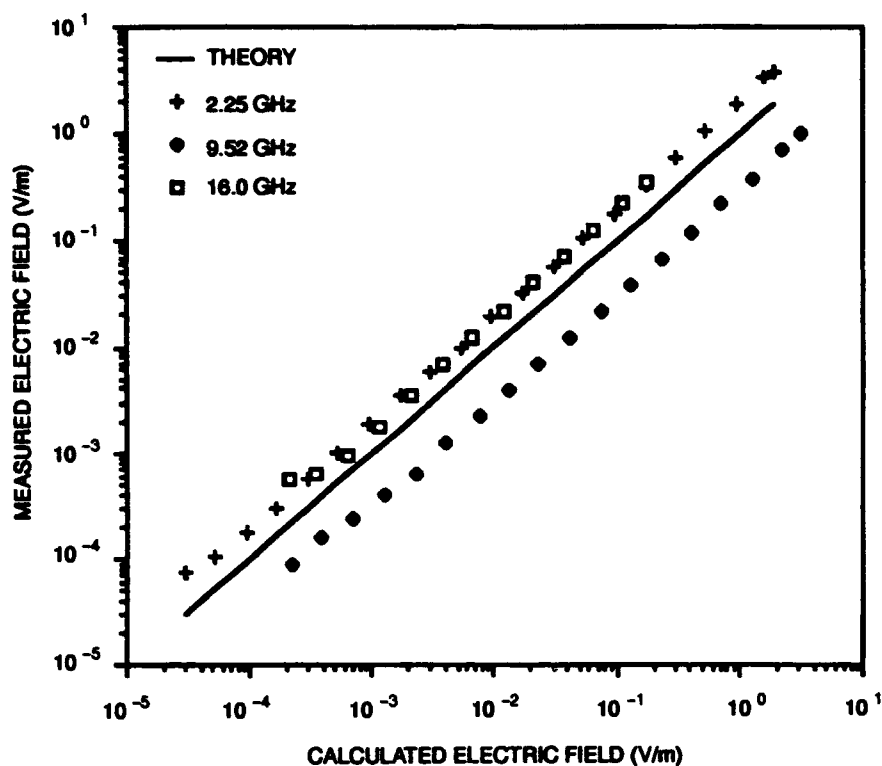
Figure 2-25. Measured RMS electric field levels versus calculated RMS electric field levels.

Table 2.1. Externally modulated EO EME monitoring system electric field level detection ranges at 2.25, 9.52, and 16.0 GHz.

Frequency (GHz)	RMS Electric Field Detection Range	
	(1 Hz Bandwidth)	(1 kHz Bandwidth)
2.25	15 μV/m – 0.8 V/m	0.02 V/m – 90 V/m
9.52	44 μV/m – 6 V/m	0.04 V/m – 550 V/m
16.0	107 μV/m – 17 V/m	0.1 V/m – 1585 V/m

3.0 IMPROVEMENTS TO EO EME MONITORING SYSTEM

The Phase I testing of the breadboarded EO EME monitoring systems proved quite valuable in assessing the technology and determining areas of further development. In this Section, system improvements and modifications which have been implemented as part of the Phase II efforts associated with this program will be discussed. Performance improvements in the fiber optic link and wideband RF probes have been attained. One improvement is the development of stable, remote optically powered and controlled fiber optic links, and another is remote polarization control of fiber optic links. Link performance improvements have been achieved due to the insertion of superior optical components. The current status of the ultrawideband antenna development efforts will be reviewed. The fiber optic link improvements and modifications will be discussed first.

3.1 IMPROVEMENTS TO FIBER OPTIC LINK

The performance of analog photonic components has been steadily improving year by year. Since the start of this R&D effort in FY 91, significant advances have been made in the areas of solid-state laser and optical modulator technology, and these advances affect the performance of the EO EME monitoring system. In this section, fiber optic analog link performance improvements and link modifications during Phase II of this effort will be discussed.

The link performance of the "best available" 18-GHz fiber optic link has been measured. This link is similar to that described in Section 2.3, but has slightly superior optical components and is the link to be used in the FY 94 shipboard demonstration under this project. It consists of a 50-mW Nd:YAG laser (Amoco Laser Company Model ALC1320-50S), a 300-meter length of PMF (3M Model FS-HB-6621) for the uplink, a 300-meter length of SMF (Corning Model SMF28) for the downlink, an 18-GHz optical modulator (UTP Model APE MZM-1.3-18-T-01), and an 18-GHz InGaAs p-i-n photodiode (Fermionics Corporation Model HSD30). Postdetection amplification with a low-noise amplifier (LNA) is implemented to reduce the overall NF of the receiver. The spectrum analyzer used in this work (Hewlett Packard Model 8566B) has an NF of approximately 40 dB.

The fiber optic link transfer function (electrical in/electrical out) is shown in figure 3-1. An RF insertion loss of 35 dB is shown at 18 GHz along with a 3-dBe link bandwidth of 15 GHz. This system possesses an NF of less than 35 dB at 2 GHz as well as an SFDR of >100 dB/Hz$^{2/3}$. This link has been calibrated, packaged, and is currently undergoing environmental testing, which continues into Phase III of this effort.

To address the > 18-GHz system requirements, current R&D efforts include a 40-GHz lithium niobate MZ modulator being developed by Boeing, a 40-GHz III-V semiconductor EA modulator being developed by Fermionics, and a 50-GHz III-V semiconductor MZ device procured from GEC–Marconi Materials Technology. The status of these R&D efforts will now be discussed.

3.1.1 Ultrawideband Optical Modulators

Efforts to further develop the semiconductor EA modulators for shipboard analog photonic link applications are continuing. A Navy development program with Fermionics Corporation is directly supporting the shipboard EME monitoring effort. The purpose of this Office of Naval
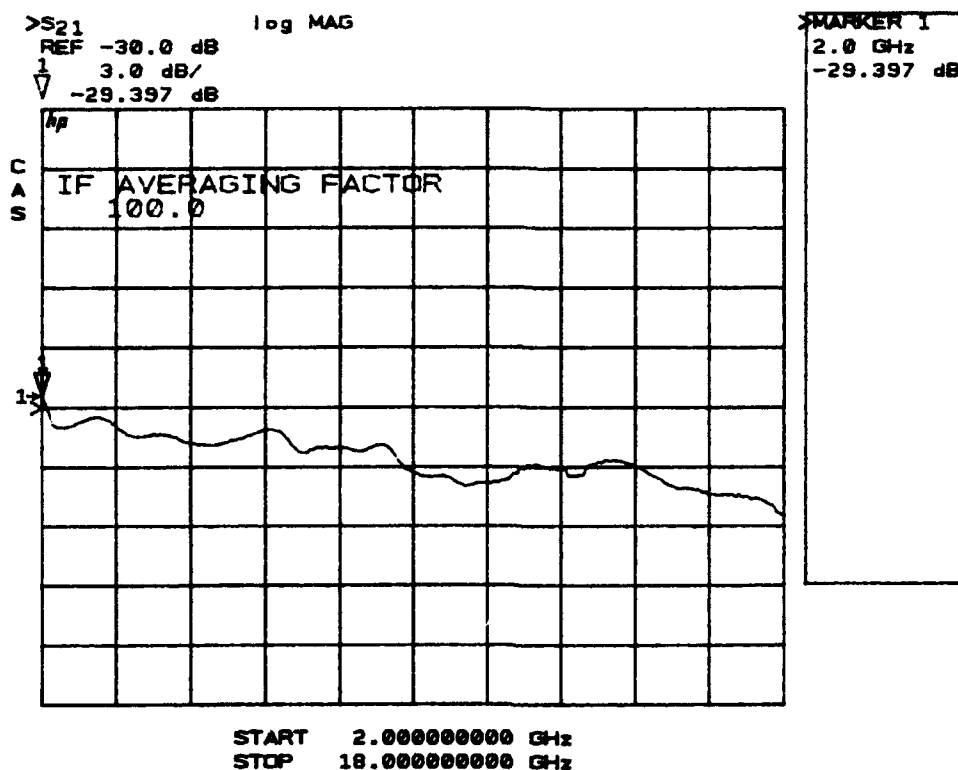
Figure 3-1. Fiber optic link transfer function.

Research-sponsored and NRaD-administered effort is to develop a high-speed III-V semiconductor EA modulator. The objective of the work is to commercialize a 40-GHz InGaAsP/InP FKE modulator operable at a wavelength of 1.32 μm for digital as well as analog optical link applications. The operation of the FKE modulator was discussed in Section 2.1.2 of this report. At present, a >20-GHz fiber-pigtailed modulator has been delivered to the Navy.[17,18] This device suffers from a rather large optical insertion loss (8.8 dB) and only a moderate RF efficiency (10 dB with 7 V voltage swing). Theoretical simulations and other experimental work suggest that these parameters can be significantly improved. Nevertheless, this device is being tested for shipboard use. Current work is focused upon improving the modulator performance parameters and delivering a 40-GHz semiconductor EA modulator in FY 94.

Under direct NRaD sponsorship supporting the EO EME monitoring task, Boeing is developing a wideband traveling-wave lithium niobate MZ modulator. The goal of this effort is to deliver an MZ modulator which is suitable for operation at 1.3 μm, is operable from DC to 40 GHz, has a V_π of <15 V at 40 GHz, an extinction ratio of >20 dB, and a fiber-to-fiber optical insertion loss of <3 dB. To date, Boeing has produced > 20-GHz bandwidth optical modulators and it intends to slightly modify the structure to efficiently achieve a >40-GHz modulation bandwidth. A 40-GHz lithium niobate optical modulator possessing the performance specifications stated above is to be delivered to the Navy for testing in FY 94.

A wideband III-V semiconductor MZ optical modulator has also been procured from GEC–Marconi Materials Technolgy. According to specifications, this device is to operate at 1.3 μm, be operable from DC to 50 GHz, and have an RF V_π = 10 V, a >20-dB extinction ratio, and an optical insertion loss of <11 dB. The specifications for this modulator are excellent in all

29

areas except the optical insertion loss. As this technology advances, lower fiber-to-fiber optical insertion losses should be attained. The GaAs-based modulator with a < 11-dB optical insertion loss is to be delivered to the Navy for testing in FY 94.

The suitability of these three wideband optical modulator approaches for shipboard EME monitoring will be experimentally determined in FY 94 and recommendations will be forthcoming.

3.1.2 Optically Powered and Controlled Remote Fiber Optic Links

Many fiber optic antenna remoting applications, including shipboard EME monitoring, require standoff electrical powering of the antenna-coupled components. Self-contained battery packs are one solution. However, batteries possess a finite lifetime that can limit their usefulness for many applications. In some cases, the optical powering can be accomplished using a PBL system, which has the advantage that all-dielectric fiber optic cables can be used. This can be essential for applications like the EME monitoring system, where EMI effects are to be minimized. In addition, for multioctave externally modulated fiber optic links, the electrical biasing of the optical modulator is critical in minimizing nonlinear distortion. Although accurate methods of passively biasing the modulators are being investigated,[19] the environmental stability of the bias position has not been established. Consequently, active modulator biasing is also under investigation. Combining remote optical powering and remote optical modulator bias control has been demonstrated.[20,21] Here, we will demonstrate this technique with two multioctave fiber links and show how accurately the bias point must be controlled in order for no dynamic range penalty to result.

The two externally modulated fiber optic links investigated in this work operated from 30 to 500 MHz (proton exchange modulator) and from 2 to 18 GHz (titanium diffused modulator). Each link consists of a 1.32-μm Nd:YAG laser, PMF for the uplink, a lithium niobate MZ modulator, SMF for the downlink, and a high-speed photodiode. The PBL system consists of a high-power AlGaAs laser diode array, a multimode optical fiber (100 μm/140 μm), and a high-efficiency GaAs photocell. The AlGaAs laser diode is intensity-modulated at low frequency ($\approx$ 100 Hz) to introduce a reference modulation onto the optical modulator. The second harmonic of this low-frequency modulation is then remotely detected and analyzed using a lock-in amplifier. The output of the lock-in amplifier is used to actively control the optical power of the AlGaAs laser diode, which in turn controls the optical modulator bias position. A schematic of this fiber optic system is shown in figure 3-2. The performance requirements and the ability of this optical powering and biasing control technique to minimize modulator-induced harmonic distortion over wide temperature ranges will now be discussed.

The PBL unit consists of a 250-mW AlGaAs laser diode array (Spectra Diode Labs. Model SDL-2432-P2) emitting at 810 nm which is directly coupled into an optical fiber with a core diameter of 100 μm (manufactured by Spectran Corp.). At the modulator side of the link, the optical power is converted to electrical power using a 12-V GaAs photocell (Photonic Power Systems Model PPC-12S-ST). Approximately 50 mW of optical power is delivered through the optical link to the photocell. A graph of the output voltage as a function of series resistance for an input power of 50 mW is shown in figure 3-3. A series resistance of 2.7 kΩ is chosen which allows for an output voltage of between 0 and 12 V to be obtained. A plot of the output voltage as a function of input optical power is shown in figure 3-4. Very little current is required (<< 1 mA) to drive the modulators, from which it can be inferred that very little electrical power
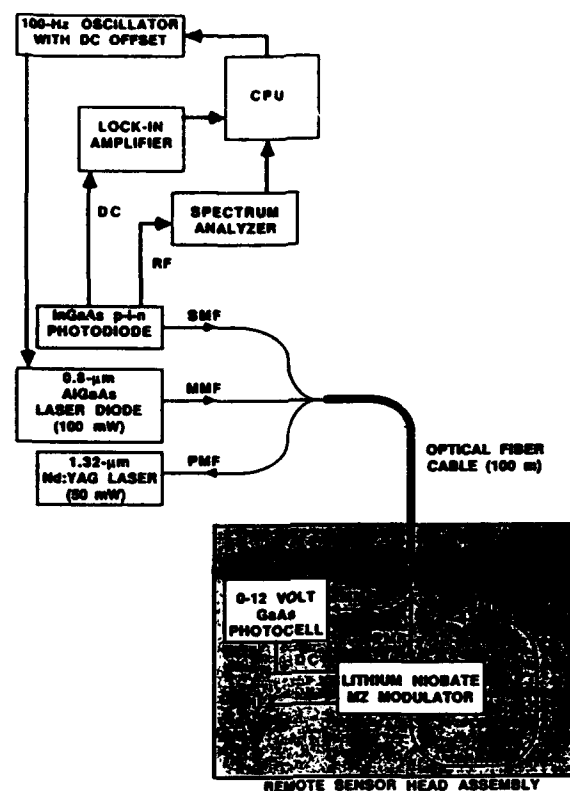
Figure 3-2. Schematic of optical powering system and modulator bias control circuitry.
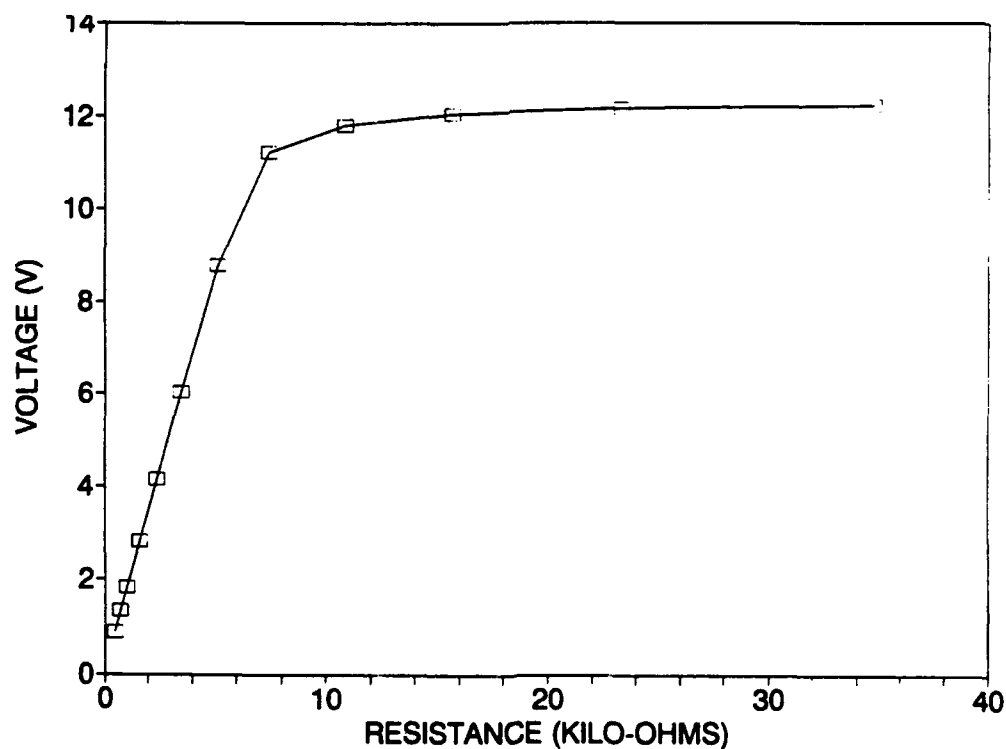
Figure 3-3. Photocell output electrical voltage as a function of series resistance for 50-mW input optical power.
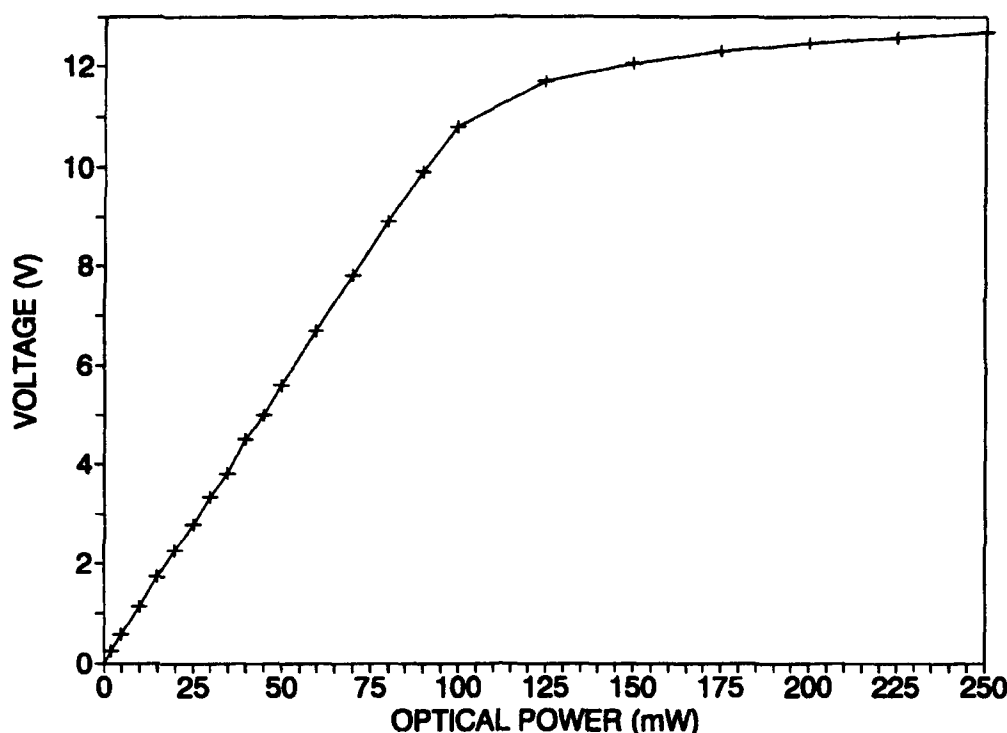
Figure 3-4. Photocell output voltage versus input optical power using a
2.7-kΩ series resistance.

(voltage X current) is required for this remote unit. A 0.47-μF capacitor is placed in series with
the 2.7-kΩ resistor to damp out voltage fluctuations caused by transmitted optical power
fluctuations through the multimode fiber. The transmitted optical power is modulated with a
100-Hz small modulation depth signal for the modulator bias control. This optical powering
technique allows for the modulator voltage to easily be changed simply by varying the trans-
mitted optical power.

The requirement for the fiber optic link is that the SFDR is not reduced by any error in
biasing the modulator. The reciever signal powers for the fundamental through the third-order
intermodulation product for the MZ link excited with equal intensity RF tones at ω_1 and ω_2 are
given by

$$I_o^2\sin^2(\delta)J_o^2(m)J_1^2(m) \qquad \text{fundamental; } \omega_1,\omega_2 \qquad\qquad (3.1)$$

$$I_o^2\cos^2(\delta)J_o^2(m)J_2^2(m) \qquad \text{2nd harmonic; } 2\omega_1,2\omega_2 \qquad\qquad (3.2)$$

$$I_o^2\cos^2(\delta)J_1^4(m) \qquad \text{2nd-order intermodulation; } \omega_1 \pm \omega_2 \qquad\qquad (3.3)$$

$$I_o^2\sin^2(\delta)J_1^2(m)J_2^2(m) \qquad \text{3rd-order intermodulation;} \qquad\qquad (3.4)$$
$$2\omega_1 \pm \omega_2, 2\omega_2 \pm \omega_1$$

where I_o is the optical power incident on the detector, δ is the modulator bias position, m is the
modulation index, and $J_n(m)$ is the Bessel function of the first kind of order n. The modulation
index is given by $m = (\pi/2)(V_d/V_\pi)$, where V_d is the instantaneous drive voltage at ω_1 and ω_2,

and V_π is the modulator half-wave voltage. For links that have bandwidths less than one octave, the SFDR is measured using the third-order intermodulation signals. The relative levels of the fundamental signal to the spur at the third-order intermodulation frequencies can be computed by taking the ratio of Eq. 3.4 to Eq. 3.1 given above. The ratio is constant for a specific modulation index m and is independent of modulator bias δ. However, if the link is designed for multioctave bandwidth operation, the second-order intermodulaton signals must be inspected. The second-order intermodulation signals, $\omega_1 \pm \omega_2$, are larger than the second-order harmonics. The ratio of the fundamental to the second-order intermodulation signals is a function of the modulator bias point. Figure 3-5 shows the relative levels of Eq. 3.1 to 3.4 as a function of phase bias error for a modulation index set to a value when the third-order products equal the noise floor of the system shown in figure 3-2. The maximum allowable bias error is then calculated based on the requirement that the SFDR not be degraded by the modulator biasing.
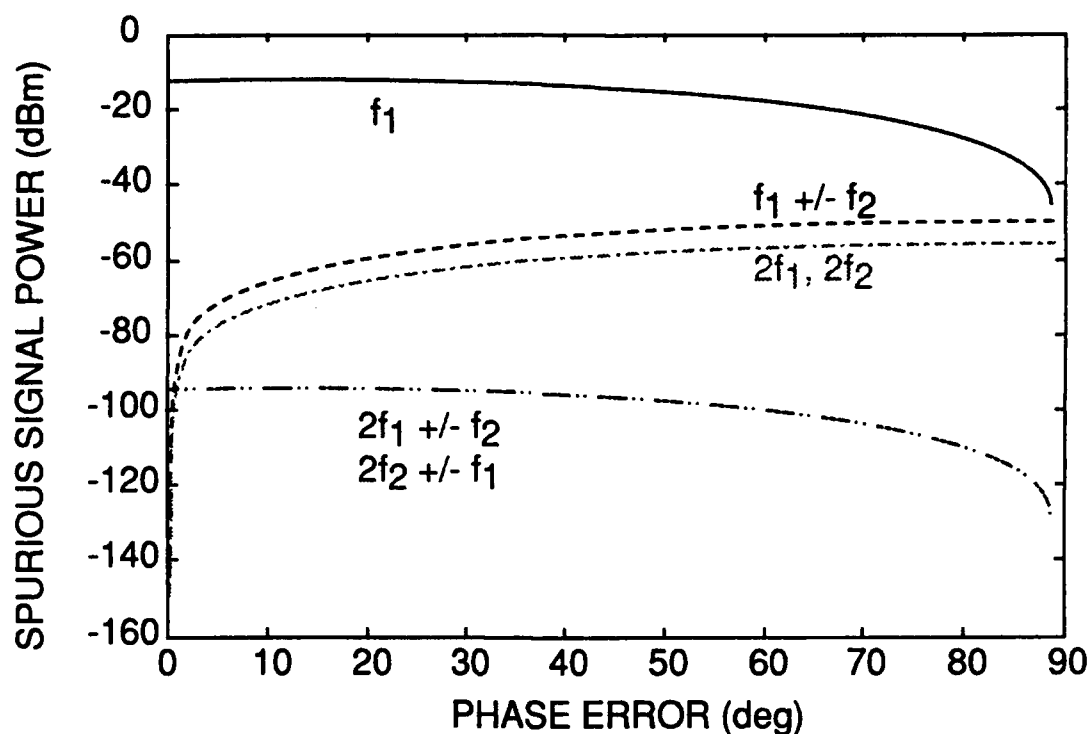
Figure 3-5. Fundamental and spurious signal levels as a function of phase bias error for the minimum detectable modulation index.

The receiver bandwidth is an important factor in finding the sensitivity of the phase bias error of the MZ modulators. For instance, if the receiver bandwidth is reduced, the system noise floor is reduced and the spurious signals become more prevalent. In figure 3-5, the noise floor would move lower and the second and third-order products would appear at a lower input drive level (smaller modulation index). Therefore, the output absolute noise floor level affects the measurable spurious signal levels allowed, which determines the required modulator bias point accuracy.

33

The 30- to 500-MHz fiber optic link used for this measurement has an RF insertion loss of 11 dB, an NF of 20 dB, and an SFDR of 109 dB/Hz$^{2/3}$. The 2- to 18-GHz link has an RF insertion loss of 27 dB, an NF of 35 dB, and a 108-dB/Hz$^{2/3}$ SFDR for optimum modulator biasing. The effect of a 1-degree phase bias error on the SFDR for the 30- to 500-MHz link is shown in figure 3-6. The plot assumes a 30-kHz receiver bandwidth, which is appropriate for channelized receiver or ultrawideband applications. It is already apparent that the SFDR of this link is being severely limited by the harmonic levels. A similiar result is found for the 2- to 18-GHz link. To emphasize this point further, a plot of the phase error tolerance (the second-order intermodulation signal level equals the third-order intermodulation level) versus receiver bandwidth for the lower frequency link is shown in figure 3-7. This curve suggests that for multioctave channelized receiver applications, a modulator phase bias error of 0.5 degree or less is required. This level of modulator phase bias accuracy is extremely difficult to attain using passive modulator biasing techniques.
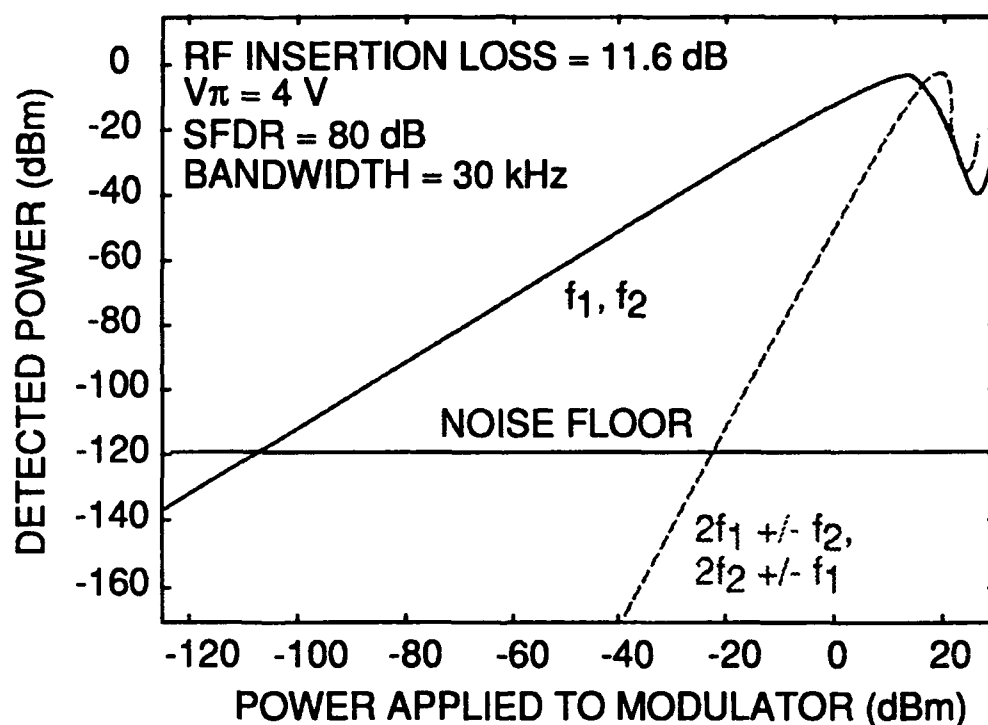
Figure 3-6. Effect of 1-degree modulator phase bias error on the 30–500-MHz fiber optic link.

A plot of the modulator phase bias drift versus temperature for the modulators used in the 30- to 500-MHz and 2- to 18-GHz links is shown in figure 3-8. Both the proton-exchanged and the ion-diffused modulators show unacceptable bias point drifts over the 20°C to 100°C temperature range. Even the most stable modulator designs will have difficulty maintaining the bias point to the degree required. Hence, active control of the modulator bias point is imperative for high-performance multioctave link applications. Computer-controlled bias point stabilization results between 20°C and 100°C are shown in figure 3-9 for both links investigated. A second harmonic suppression as high as 20 dB was obtained for both links, which translates into increased SFDR. Using the computer control, the bias points for both links were maintained to
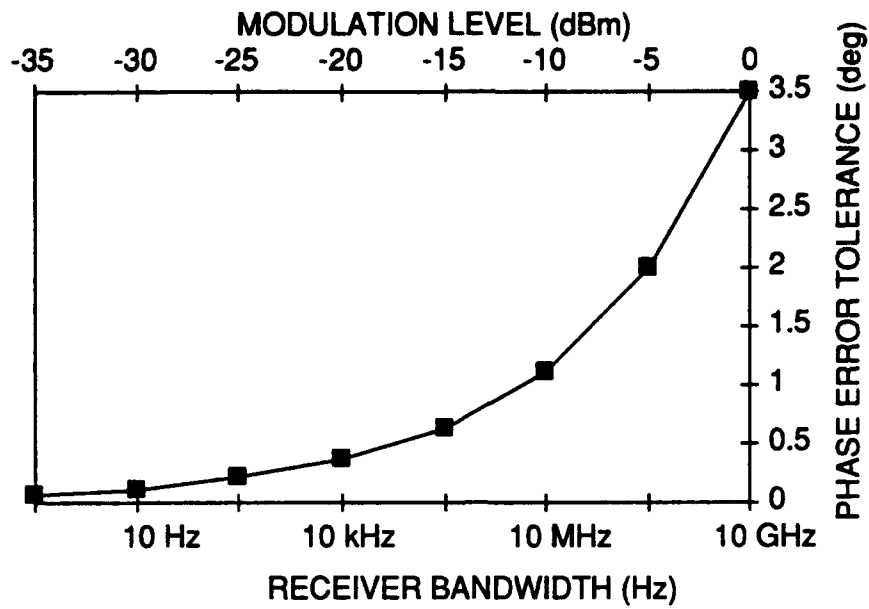
Figure 3-7. Modulator phase bias tolerance as a function of receiver bandwidth for the 500-MHz fiber optic link.
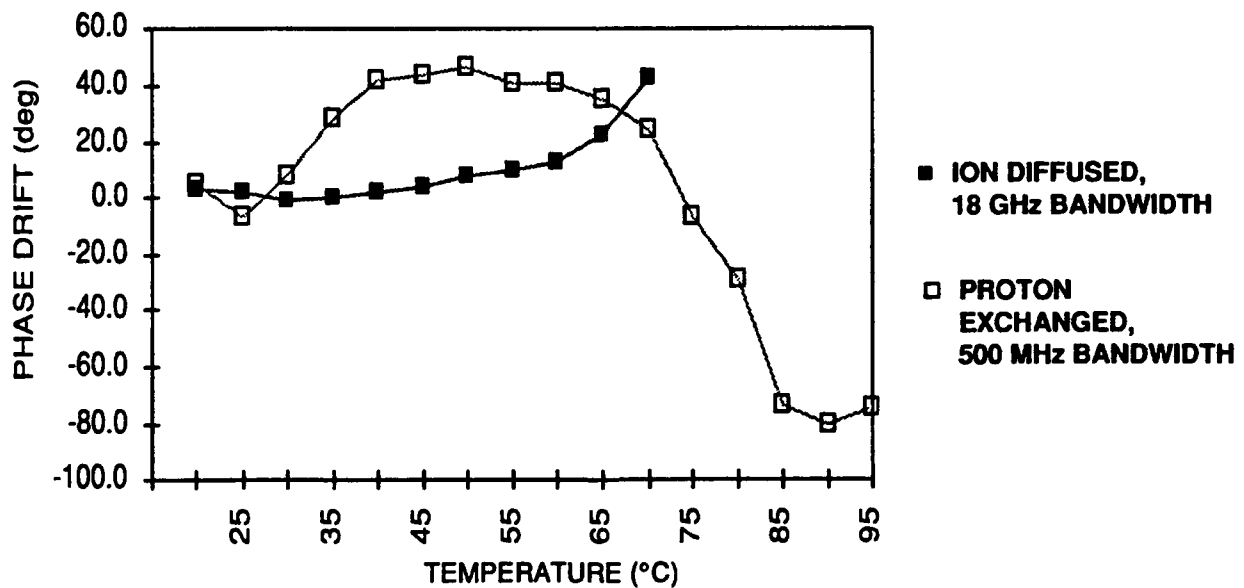
Figure 3-8. Modulator phase bias drift as a function of temperature for proton-exchanged and titanium-indiffused lithium niobate optical modulators.
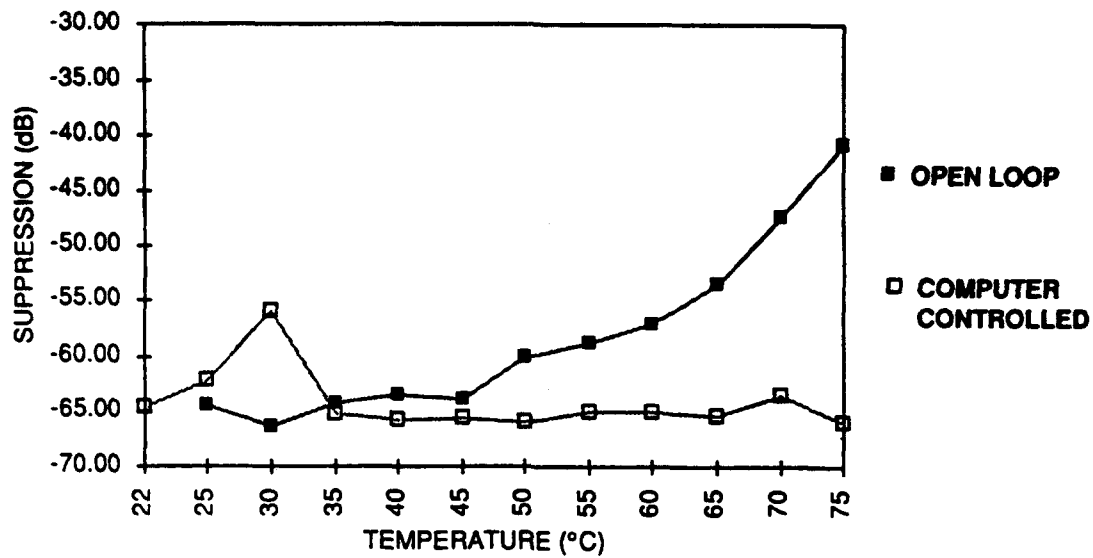
(a) Ion-diffused modulator.
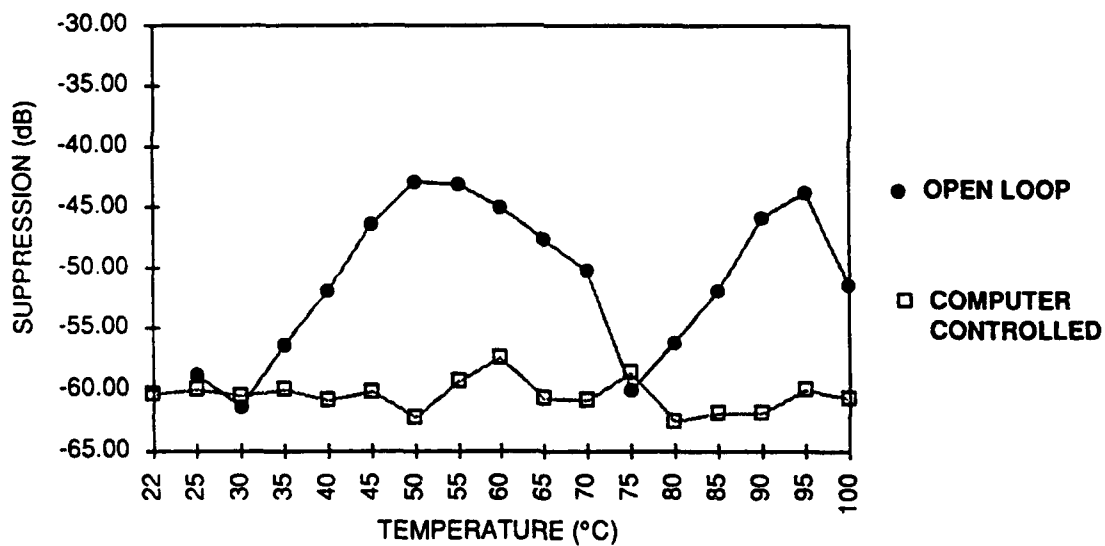
(b) Proton-exchanged modulator.

Figure 3-9. Computer-controlled modulator phase bias stabilization results as a function of temperature for both low- and high-frequency fiber optic links.

within 1 degree, which was limited by the time consant of the feedback circuitry. Better bias point control should be possible using this technique along with optimized feedback algorithms. This should allow multioctave fiber optic links employing MZ optical modulators to approach third-order intermodulation-limited SFDRs. This system improvement should enable EO EME monitoring systems to operate over the wide temperature ranges expected in the shipboard environment.

3.1.3 Remote Optical Polarization Control of EM Field Sensor

The performance of externally modulated remote fiber optic links similiar to that shown in figure 2-1 is subject to polarization fading if the proper polarization is not presented to the modulator. The use of PMF is a common method for overcoming this problem, and due to its relative maturity, it is the method to be used in the FY 94 shipboard demonstration for this project. However, PMF is difficult to use, is prone to damage, and can add significant cost to the system. Alternatively, two techniques have been investigated which eliminate the need for PMF in remote link applications. One technique uses a quasidepolarized optical source by combining two orthogonally polarized light beams in a single-mode optical fiber.[22] In this case, the modulator ideally accepts the same amount of optical power irrespective of fiber polarization effects. With this technique, it is critical that the power of the two lasers is identical, that the polarizations are truly orthogonal, and that the laser beat frequency is pushed beyond the frequency range of interest. These are not trivial experimental tasks. Another technique relies on active polarization control with standard SMF to compensate for polarization drifts in the fiber between the source and the controller and in the fiber leading to the sensor. With this technique, much lower cost fiber can be used, which would permit simple field repairs and the use of optical sources that are pigtailed with standard fiber rather than PMF. This polarization-control technique has been investigated for its application to the shipboard EME monitoring system.

Several polarization-controlling systems have been developed based on either lithium niobate, rotating waveplates, fiber squeezers, or fiber cranks.[23] However, these systems are either expensive, have high insertion loss, or mechanically fatigue the fiber, which can some-times result in breakage. Liquid crystals can be used for polarization control and do not suffer from these limitations.[24,25] While response times of liquid crystals were once considered to be too slow for some applications,[26] methods are being investigated to improve the response time until it is practical for virtually all communication and sensor applications. This Section describes work demonstrating the use of a liquid-crystal polarization controller in a remote fiber optic link configuration similiar to that used in the EO EME monitoring system.

The experimental setup is shown in figure 3-10. The source is a 10-mW Nd:YAG solid-state laser emitting at 1.32 μm, followed by a quarter-wave plate and a half-wave plate. The wave-plates are mounted on stages which can be rotated to produce any desired polarization and effectively simulate the effect of birefringence in standard SMF between the source and the polarization controller. The liquid-crystal polarization controller consists of three liquid-crystal cells. This is the minimum number of retarders required to transform any polarization to any other polarization. A coupling lens is used to launch the optical signal into a 2-km length of SMF. The SMF is connected to the PMF pigtail of a titanium-indiffused lithium niobate MZ modulator using standard FC connectors. The output of the modulator is detected by means of a high-speed InGaAs p-i-n photodiode. The RF insertion loss is measured with an HP8510B network analyzer in the 2- to 18-GHz range.
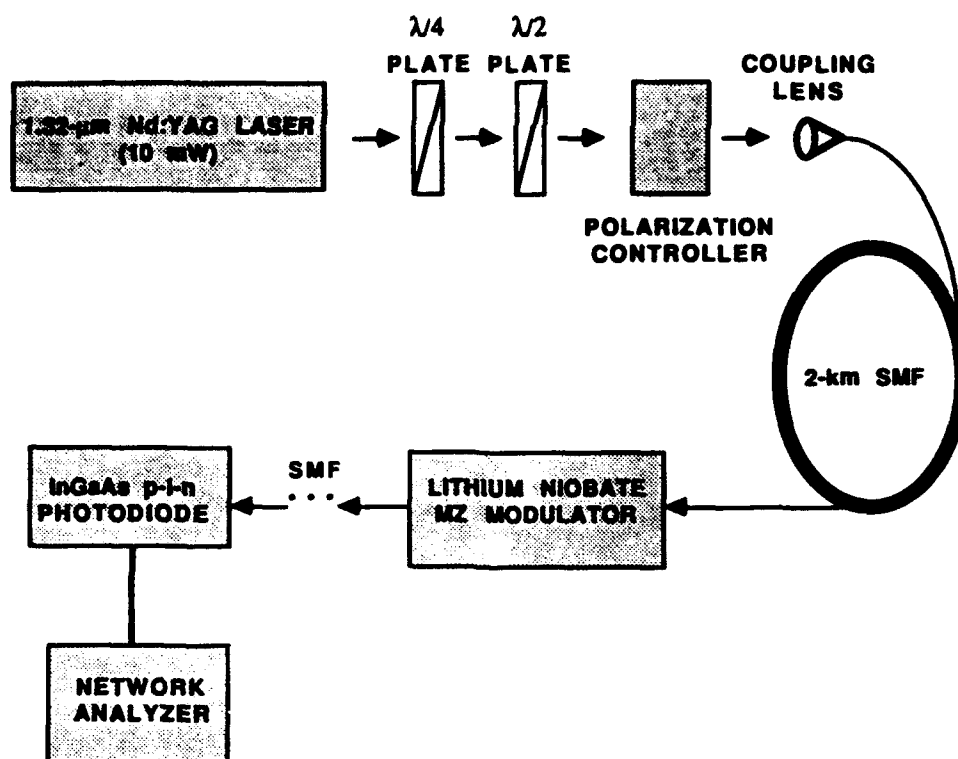
Figure 3-10. Remote polarization control setup using liquid-crystal phase
retarders.

To determine a baseline performance and to illustrate the effects of polarization fading, the
first two measurements of RF insertion loss were made without the polarization controller.
Figure 3-11 shows the RF insertion loss after the quarter-wave plate and the half-wave plate are
set for maximum output signal and maximum photodiode current. The RF insertion loss at
2 GHz is –44 dB and the photodiode current is 0.78 mA. Figure 3-12 shows the RF insertion
loss after the waveplates are set for minimum RF signal, which is below the noise floor of the
system at –84 dB. These measurements indicate the potential RF signal level fading if standard
SMF is used without any form of polarization control.

Next, the polarization controller was inserted into the system and the RF insertion loss
measurements were repeated for several input polarizations to the polarization controller. The
waveplates were rotated to produce right- and left-handed circular polarizations and linear
polarizations with tilts of 0, ± 45, and ± 90 degrees. In each case, the polarization controller
was adjusted to maximize the RF signal level. Figure 3-13 shows the RF insertion loss of the
link for one of the measurements: a –52.5 dB insertion loss at 2 GHz and a photodiode current of
0.3 mA. All measurements of RF insertion loss and photodiode current repeated within a range
of ± 0.25 dB and 0.005 mA, respectively, which is within experimental error. The 8.5-dB
excess RF insertion loss is due to a 4.25-dB optical loss through the the polarization controller.
The optical loss can be reduced to 0.45 dB by using cells optimized for use in the near-infrared.

Hence, polarization control for remote sensing applications using liquid crystals has been
successfully demonstrated in a fiber optic link. Polarization control can compensate for
polarization changes in fiber leading up to the polarization controller as well as those between
the controller and the remote sensor, enabling the use of optical sources pigtailed with standard

38

>S21   log MAG
REF -50.0 dB
2   3.0 dB/
▽ -0.0059 dB

C
A   IF AVERAGING FACTOR
S   1.0 k

START   2.000000000 GHz
STOP   18.000000000 GHz
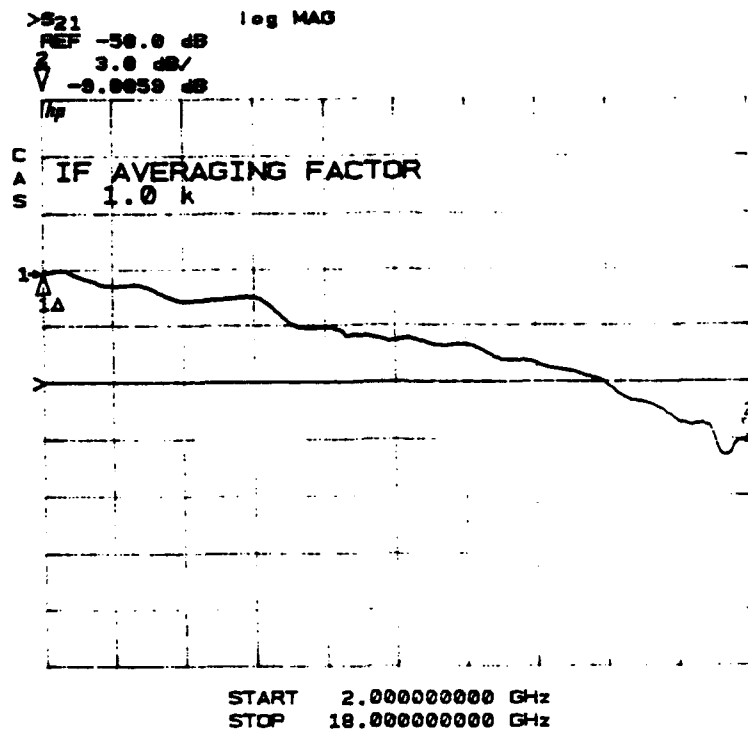
Figure 3-11. Fiber optic link RF insertion loss with optimum polarization alignment.

>S21   log MAG
REF -80.0 dB
2   3.0 dB/
▽   4.707 dB

C
A   REFERENCE VALUE
S   -80.0 dB

START   2.000000000 GHz
STOP   18.000000000 GHz
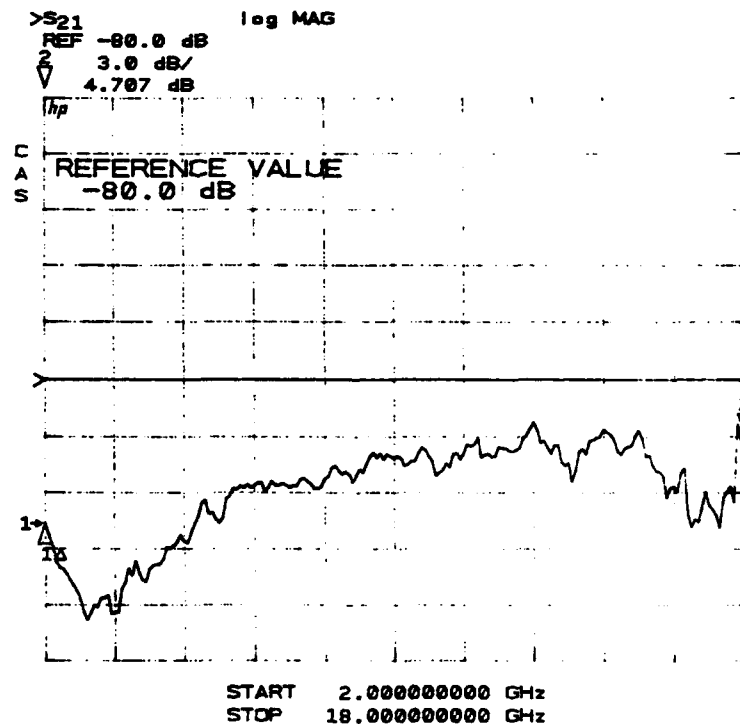
Figure 3-12. Fiber optic link RF insertion loss with worst-case polarization alignment.

39

>S21   log MAG
REF -50.0 dB
3.0 dB/
-9.1191 dB

```
  hp
C
A
S
```

START   2.000000000 GHz
STOP   18.000000000 GHz
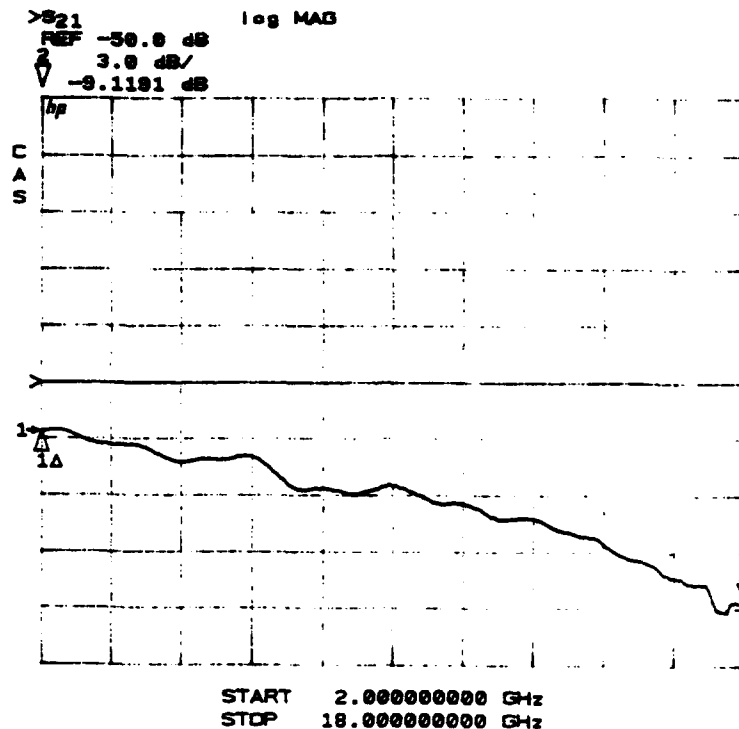
Figure 3-13. Fiber optic link RF insertion loss with
optimum liquid-crystal phase-retarder alignment.

SMF rather than PMF. Manual adjustments provided simple quick maximization of the signal, but a feedback control loop could be added to automate the process. The 8.5-dB excess RF insertion loss due to the optical insertion loss of the polarization controller at 1.3 µm is incurred because the liquid-crystal cells were designed for visible light. Cells with enhanced transmission have been made with an optical insertion loss of < 0.15 dB at 1.3 and 1.55 µm. Cells such as these are being prototyped into a fiber-pigtailed system with an optical insertion loss expected to be < 1.5 dB. This insertion loss is comparable to that which is incurred using PMF, especially if multiple connectors are used. The size of the fiber-pigtailed liquid-crystal controller will be a cylinder approximately 2 inches long and 1/2 inch in diameter. This system can be useful for reducing the cost of an EO EME monitoring system without affecting size or weight.

3.2 IMPROVEMENTS TO WIDEBAND RF PROBE

The EM field sensing element is an important component of the shipboard EME monitoring system. Efficient wideband probes which can be packaged into small portable units are desired. For frequencies above 500 MHz, commercially available spiral antennas are the best choice. Compact spiral antennas are available with responses from 0.5 to 50 GHz. Two spiral antennas can cover this entire range. The gain as a function of frequency of a 0.5- to 18-GHz two-arm circularly polarized omnidirectional spiral antenna (Watkins-Johnson Model WJ-48920) is shown in figure 3-14. A gain of > 0 dBi is obtained for frequencies > 500 MHz. Below 500 MHz, the response of this antenna drops off dramatically, but is useable to 300 MHz (-20-dBi gain). This is one of the antennas to be used in the FY 94 shipboard demonstration. Spiral antennas with > -2-dBi gain from 18 to 50 GHz have been obtained (AEL Model ASM-1601)

40

and can be diplexed with the low-frequency antenna signals by using conventional techniques. Below 500 MHz, the situation is quite different, for there are no commercially available compact antennas that currently meet the requirements for shipboard EO EME monitoring. A number of developmental efforts are under way to solve this low-frequency antenna problem. These antenna structures will now be discussed.
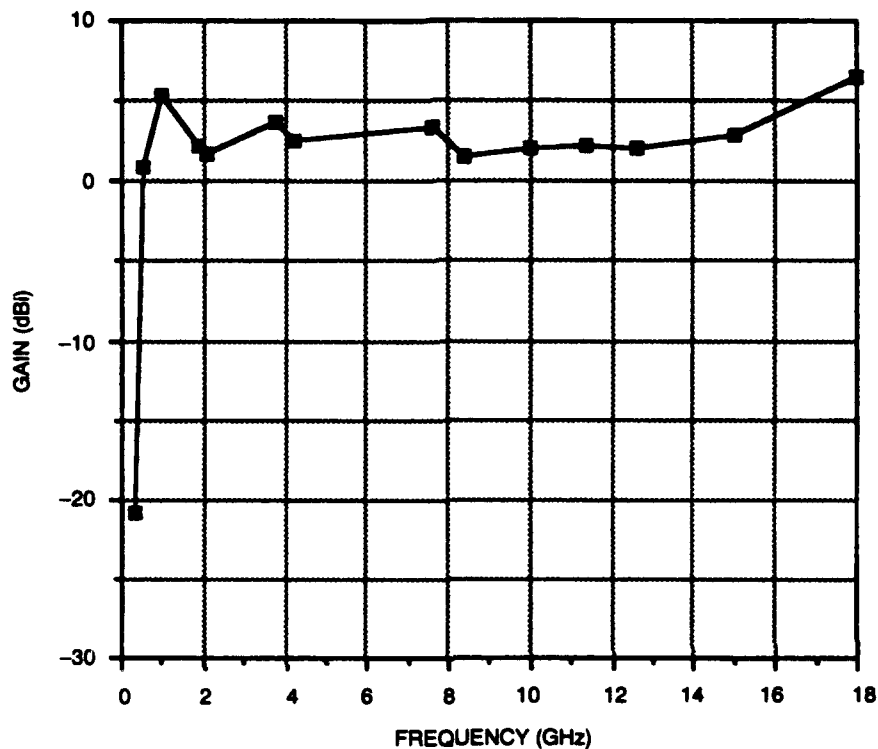
Figure 3-14. Gain versus frequency for the Watkins–Johnson two-arm spiral antenna.

3.2.1 Electrically Short Dipole or Monopole Antenna

The use of an electrically short dipole antenna or a monopole antenna with corresponding ground plane is the simplest way to achieve a limited response at low frequencies. These antennas are easy to produce, have a broad beamwidth, and can be modeled rather easily. With an antenna length less than half the wavelength of the highest frequency of interest, the antenna efficiency decreases monotonically with decreasing frequency and can be easily calibrated. The high frequency ($f > f_r$, where f_r is the antenna resonant frequency) response oscillations can be damped by resistively loading the dipole or monopole antenna, which can extend the useful bandwidth of the antenna. The drawback of the electrically short antenna is that it sacrifices a considerable amount of radiation efficiency, especially at the lowest frequencies. However, due to the rather high actual shipboard field strength levels, this approach may be feasible.

Simulations have been performed on bare and resistively loaded dipole and monopole antennas to estimate the gain down into the HF band. Figure 3-15 shows the simulated antenna output power as a function of frequency delivered into a 50-Ω load for a bare 15-cm dipole and a resistively loaded 15-cm dipole. An incident RMS electric field strength of 0.7 V/m is

assumed for these curves. For frequencies up to 500 MHz, there is no need for the resistive loading. At 2 MHz, an antenna output power of -80 dBm is obtained. The NF of the EO EME monitoring system is approximately 40 dB, which implies an input sensitivity of -135 dBm in a 1-Hz bandwidth. A more realistic receiver bandwidth is approximately 30 kHz, which implies a sensitivity of approximately -90-dBm, which is well below the 2-MHz antenna signal. Given a system NF of 40 dB, the minimum detectable RMS electric field level is plotted as a function of frequency in figure 3-16 for a 15-cm bare dipole antenna and a resistively loaded 15-cm dipole. This result implies that a short dipole antenna or equivalent monopole antenna with corresponding ground plane can satisfy the 2- to 500-MHz shipboard EME monitoring requirements; an experimental verification of this is in progress.

3.2.2 Enlarged Spiral Antenna

There are a number of approaches to increasing the efficiency of compact antennas which are useable from 2 to 500 MHz. One approach is to apply wideband spiral antenna techniques and simply increase the aperture size. This basic approach is being pursued by Wang-Tripp in a Navy-sponsored and NRaD administered R&D effort. It is anticipated that 30- to 500-MHz frequency coverage with > 0-dBi useable gain across this band can be achieved by utilizing a 24-inch-diameter spiral-mode microstrip antenna with modified electrical feed arrangement. Extended operation down into the HF band will be investigated. The proposed antenna will be small, lightweight, and possess a broad beamwidth, characteristics which are required for this application. A prototype antenna should be available for testing in this program in FY 94.

3.2.3 Sectorialized Monopole Antenna

A 30- to 500-MHz passive monopole antenna is being developed by Dorne & Margolin, Inc. as part of a Navy-sponsored and NRaD administered R&D program. The approach taken is based on combining the self-complementary antenna principle with a sectorialized antenna structure. The monopole antenna provides omnidirectional coverage as long as its length is less than one-half the radiating wavelength. For multioctave applications, the standard monopole antenna either possesses low gain at the low frequencies or undesired lobing at the higher frequencies. To overcome this, a sectorialized antenna which satisfies the omnidirectional requirement across the band is proposed. A minimum-size omnidirectional monopole antenna which possesses > 0 dBi across the frequency band is to be developed. Extended operation down into the HF band will be investigated. Prototype antenna structures will be available in FY 94 for use in this EM field monitoring task.

3.2.4 High-Dielectric Spiral Antenna

Another way to improve the low-frequency response of compact antennas is to fabricate spiral antennas on high-dielectric substrates in an attempt to effectively increase the aperture/wavelength ratio. When a high-relative-dielectric substrate material, ε_s is employed, the radiating wavelength in the dielectric material is decreased by $\lambda/(\varepsilon_s)^{1/2}$. The larger the dielectric constant, the shorter the wavelength, and hence, the larger the antenna gain. However, this increased gain is compensated for to some extent by the increased reflection coefficent of the antenna structure. The reflection coefficient should scale like $(\varepsilon_s^{1/2} - \varepsilon_o^{1/2})/(\varepsilon_s^{1/2} + \varepsilon_o^{1/2})$, where ε_o is the-free space relative-dielectric constant. This tradeoff has been experimentally investigated.
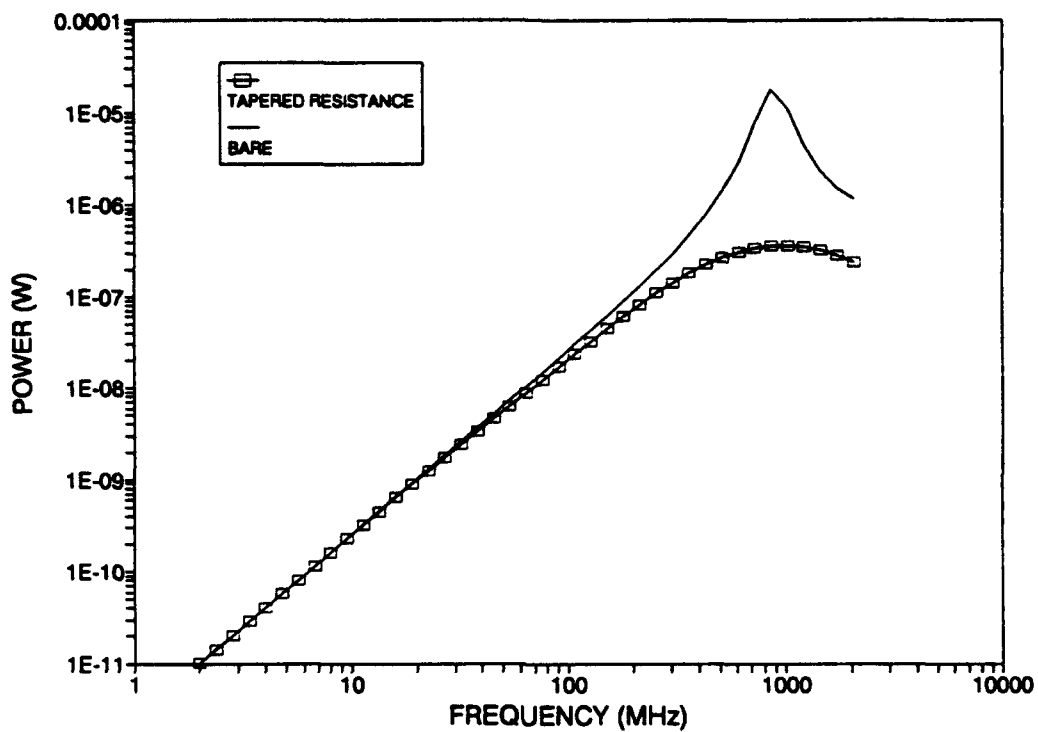
Figure 3-15. Antenna output power into 50-Ω load versus frequency for a bare and resistively loaded 15-cm dipole with 0.7-V/m RMS electric field excitation.
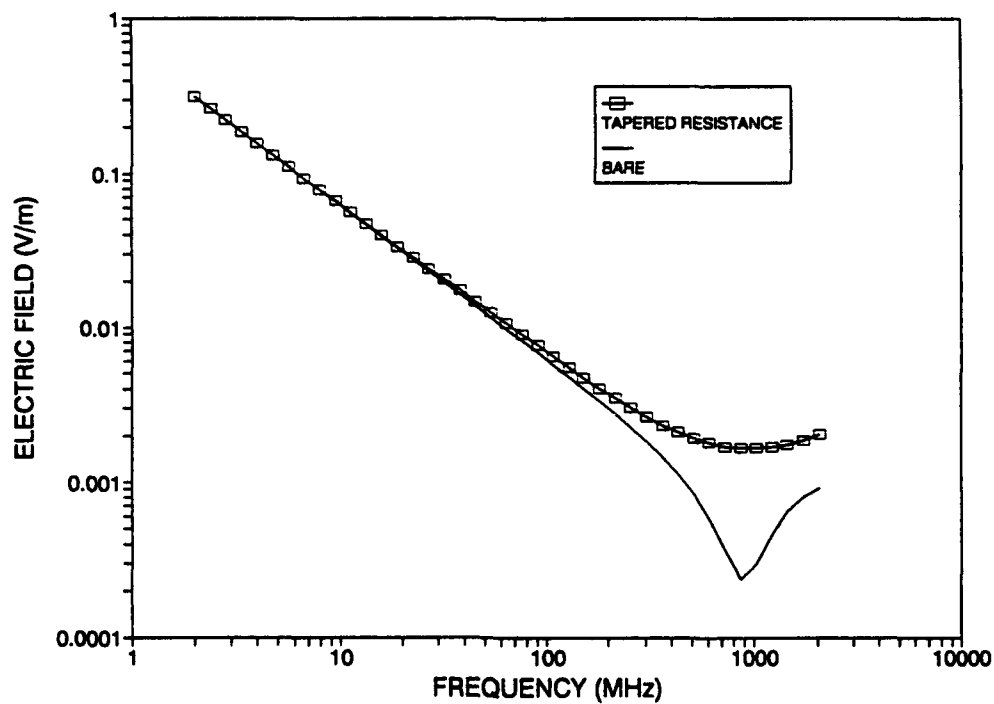
Figure 3-16. Minimum detectable RMS electric field level versus frequency for a bare dipole, assuming a 40-dB system NF and a 30-kHz receiver bandwidth.

A number of multiturn spiral antennas have been fabricated on a high-dielectric substrate (barium-doped titanium dioxide, ε_{hd} = 80) and compared with identical antennas fabricated with conventional Duroid substrates (ε_d = 2.2 or ε_d = 10). The spirals were designed to follow an exponential radial dependence given by

$$r(\Theta) = A \exp(B \ \Theta) \tag{3.5}$$

where A and B are parameters that have been varied. The return loss (S_{11}) versus frequency for 3-inch, 1.5-turn spiral antennas fabricated on each substrate material is shown in figure 3-17. The antenna fabricated on the high-dielectric material clearly cuts in at a lower frequency, as expected. The return loss for 6-inch, 1.5-turn spirals fabricated on the two substrates is shown in figure 3-18. Again, the cut-in frequency is lower (400 MHz versus 600 MHz) for the spiral antenna fabricated on the high-dielectric material. The number of turns has an effect on the antenna characteristics as well. The return loss for 6-inch, ε_d = 2.2 spiral antennas with 1, 1.5, and 2 turns is shown in Figure 3-19. The antenna with 2 turns has the lowest cut-in frequency. However, a higher absolute reflection coefficient, which must be accounted for, is obtained for the 2-turn spiral. An impedance transformer is one method of overcoming the added reflection loss. The best results have been obtained on a 12-inch, 6-turn spiral antenna. The return loss versus frequency for this antenna is shown in figure 3-20, where a 250-MHz cut-in frequency is obtained. This demonstrates the concept of using high-dielectric substrate material for enhancing the low-frequency antenna response. Optimization of the antenna structure is continuing, and antenna patterns will be obtained on optimized structures.

Each of the four techniques discussed has its advantages for producing an efficient, broadband, compact antenna which is useable down into the HF band. At this point, laboratory testing is continuing to ultimately decide which low frequency antenna bests suits this application. Above 300 MHz, the two-arm spiral antenna with useable gain out to 18 GHz will be used in the shipboard demonstration. The plans for the FY 94 shipboard demonstration will now be discussed.
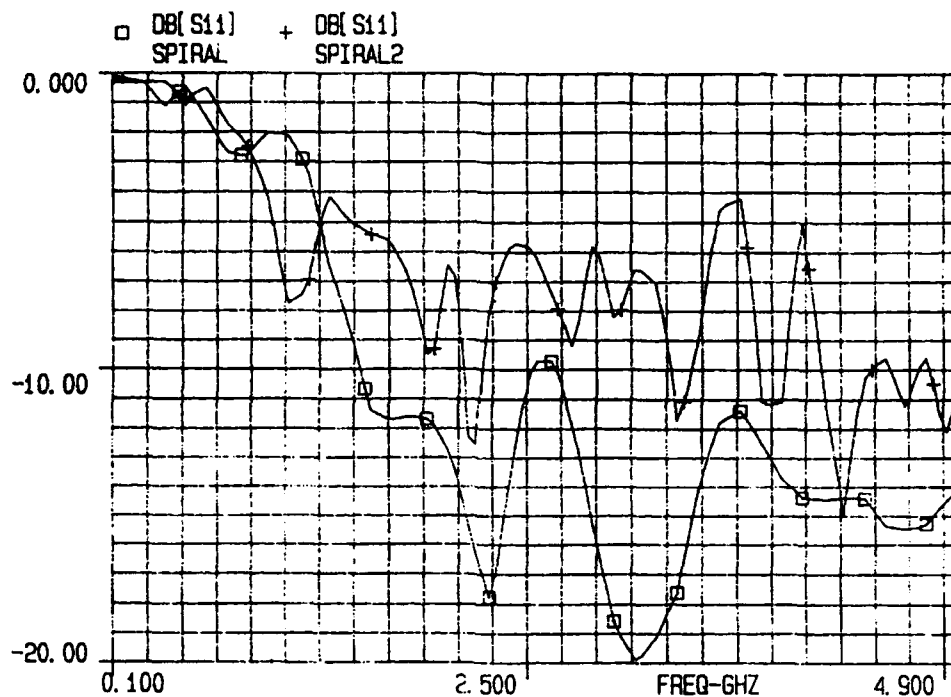
Figure 3-17. Return loss (S_{11}) versus frequency for 3-inch, 1.5-turn spiral antennas fabricated on relative dielectric constant 2.2 (squares) and 80 (crosses) substrate material.
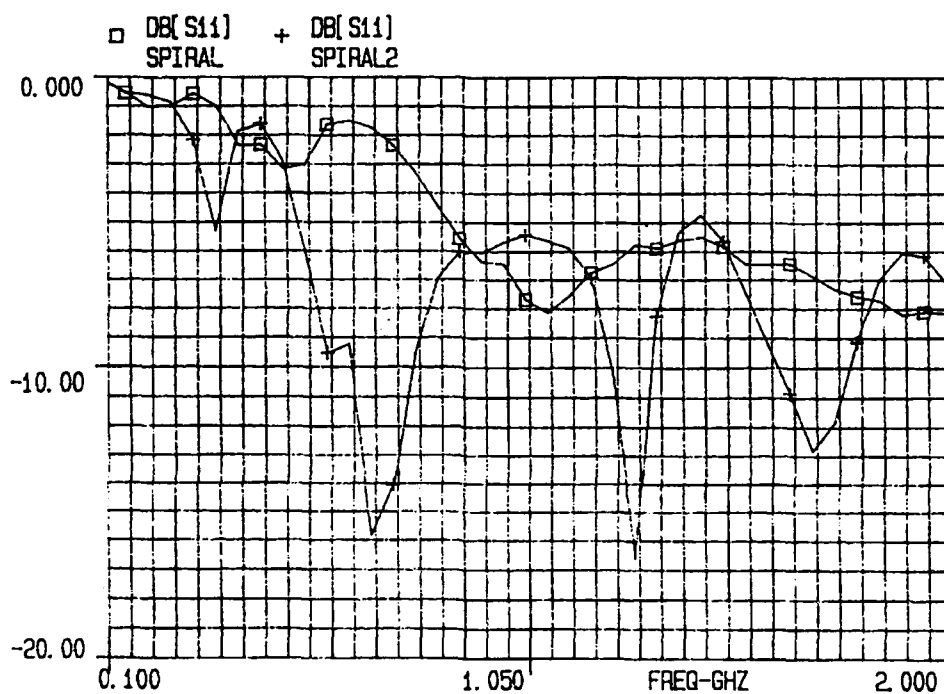
Figure 3-18. Return loss (S_{11}) versus frequency for 6-inch, 1.5-turn spiral antennas fabricated on relative dielectric constant 2.2 (squares) and 80 (crosses) substrate material.

Figure 3-19. Electrical return loss (S_{11}) for 6-inch spiral antennas on 2.2 dielectric constant substrates with 1 (crosses), 1.5 (squares), and 2 (diamonds) turns.

Figure 3-20. Electrical return loss (S_{11}) versus frequency for a 12-inch, 6-turn spiral antenna on 2.2 dielectric constant substrate.

46

4.0 SHIPBOARD DEMONSTRATION TEST PLAN

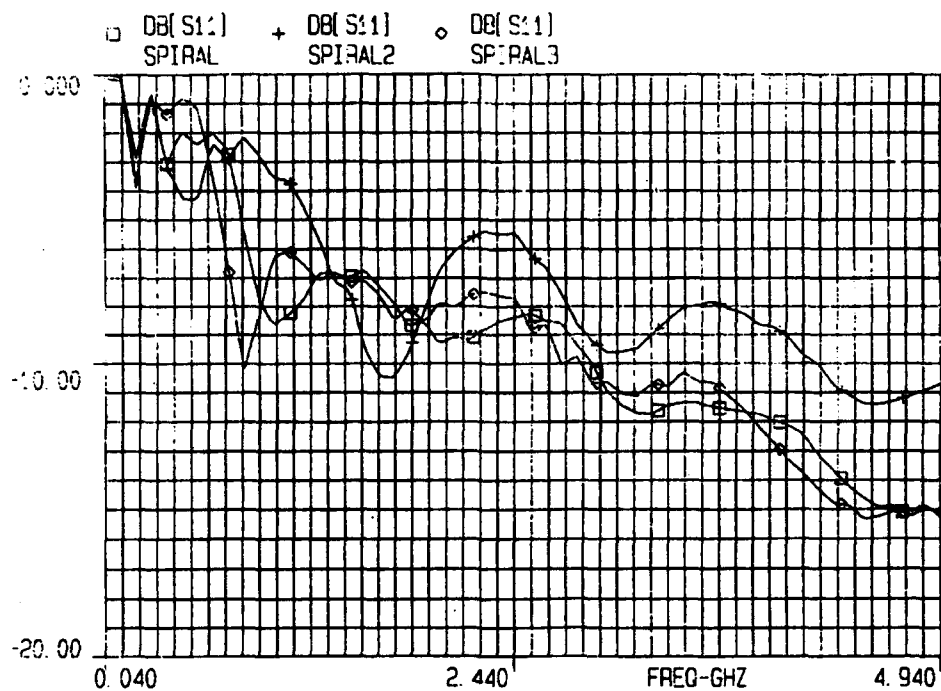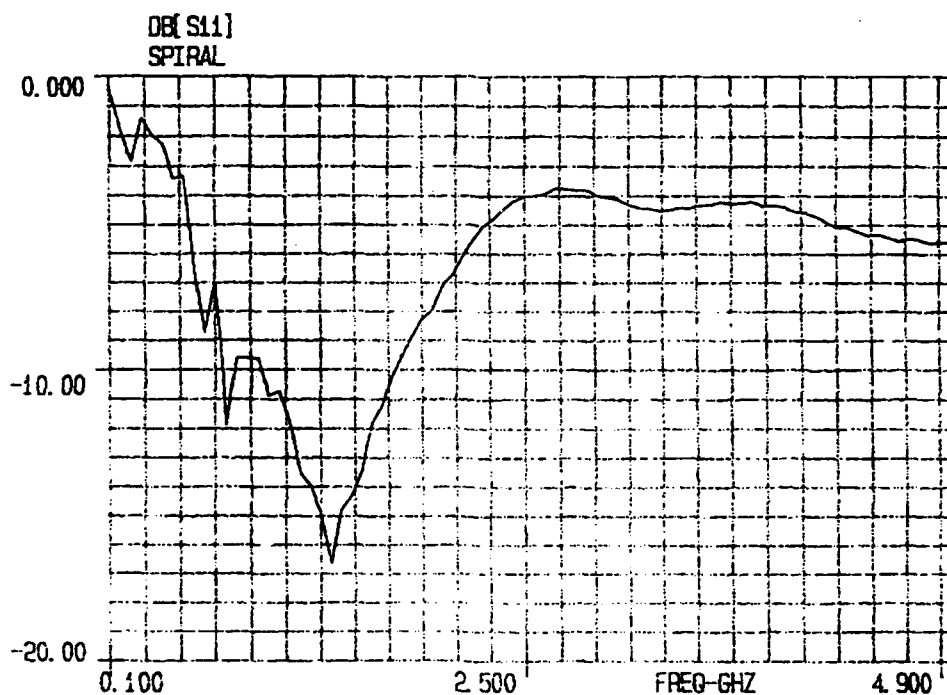In FY 94, the technology developed in this R&D effort will be shipboard-tested. The purpose of this shipboard demonstration is to qualify the technology under development and provide ship operators with an example of the enhanced capabilities it can bring. The plan is to temporarily mount the prototype photonic sensor assembly at various topside positions while controlled shipboard emissions are recorded. Details that need to be addressed include ship class, measurement sites, test and evaluation procedures, and documentation plans. These issues will now be discussed.

4.1 SHIP CLASS SELECTION

A number of naval surface ships have been considered for use in the shipboard testing of the EO EME monitoring system. Among these, the DDG-51 class and the LSD-41 class are considered the top candidates. Important factors influencing ship selection are the number of ships in the class, the EM configuration of the ship, and the availability in the San Diego area of the ship class for shipboard measurements. The existing ship class experimental EME database and the past experience of associated personnel in making shipboard measurements also weighed heavily in ship selection. With these factors taken into consideration, the LSD-41 class surface ship was selected for this task.

The LSD-41 is a dock landing ship that is 609 feet long, 84 feet wide, and 20.5 feet deep. It possesses a good complement of communication and surveillance capabilities, which makes it a good choice for testing the EME monitoring system. Within the LSD-41 class, the LSD-40, LSD-42, LSD-45, and LSD-47 have recent EMI certifications, which make them leading candidates for testing. This certification ensures properly functioning EM equipment, which is required if there are to be meaningful measurements. Specific LSD-41 class ship selection will depend on actual ship availability during FY 94 for shipboard measurements. Depending on scheduling, testing could occur on different LSD-41 class vessels . In such a case, some variation in topside EM and structural configurations is expected and will affect the actual EME at various shipboard sites. However, this is not a major issue for the purpose of these measurements. Data from the LSD-42 (USS *Germantown*) and LSD-47 (USS *Rushmore*) have been used as a baseline for expected EM field strengths for each transmitter at various shipboard sites.

The USS *Germantown* shipboard RF EM (radiated) system configuration has been determined from two sources: FY 90 DPMA SUPSHIP San Diego, CA, dated May 90, and COM-NAVSURFPAC Equipment List for Ship Class LSD-42/LSD-41, dated 11 Sep 89. Photographs of the USS *Germantown* with antenna sites numerically identified are shown in figures 4-1 to 4-6. Table 4.1 shows the antenna characteristics of each emitter on this vessel. In addition to the equipment description and location, RF transmitters are further described in regard to emitter level and modulation characteristics. Focusing only on the transmit antennas, there are three HF communication antennas, designated 2-1 through 2-3, and twelve VHF/UHF transceive communication antennas, designated 3-1 through 3-13. There are also an X-band navigation antenna, designated 4-1, eleven UHF surveillance antennas, designated 5-1 through 5-11, two broadband EW antennas, designated 6-1 and 6-2, and two weapons control antennas, designated 8-4 and 8-5. As many of these emitters as possible will be included in the testing of the EME monitoring system. All the emitters, except for the satellite communication (SATCOM) (3-9A and 3-9B), CIWS (8-4 and 8-5), EW (6-1 and 6-2), and HF antennas (3-1, 3-2, and 3-3), are located on the mast at various heights.

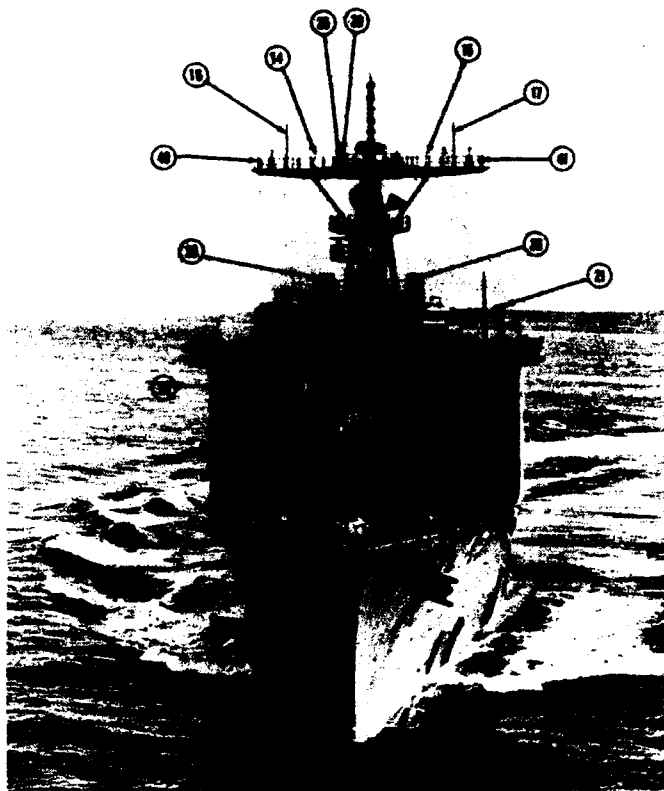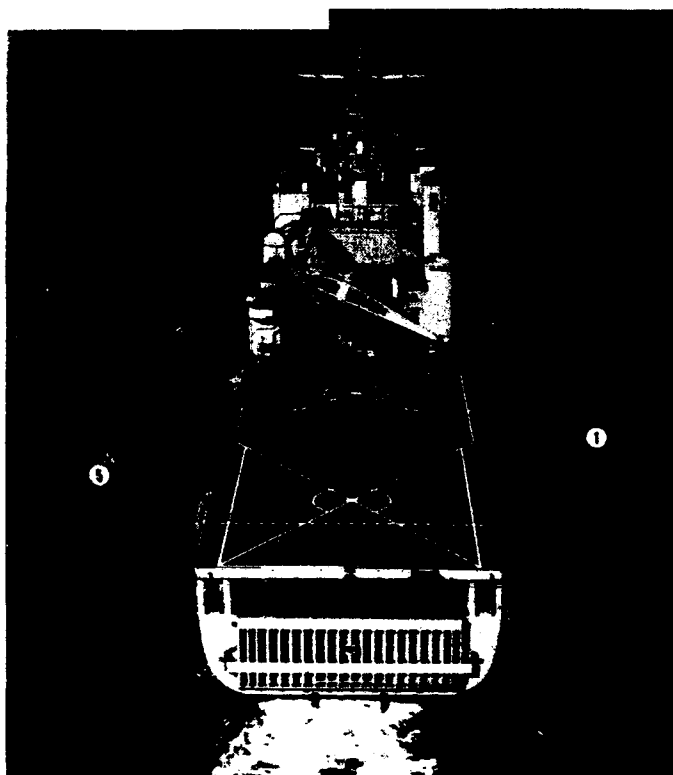Figure 4-1. Bow of USS *Germantown* (LSD-42).

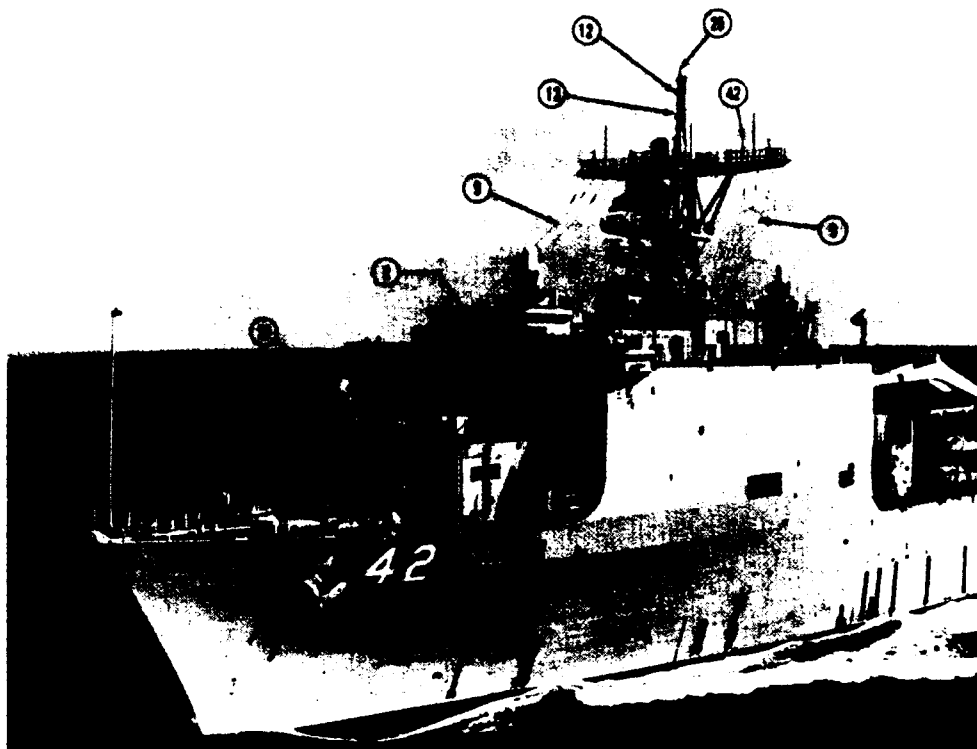Figure 4-2. Stern of USS *Germantown* (LSD-42).

Figure 4-3. Forty-five degrees from bow, port view of USS *Germantown* (LSD-42).
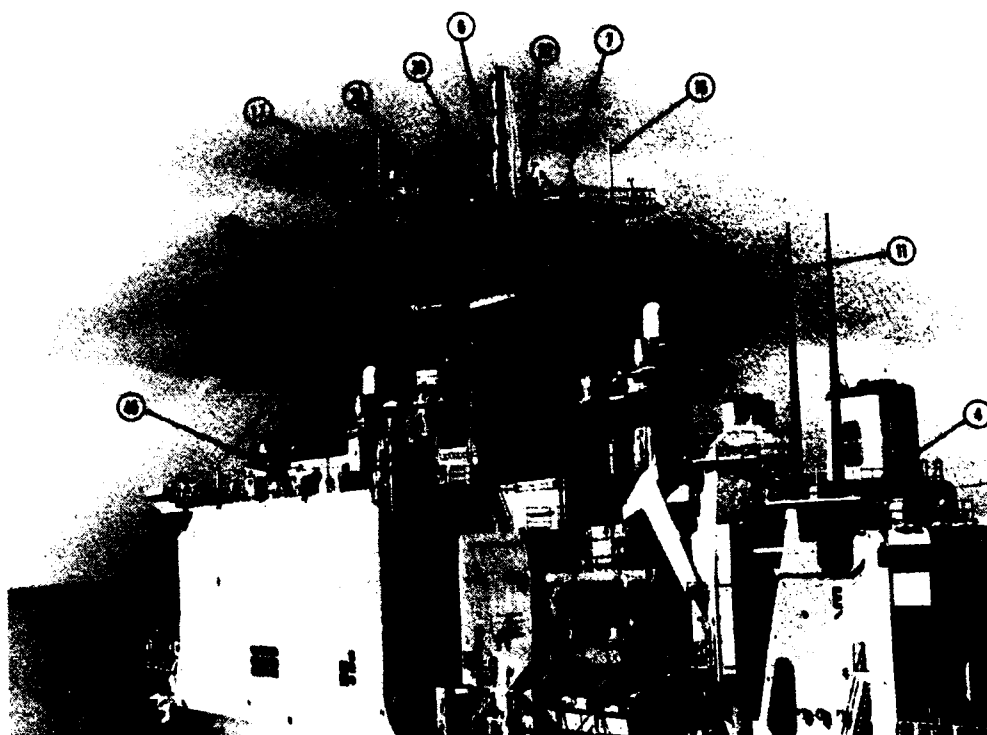

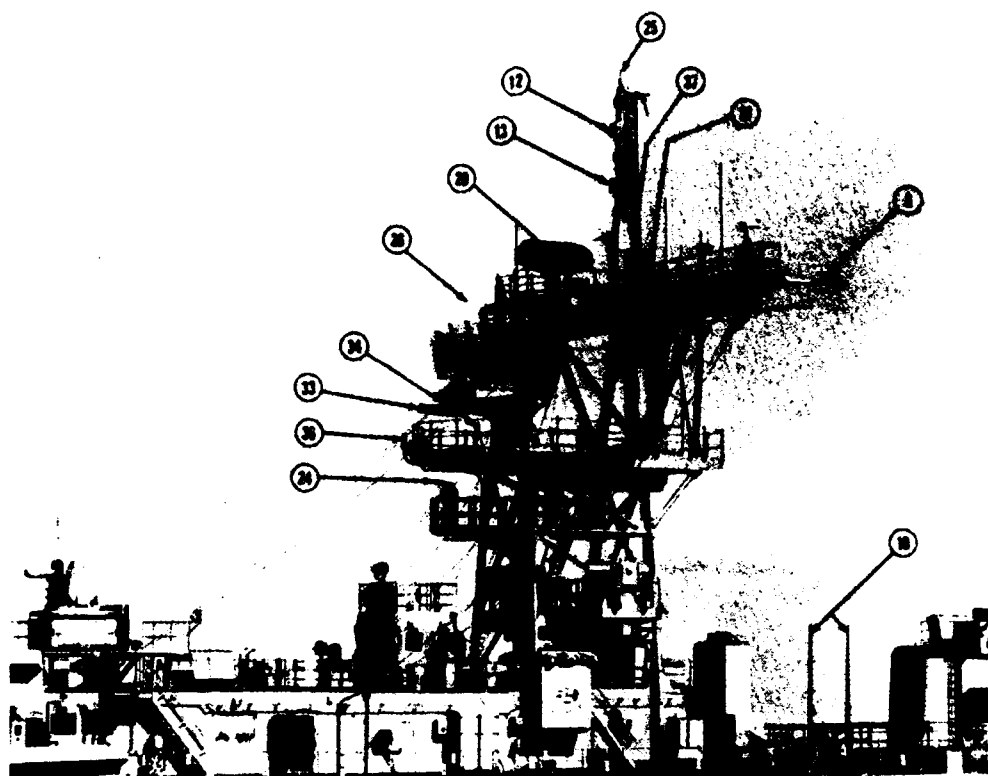Figure 4-4. Forty-five degrees from stern, port view of USS *Germantown* (LSD-42).

Figure 4-5. Broadside, port view of USS *Germantown* (LSD-42).

Figure 4-6. Broadside, starboard view of USS *Germantown* (LSD-42).

50

Table 4-1. LSD-41 class antenna characteristics.

Photo Ref No.	Ant No.	Antenna Nomenclature	Antenna Location	Antenna Termination	Ant Gain dB	System Nomenclature	Emitter Nomenclature	Freq Range MHz	Emitter Level μK	Emitter Type	Emitter BW
COMMUNICATIONS RECEIVE ONLY											
1	1-1	AS-3772A/U 35 FT TWIN WHIP	Stern Stbd	AN/SRA-40A NO. 1	N/A	AN/SRA-40A	Rec only	2-30	N/A	N/A	N/A
2	1-2A	AS-0815/SSR-1	Fwd/O/Bk	AN-0834/SSR-1	N/A	AN/SSR-1A	Rec only	240-315	N/A	N/A	N/A
3	1-2B	AS-0815/SSR-1		AN-0834/SSR-1	N/A	AN/SSR-1A	Rec only	240-315	N/A	N/A	N/A
4	1-2C	AS-0815/SSR-1	Mid/Ship/Port	AN-0834/SSR-1	N/A	AN/SSR-1A	Rec only	240-315	N/A	N/A	N/A
	1-2D	AS-0815/SSR-1		AN-0834/SSR-1	N/A	AN-SSR-1A	Rec only	240-315	N/A	N/A	N/A
5	1-3	AS-3771A/U OE-418/SRC 14 FT TWIN WHIP	Stern Port	AN/SRA-40A NO. 2	N/A	AN/SRA-40A	Rec only	4-30	N/A	N/A	N/A
6	1-6	AS-2807/SRR	N/Mid/Td	CONNECTOR	N/A	CRYPTO VAN	Rec only	30-1000	N/A	N/A	N/A
7	1-7	AS-2807/SRR	N/Stbd/Td	CONNECTOR	N/A	CRYPTO VAN	Rec only	30-1000	N/A	N/A	N/A
8	1-8	AT-0248/SR	N/Port/Td	AN/SRA-17C	N/A	OKCS	Rec only	0.014-0.60	N/A	N/A	N/A
COMMUNICATIONS HF/MF TRANSMIT & RECEIVE											
9	2-1	AS-4114/SRC OE-483/SRC TWIN FAN	N to B/Bk	AN/SRA-56 NO. 1 & 2	4	AN/SRA-56	AN/URT-230	2-6	1000	CW/AM/SSB	5 kHz
10	2-2	AS-3772A/U OE-415(V)2/SRC 35 FT TWIN WHIP	Aft/B/Bk/Port	AN/SRA-57 NO. 1 & 2	4	AN/SRA-57	AN/URT-230	4-12	1000	CW/AM/SSB	5 kHz
11	2-3	AS-3771A/U OE-482(V)1/SRC 14 FT TWIN WHIP	Mid/Ship/Port	AN/SRA-58	4	AN/SRA-58	AN/URT-230	10-30	1000	CW/AM/SSB	5 kHz
COMMUNICATIONS VHF/UHF/SHF/EHF TRANSCEIVE											
12	3-1	AS-1735/SRC	N/Top	OA-9123/SRC NO. 1	2	UHF LOS	AN/WSC-3(V)7	225-400	30	AM	25 kHz
13	3-2	AS-1735/SRC	N/Top	OA-9123/SRC NO. 2	2	UHF LOS	AN/WSC-3(V)7	225-400	100	FM/PSK	25 kHz
14	3-3	AS-2809/SRC	N/Stbd/Td	AN/URC-80(V)5	2	BRG-TO-BRG	AN/URC-80	156-162	25	FM	50 kHz
15	3-4	AS-2809/SRC	N/Port/Td	AN/GRC-211	2	VHF RADIO	AN/GRC-211	116-152	25	AM	25 kHz
16	3-5	AS-3226/URC	N/Stbd/Td	TD-1288(V)/GRC No. 1	2	VHF RADIO	AN/VRC-46A	30-76	50	FM	50 kHz
17	3-6	AS-3226/URC	N/Port/Td	TD-1288(V)/GRC No. 2	2	VHF RADIO	AN/VRC-46A	30-76	50	FM	50 kHz
18	3-7	AS-3226/URC	N/Mid/Td	TD-1288(V)/GRC No. 3	2	VHF RADIO	AN/VRC-49	30-76	50	FM	50 kHz
19	3-8	AS-3226/URC	Not Shown	TD-1288(V)/GRC No. 4	2	VHF RADIO	AN/VRC-49	30-76	50	FM	50 kHz
20	3-9A	AS-3018A/WSC-1(V)	Bow/Stbd	AN-6891A/WSC-1(V)	12	SATCOM	AN/WSC-3(V)3	240-318	800	FM/PSK	25 kHz
21	3-9B	AS-3318A/WSC-1(V) OE-82C/WSC-1(V)	Aft/B/Bk/Port	AN-6891A/WSC-1(V)	12	SATCOM	AN/WSC-3(V)3	240-318	800	FM/PSK	25 kHz
22	3-12	AS-3439/G	F/Port/Td		0	CRYPTO VAN	AN/URC-110	116-400	20	AM	25 kHz
23	3-13	AS-3439/G	N/Stbd/Td		0	CRYPTO VAN	AN/URC-110	116-400	20	AM	25 kHz
NAVIGATION											
24	4-1	AS-3194/SPS-64	N/Lower/Level	RT-1248/SPS-64	28	AN/SPS-64(V)9	AN/SPS-64(V)9	9375	20000	Pulse	60 MHz
25	4-2	GC-204/SRN-19(V)	N/Top	AN/SRN-19(V)2	N/A	SATNAV	Rec only	400	N/A	N/A	N/A
26	4-3	AS-2960/SRN-17	N/Stbd/Td	AN/SRN-17	N/A	OMEGA	Rec only	10-14 kHz	N/A	N/A	N/A
SURVEILLANCE											
27	5-1	AS-3263/SPS-49	N/Mid/Td	AN/SPS-49	29	AN/SPS-49(V)1	AN/SPS-49	850-942	280000	60 uSec	17 kHz
28	5-2	AS-0368/SPS-10	N/Mid/Td	AN/SPS-10	23	AN/SPS-10	AN/SPS-10	5400-5800	785000	0 25 uSec	4 MHz
29	5-3	AS-1778/UPX	N/Mid/Pd/Td	AN/UPX-25(V)4 NO. 1	2	IFF	AN/UPX-25	1030	2000	1 uSec	1 MHz
30	5-4	AS-1778/UPX	N/Stbd/Td	AN/UPX-25(V)2	2	IFF	AN/UPX-25	1030	2000	1 uSec	1 MHz
31	5-5	AS-1778/UPX	N/Mid/Td	AN/UPM-137A	2	IFF TEST	AN/UPM-137A	1090	10	1 uSec	1 MHz
32	5-6	AS-1778/UPX	N/Aft/Pd/Td	AN/UPX-25(V)4 NO. 2	2	IFF	AN/UPX-25	1030	2000	1 uSec	1 MHz
33	5-7	AS-2188/U	N/Mid/Level	AN/UPX-28	18	IFF (SPS-49)	AN/UPX-28	1030	2000	1 uSec	1 MHz
34	5-8	AS-3077/SP	N/Mid/Level	AN/SPS-49	N/A	SPS-49 CSLC	AN/SPS-49	850-942	N/A	S/L Cancl	N/A
35	5-9	AS-3077/SP	N/Stbd/Td	AN/SPS-49	N/A	SPS-49 CSLC	AN/SPS-49	850-942	N/A	S/L Cancl	N/A
36	5-10	AS-3078/SP	N/Mid/Level	AN/SPS-49	N/A	SPS-49 CSLC	AN/SPS-49	850-942	N/A	S/L Cancl	N/A
37	5-11	AS-3079/SP	N/Mid/P/Td	AN/SPS-49	N/A	SPS-49 CSLC	AN/SPS-49	850-942	N/A	S/L Cancl	N/A
ELECTRONIC WARFARE											
38	6-1	CV-1192/SLQ-32	B/Bk/Stbd	AN/SLQ-32	Clas'fd	AN/SLQ-32	AN/SLQ-32	Rec LHF-Ku	Clas'fd	Clas'fd	Clas'fd
39	6-2	CV-1192/SLQ-32	B/Bk/Port	AN/SLQ-32	Clas'fd	AN/SLQ-32	AN/SLQ-32	Xmit X-Ku	Clas'fd	Clas'fd	Clas'fd
WEAPONS CONTROL											
43	8-4	CIWS	B/Bk/Mid	MK 16 WEPS GRP	Clas'fd	CIWS	MK 16 WEPS	Ku-Band	Clas'fd	Pulse	Clas'fd
44	8-5	CIWS	B/Bk/Aft	MK 16 WEPS GRP	Clas'fd	CIWS	MK 16 WEPS	Ku-Band	Clas'fd	Pulse	Clas'fd
MISCELLANEOUS											
40	8-1A	T-436A/SAT-2	N/Stbd/Td	C-1356/SAT-2	N/A	AN/SAT-2A		TR	N/A	N/A	N/A
41	8-1B	T-436A/SAT-2	N/Port/Td	C-1356/SAT-2	N/A	AN/SAT-2A		TR	N/A	N/A	N/A
42	8-3	AR-106-36C	N/Port/Td	TV SYSTEM	N/A	ENTERTAIN	Rec only	TV	N/A	N/A	N/A
45	8-8	5 FT WHIP	B/Bk/Port	FURUNO FAX-208/A/N	N/A	WEATHER FAX	Rec only		N/A	N/A	N/A

While the emissions from the HF antennas are nondirectional and easily received at a single location, many of the emitters at or above the UHF band have directional antennas. This complicates estimating field strengths at various topside locations. A conservative approach has been taken for this work of using sidelobe field strength levels instead of mainlobe field levels for the highly directional emitters. With this field strength assignment, a conservative estimate of the average field strength at various topside locations can be made. The expected LSD-41 class topside EME will now be discussed.

4.2 SHIPBOARD EME DETERMINATION

When available, experimental weather deck EME data are used for estimating field strengths at different topside locations due to the various shipboard emitters. When experimental EME data are not available, a far-field approximation is used. In the far-field, the mainlobe weather deck EME due to a given emitter can be calcuated using

$$P_r = (P_t) \ (G) \ / \ 4\pi R^2 \tag{4.1}$$

where

P_r =   Received power density (W/m^2)

P_t =   Emitter level (W)

G =   Antenna gain (dBi)

R =   Radius (m), antenna to sensor

and the electric field stength (V/m) is then given by

$$E = (\eta \ P_r)^{1/2} \tag{4.2}$$

where $\eta = 377 \ \Omega$ is the free-space radiation resistance. When experimental data are not available, this expression is used (with gain correction for directional antennas) for estimating the field strength due to a shipboard emitter at various topside locations. For the higher frequency transmitters, this approximation should give fairly accurate results.

Experimental weather deck EM field level information is available for the HF antennas aboard the LSD-41 class naval vessel. Above the HF band, far-field EM field levels have been calculated using Eq. 4.1 and 4.2. This is an approximation to the exact near-field EM levels, which would require numerical calculation for each emitter. Measurements in the HF band (NRaD Contract N66001-90-D-0001) for the USS *Rushmore* have been made at 16 different sites about the ship and those measurements have been used for estimating purposes. From this experimental HF data and the calculated EM field levels above HF, it appears that as few as three topside sensor sites are required to determine the status of every shipboard emitter. The candidate topside sites for measurement are shown in figure 4-3. These sites have been chosen to be consistent with the sites where experimental HF measurements are available. Of these topside sites, shipboard measurements using the photonic EM field probe will be taken at sites 1, 16, 10, and 13. Site 1 is located on the 07 level, C/L, midway between the front of the CIWS housing and the railing. Site 16 is located on the port yardarm between antennas 5-5 and 3-6. Site 10 is located on the aft CIWS platform, C/L. Site 13 is located on the 01 level, C/L. With these proposed monitoring sites, an average field strength due to each emitter of at least 0.1 V/m

should be registered at one of the topside measurement locations. This field strength should be easily detectable with the photonic EM field probe. The actual shipboard measurement procedures will now be discussed.
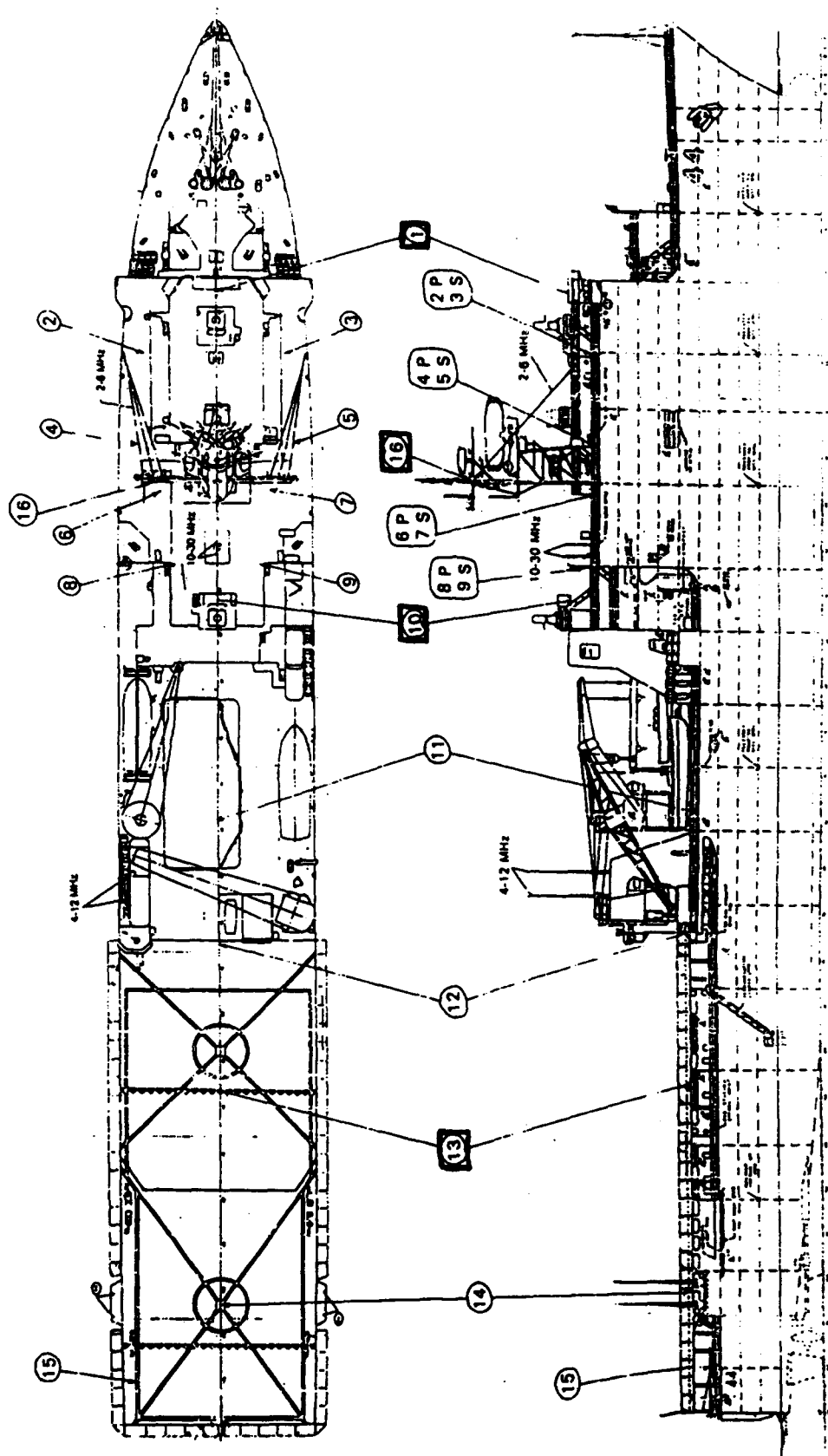
Figure 4-7. Candidate topside measurement sites aboard LSD-41 class ship.

54

4.3 SHIPBOARD TEST AND EVALUATION PROCEDURES

E-field intensity measurements at preselected topside sites due to as many emitters as can be accessed aboard an EMI-certified LSD-41 class ship will be performed. The testing will take place during the MAR 94 to SEP 94 timeframe and will probably include both in-port and at-sea testing in order to adequately assess the performance of the photonic EM field probe.

At the time an actual LSD-41 class ship has been scheduled for testing of the photonic EM field monitoring system, an initial inspection of the ship will be planned. Upon acceptance of the ship's condition, ship operators will be given both an in-port and an at-sea test plan which will be subject to their modification and approval. The two test plans will have some differences.

At-sea in a deployed environment, much more care and planning must be given to the required cabling and electronic equipment power requirements. Approved techniques for securing cables and a dedicated area for data acquisition and processing are required. Furthermore, at-sea testing is much less restrictive of emitter power levels and less prone to industrial EMI. Conversely, in-port testing is easier to schedule, is more flexible to spontaneous test modifications, is less affected by adverse weather conditions, and can use an onshore wall-powered vehicle as the remote site for data acquisition and processing. However, in-port transmitted power restrictions and industrial EMI can limit the scope of the testing. The ideal scenario is to perform preliminary in-port tests which culminate in an at-sea demonstration.

Once configured, the actual shipboard tests which are to be performed will be similar for both in-port and at-sea testing. The general test procedure will be to place the remote photonic probe at each of the selected topside positions and individually and simultaneously excite the probe with the shipboard transmitters. The shipboard emitter's frequency and transmitted power level information will be carefully measured. The E-field strengths, intermodulation product levels, and modulation characteristics will be recorded at the monitoring sites, with the transmitters operating in their normal operation mode (i.e., power levels and modulation format). Performance degradation due to industrial and military EMI caused by external offship emissions will be noted. Data acquisition and recording will occur in an approved topside site (or inside an onshore vehicle) through a length of 300 meters of single-mode optical fiber. Handheld two-way radios will be used to coordinate between the transmitter rooms and the processing site. Received power levels will be recorded from which electric field strengths will be deduced. The electrically powered laser and optical detector, as well as the required processing electronics, will be assembled at the remote processing site, where standard single-phase 115 V AC power which can supply a current of 20 A is required.

Upon completion of the shipboard testing, the data will be analyzed and an evaluation will be made of the photonic EM field probe for shipboard EME monitoring. A report will be submitted which will include the shipboard test results, the final photonic EM field probe configuration, recommendations for further development, and lessons learned for future Navy photonic R&D efforts.

5.0 CONCLUSIONS

The concept of using fiber optic and EO techniques for shipboard remote broadband EM field monitoring has been demonstrated. The performance of the externally modulated fiber optic link has been improved by refining the components in the current 2- to 18-GHz system and by implementing system configuration and measurement improvements. An integrated RF probe design for continuous 2-MHz to 18-GHz frequency coverage has been developed. Expected electric field strengths at selected points about an LSD-41 class ship have been determined, and three topside measurement sites appear adequate to obtain the entire ship EM signature.

Laboratory and anechoic chamber measurements have been performed in the 2-MHz to 18-GHz frequency range on a second-generation externally modulated EO EME monitoring system. The system consists of two compact antennas (spiral antenna and short dipole antenna) which cover the entire frequency range, an optically powered and controlled analog fiber optic link, and a wideband spectrum analyzer. Electric field sensitivities of < 1 V/m in a 30-kHz bandwidth with a spurious free dynamic range > 75 dB have been demonstrated with this system. This system is currently being packaged and readied for a shipboard demonstration.

The performance of this system is limited at the high-frequency end by the optical modulator. R&D efforts supporting this task are under way to produce optical modulators with bandwidths exceeding 40 GHz, and prototypes should be available in FY 94. The use of III-V semiconductor optical waveguide modulators as well as lithium niobate MZ modulators are being considered for this application. Both FKE and QCSE semiconductor modulators have been investigated and compared to state-of-the-art lithium niobate MZ modulators for this analog fiber optic application. System comparisons using experimental results of the semiconductor EA and MZ modulators indicate that for moderate system bandwidths (< 20 GHz), not much difference in performance between the two types of modulators is expected. If, however, the optical insertion loss of the EA modulators can be improved to that attained by MZ modulators, superior performance will result. For ultrawideband (> 30 GHz) analog systems, the EA modulators, even with the presently existing large optical insertion losses, will outperform the MZ modulators. This is due to the more severe decrease in RF efficiency of the MZ modulators with increasing bandwidth.

The performance of the photonic EM field sensor is limited at the low-frequency end by the gain of the compact antenna. A number of antenna structures have been and are continuing to be investigated for use in the wideband EM field sensor. At present, an electrically short dipole antenna with limited gain appears to be the most practical choice for 2 MHz to 500 MHz. With this 15-cm-long antenna, broad beamwidth response is obtained, which results in a calculated electric field sensitivity of < 1 V/m at 2 MHz. Better sensitivity is achieved with this dipole antenna at frequencies approaching 500 MHz. Above 500 MHz, a broad beamwidth, cavity-backed two-arm spiral antenna is used. This antenna has > 0 dBi gain from 500 MHz to 18 GHz.

The 2-MHz to 18-GHz prototype photonic EM field sensor will be tested in FY 94 aboard an LSD-41 class naval surface ship. Communication, surveillance, and electronic warfare transmissions will be monitored using the photonic EM field probe at selected topside locations. Transmission frequencies, power levels, dynamic range, and intermodulation products will be remotely recorded. The results will be published in a technical report which will include recommendations as to further development.

In summary, it has been found that shipboard EO EME monitoring is currently feasible for frequencies up to 20 GHz using an externally modulated fiber optic system. Systems with frequency coverage to 40 GHz should be possible in the near future as optical modulator performance is improved. A shipboard demonstration to validate these findings is scheduled for FY 94.

6.0 RECOMMENDATIONS

The following recommendations are made concerning the development of a shipboard EO EME monitoring system:

1. Continue preparing 2-MHz to 18-GHz EME monitoring system for actual shipboard tests which will be conducted in FY 94.

2. Continue developing optical modulation techniques which will extend out to 50 GHz.

3. Continue developing compact HF/VHF antenna probe structures which optimize the size/bandwidth/gain tradeoffs.

4. Identify follow-on Navy sponsorship for specific applications and subsequently develop a frequency agile receiver with a user-friendly PC-based interface.

6. RECOMMENDATIONS

The following recommendations are made concerning the development of a shipboard EO EME monitoring system:

1. Continue preparing 2-MHz to 18-GHz EME monitoring system for actual shipboard tests which will be conducted in FY 94.

2. Continue developing optical modulation techniques which will extend out to 50 GHz.

3. Continue developing compact HF/VHF antenna probe structures which optimize the size/bandwidth/gain tradeoffs.

4. Identify follow-on Navy sponsorship for specific applications and subsequently develop a frequency agile receiver with a user-friendly PC-based interface.

14. S. A. Pappert, R. J. Orazi, T. T. Vu, S. C. Lin, A. R. Clawson, and P. K. L. Yu, "Polarization dependence of a 1.52 μm InGaAs/InP multiple quantum well waveguide electroabsorption modulator," *IEEE Photon. Technol. Lett.*, vol. 2, 257 (1990).

15. G. Betts, L. M. Walpita, W. S. C. Chang, and R. F. Mathis, "On the linear dynamic range of integrated electrooptical modulators," *IEEE J. Quantum Electron.*, vol. QE-22, 1009 (1986).

16. K. Wakita, I. Kotaka, O. Mitomi, H. Asai, Y. Kawamura, and M. Naganuma, "High speed InGaAs/InAlAs multiple quantum well optical modulators with bandwidths in excess of 40 GHz at 1.55 μm," *Technical Digest CLEO '90*, 70 (1990).

17. P. K. L. Yu, Y. Z. Liu, A. L. Kellner, A. R. Williams, B. C. Lam, and X. S. Jiang, "Design and fabrication of InGaAsP/InP waveguide modulators for microwave applications," *SPIE Proc.* 1703, 100 (1992).

18. Y. Z. Liu, J. M. Chen, S. A. Pappert, R. J. Orazi, A. R. Williams, A. L. Kellner, X. S. Jiang, and P. K. L. Yu, "Semiconductor electroabsorption waveguide modulator for shipboard analog link applications," *SPIE Proc.* 2155, Paper #11 (1994).

19. C. H. Bulmer, W. K. Burns, and A. S. Greenblatt, "Phase tuning of LiNbO$_3$ modulators by excimer laser ablation," PSAA-91 *Tech. Dig.*, 64 (1992).

20. C. H. Cox, L. A. Bernotas, G. E.Betts, A. I. Grayzel, D. R. O'Brien, J. J. Scozzafava, and A. C. Yee, "An externally-modulated fiber-optic link test bed for addressing application issues and options," PSAA-91 *Tech. Dig.*, 1 (1992).

21. M. H. Berry, R. J. Orazi, S. A. Pappert, and S. T. Li, "Stability of remote, optically powered and controlled externally modulated fiber optic links," PSAA-92 *Tech. Dig.*, 75 (1993).

22. W. K. Burns, R. P. Moeller, C. H. Bulmer, and A. S. Greenblatt, "Depolarized source for fiber-optic applications," *Opt. Lett.* 16, 381 (1991).

23. T. Okoshi, "Polarization-state control schemes for heterodyne or homodyne optical fiber communications," *J. Lightwave Technol.* LT-3, 1232 (1985).

24. S. Rumbaugh, M. D. Jones, and L. W. Casperson, "Polarization control for coherent fiber-optic systems using nematic liquid crystals," *J. Lightwave Technol.* LT-8, 459 (1990).

25. S. R. Ascham, M. C. K. Wiltshire, S. J. Marsh, and A. J. Gibbons, "A practical liquid crystal polarisation controller," *Proc. ECOC '90*, 393 (1990).

26. R. Noe, H. J. Rodler, A. E. Ebberg, G. Gaukel, B. Noll, J. Wittmann, and F. Auracher, "Comparison of Polarization handling methods in coherent optical systems," *J. Lightwave Technol.* LT-9, 1353 (1991).

REPORT DOCUMENTATION PAGE

Public reporting burden for this collection of information is estimated to average 1 hour per response, including the time for reviewing instructions, searching existing data sources, gathering and maintaining the data needed, and completing and reviewing the collection of information. Send comments regarding this burden estimate or any other aspect of this collection of information, including suggestions for reducing this burden, to Washington Headquarters Services, Directorate for Information Operations and Reports, 1215 Jefferson Davis Highway, Suite 1204, Arlington, VA 22202-4302, and to the Office of Management and Budget, Paperwork Reduction Project (0704-0188), Washington, DC 20503.

1. AGENCY USE ONLY *(Leave blank)*	2. REPORT DATE May 1994	3. REPORT TYPE AND DATES COVERED Interim: October 1992 – 1993

4. TITLE AND SUBTITLE

ULTRAWIDEBAND SHIPBOARD ELECTROOPTIC ELECTROMAGNETIC ENVIRONMENT MONITORING

5. FUNDING NUMBERS

SC1A/PE0602121N

6. AUTHOR(S)

S. Pappert, M. Berry, S. Hart, R. Orazi, L. Koyama, and S. T. Li

7. PERFORMING ORGANIZATION NAME(S) AND ADDRESS(ES)

Naval Command, Control and Ocean Surveillance Center (NCCOSC),
RDT&E Division
San Diego, CA 92152–5001

8. PERFORMING ORGANIZATION REPORT NUMBER

TR 1646

9. SPONSORING/MONITORING AGENCY NAME(S) AND ADDRESS(ES)

Office of the Chief of Naval Research
Code 334
Arlington, VA 22217–5000

10. SPONSORING/MONITORING AGENCY REPORT NUMBER

11. SUPPLEMENTARY NOTES

12a. DISTRIBUTION/AVAILABILITY STATEMENT

Approved for public release; distribution is unlimited.

12b. DISTRIBUTION CODE

13. ABSTRACT *(Maximum 200 words)*

This report summarizes the current R&D status of an electrooptic electromagnetic environment monitoring system for shipboard use. Ultrawideband analog photonic link development and wideband electromagnetic sensing elements are described. System performance results from 2 MHz to >20 GHz are reported and future shipboard demonstration plans are described.

14. SUBJECT TERMS

electrooptics
antenna remoting
fiber optics
electromagnetic field sensor
analog photonic links
ultrawideband antennas

15. NUMBER OF PAGES

74

16. PRICE CODE

17. SECURITY CLASSIFICATION OF REPORT	18. SECURITY CLASSIFICATION OF THIS PAGE	19. SECURITY CLASSIFICATION OF ABSTRACT	20. LIMITATION OF ABSTRACT
UNCLASSIFIED	UNCLASSIFIED	UNCLASSIFIED	SAME AS REPORT

21a. NAME OF RESPONSIBLE INDIVIDUAL	21b. TELEPHONE (Include Area Code)	21c. OFFICE SYMBOL
S. A. Pappert	(619) 553–5704	Code 555

INITIAL DISTRIBUTION

Code 0012	Patent Counsel	(1)
Code 014	K. J. Campbell	(1)
Code 01414	A. Gordon	(1)
Code 0274	Library	(2)
Code 0275	Archive/Stock	(6)
Code 50	H. O. Porter	(1)
Code 55	H. E. Rast	(1)
Code 555	M. N. McLandrich	(1)
Code 555	S. A. Pappert	(25)
Code 555	R. J. Orazi	(1)
Code 80	K. D. Regan	(1)
Code 82	R. J. Kochanski	(1)
Code 822	S. T. Li	(10)
Code 822	S. Hart	(1)
Code 822	L. B. Koyama	(1)
Code 843	M. H. Berry	(1)

Defense Technical Information Center
Alexandria, VA 22304–6145 (4)

NCCOSC Washington Liaison Office
Washington, DC 20363–5100

Center for Naval Analyses
Alexandria, VA 22302–0268

Navy Acquisition, Research and Development
    Information Center (NARDIC)
Arlington, VA 22244–5114

GIDEP Operations Center
Corona, CA 91718–8000

Naval Surface Warfare Center
Carderock Detachment
Annapolis, MD 21402–1198

Naval Sea Systems Command
Arlington, VA 22245–5200

Naval Research Laboratory
Washington, DC 20375–5320

Space and Naval Warfare Systems Command
2451 Crystal Drive
Arlington, VA 22245–5200

Office of Naval Research
Arlington, VA 22217–5000

Naval Undersea Warfare Center
Washington, DC 20362–5101

Naval Air Warfare Center
Washington, DC 20361–6000